

Mixed-phase and ice cloud observations with NIXE-CAPS

Anja Costa



Member of the Helmholtz Association

**Energie & Umwelt /
Energy & Environment
Band / Volume 397
ISBN 978-3-95806-273-3**

 **JÜLICH**
FORSCHUNGSZENTRUM

Forschungszentrum Jülich GmbH
Institute of Energy and Climate Research
Stratosphere (IEK-7)

Mixed-phase and ice cloud observations with NIXE-CAPS

Anja Costa

Schriften des Forschungszentrums Jülich
Reihe Energie & Umwelt / Energy & Environment

Band / Volume 397

ISSN 1866-1793

ISBN 978-3-95806-273-3

Bibliographic information published by the Deutsche Nationalbibliothek.
The Deutsche Nationalbibliothek lists this publication in the Deutsche
Nationalbibliografie; detailed bibliographic data are available in the
Internet at <http://dnb.d-nb.de>.

Publisher and
Distributor: Forschungszentrum Jülich GmbH
Zentralbibliothek
52425 Jülich
Tel: +49 2461 61-5368
Fax: +49 2461 61-6103
Email: zb-publication@fz-juelich.de
www.fz-juelich.de/zb

Cover Design: Grafische Medien, Forschungszentrum Jülich GmbH

Source Cover Image: Anja Costa

Printer: Grafische Medien, Forschungszentrum Jülich GmbH

Copyright: Forschungszentrum Jülich 2017

Schriften des Forschungszentrums Jülich
Reihe Energie & Umwelt / Energy & Environment, Band / Volume 397

D 468 (Diss., Wuppertal, Univ., 2017)

ISSN 1866-1793
ISBN 978-3-95806-273-3

The complete volume is freely available on the Internet on the Jülicher Open Access Server (JuSER)
at www.fz-juelich.de/zb/openaccess.



This is an Open Access publication distributed under the terms of the [Creative Commons Attribution License 4.0](https://creativecommons.org/licenses/by/4.0/),
which permits unrestricted use, distribution, and reproduction in any medium, provided the original work is properly cited.

Abstract

Clouds are a main component in the climate system. They influence the energy balance of the atmosphere by changing the earth's albedo and greenhouse effect, and redistribute energy by releasing and consuming latent heat in cloud particle nucleation and dissolution processes. Climate models therefore react sensitively on the implemented cloud parametrizations, which have to be under constant review to implement new insights into cloud formation and evolution processes. Ice clouds pose a particular challenge for simulations: In mid-level and high clouds, several possible ways for cloud glaciation and ice particle formation compete. These processes produce particles that vary strongly in habits, concentrations and radiative properties. As long as it remains unclear which processes are active, how their influence is distributed globally, how these processes might change due to global warming, and what the properties of the produced ice particles are, ice clouds will remain a significant factor of uncertainty in climate predictions. Over the last years, a number of studies has been performed to examine these questions. The Jülich instrument NIXE-CAPS has contributed a unique ice particle concentration dataset that was used to evaluate global cloud simulations. This thesis presents the extension of the aforesaid dataset into mid-level clouds, where the partitioning of ice and supercooled liquid water becomes increasingly relevant. NIXE-CAPS provides three relevant characteristics of the observed clouds: particle number concentrations, particle size distributions and particle asphericity - especially of small particles with diameters below $50 \mu\text{m}$, which have been rarely analysed so far.

The analysis of this data set was extended, evaluated and accelerated in the course of this work: instrument comparisons, error estimations and new corrections complement earlier works with NIXE-CAPS. The improved algorithms allowed a reanalysis of previous measurements and resulted in a consistent data set covering 39 hours of measurements within high clouds (cirrus) and over 38 hours within mid-level clouds.

With the NIXE-CAPS measurements, the following tasks were performed: The proportions of liquid, mixed-phase, 'small ice', and 'large ice' clouds were resolved for Arctic, mid-latitude and tropical observations. Also, the new model CLaMS-Ice was evaluated and improved with respect to its microphysical accuracy: It provides detailed cirrus cloud simulations over a wide range of meteorological conditions. It can thus be used for large-scale cirrus cloud simulations which is expected to lead to new insights regarding the global cirrus cloud cover's climatological characteristics.

Zusammenfassung

Wolken sind ein wichtiger Bestandteil des Klimasystems. Durch ihren Albedoeffekt und ihren Einfluss auf den Treibhauseffekt modifizieren sie die Strahlungsbilanz. Darüber hinaus beeinflussen sie die Energieverteilung in der Atmosphäre durch die Freisetzung und den Verbrauch latenter Wärme bei Wolkenpartikelbildungs- und -auflösungsprozessen. Klimamodelle sind daher sensitiv auf Änderungen in der Wolkenparametrisierung. Diese Parametrisierungen müssen ständig angepasst werden, um die wachsenden Erkenntnisse zu Wolkenprozessen angemessen zu repräsentieren. Eine besondere Herausforderung stellen Eiswolken (Cirren) dar: In mittleren und hohen Wolken kann das Gefrieren oder die Neubildung einer Wolke auf unterschiedlichen Wegen erfolgen, die jeweils sehr unterschiedliche Wolkencharakteristika im Hinblick auf Eiskristallformen, Konzentrationen und damit auch den Strahlungseffekt hervorbringen. Solange nicht klar ist, in welchem Umfang welche Prozesse aktiv sind und welche Partikelpopulationen durch sie erzeugt werden, bleiben Wolken ein wesentlicher Unsicherheitsfaktor in der Klimavorhersage. In den letzten Jahren wurde eine Vielzahl von Studien durchgeführt, um diese Prozesse zu erforschen. Das Jülicher Instrument NIXE-CAPS hat dabei einen einzigartigen Datensatz zu Eispartikelkonzentrationen beigetragen, mit dem globale Wolkensimulationen evaluiert werden. In der vorliegenden Doktorarbeit wird dieser Datensatz um wärmere Wolken erweitert, in denen die Aufteilung der Wolkenpartikel in Eis und unterkühltes Wasser eine zunehmende Rolle spielt. NIXE-CAPS liefert drei relevante Parameter: Anzahlkonzentrationen, Größenverteilungen und Asphärität von Wolkenpartikeln, insbesondere von kleinen Partikeln mit Durchmessern unter $50\ \mu\text{m}$, die bisher kaum analysiert wurden.

Im Lauf dieser Arbeit wurde die NIXE-CAPS-Datenanalyse erweitert, überprüft und beschleunigt: Durch Instrumentenvergleiche, Fehlerabschätzungen und neue Datenkorrekturen konnte die bisherige Auswertung verbessert werden. Dadurch war eine Reanalyse der vorherigen Messungen möglich. Insgesamt beläuft sich der NIXE-CAPS-Datensatz nun auf 39 Stunden Messung in Cirren und über 38 Stunden in mittelhohen Wolken.

Mithilfe dieser Daten konnten die folgenden Fragen bearbeitet werden: Die Anteile flüssiger und gemischtphasiger sowie die von kleinen bzw. großen Kristallen dominierter Eiswolken konnten getrennt für die Arktis, die Mittelbreiten und die Tropen bestimmt werden. Außerdem konnte das neue Modell CLaMS-Ice hinsichtlich seiner mikrophysikalischen Genauigkeit überprüft und verbessert werden: Es ermöglicht detaillierte Simulationen von hohen Wolken, und zwar über eine große Breite an meteorologischen Bedingungen. Cirren können damit großflächig charakterisiert werden, was neue Erkenntnisse zu deren klimatologischen Charakteristika verspricht.

Contents

1	Introduction: Mixed-phase and ice clouds	1
2	The NIXE-CAPS instrument: Description and data analysis	5
2.1	NIXE-CAPS: Instrument description	7
2.1.1	NIXE-CAS-DPOL	7
2.1.2	NIXE-CIP-G	9
2.2	Particle asphericity	11
2.2.1	NIXE-CAS: Description and verification in AIDA cloud chamber experiments	11
2.2.2	NIXE-CIP: Description of the asphericity analysis	15
2.3	NIXE-CAPS data evaluation	16
2.4	Sampling volume effects: 'Single particle events'	18
2.5	Sources of measurement uncertainties	21
2.5.1	Particle sizing	21
2.5.2	Particle shattering (CAS, CIP)	21
2.5.3	Poisson spots (CIP)	22
2.5.4	Artificial particles (CIP)	22
2.5.5	Particle coincidence (CAS)	23
2.5.6	Total concentrations, total masses (CAS and CIP combined)	24
3	Classification of mid-level clouds derived from NIXE-CAPS observations	29
3.1	Clouds in the mixed-phase temperature regime	29
3.2	Field campaigns	33
3.3	Results and Discussion	39
3.3.1	Mpt cloud classification based on particle number size distributions	39
3.3.2	Comparison of cloud particle with with ice nuclei numbers	43
3.3.3	Mpt cloud classification based on sphericity	44
3.3.4	Cloud type detection in the mpt regime	46
3.3.5	Mpt cloud classification: Results	47
3.4	Summary and conclusions	52
4	Simulation of NIXE-CAPS observations during ML-Cirrus using CLaMS-Ice	55
4.1	Motivation	55

4.2	Brief description of the ML-Cirrus campaign	56
4.3	Coupling 3D trajectories with ice microphysics	58
4.3.1	CLaMS trajectories	58
4.3.2	Microphysical ice cloud simulation in CLaMS-Ice	60
4.3.3	Model acceleration by variable time steps	63
4.3.4	CLaMS-Ice initialization	63
4.3.5	Identification of in-situ and liquid origin cirrus clouds	64
4.4	Simulations of ML-Cirrus clouds and CLaMS-Ice performance	64
4.4.1	Comparing simulations and observations	64
4.4.2	Overall model performance	65
4.4.3	Model performance, insitu cirrus	70
4.4.4	Model performance, liquid origin cirrus	72
4.5	Case Studies	74
4.5.1	Case I: Cold cirrus	74
4.5.2	Case II: Sedimentation and high-pressure cirrus	79
4.5.3	Case III: Warm conveyor belt: microphysical separation and outflow characteristics	81
4.6	CLaMS-Ice simulations - Summary	85
4.7	Outlook - future work on CLaMS-Ice	86
5	Thesis summary and outlook	89
	Bibliography	91
	Appendix	100
A	Single particle events in the NIXE-CAPS data	101
B	Data evaluation with the NIXElib	111
B.1	NIXElib description and new features	111
B.2	User options and standard settings	114
C	Acknowledgments	117

List of Figures

1.1	Ice clouds in the mid-level and high atmosphere can form under various circumstances.	2
1.2	Highly variable cloud particle concentrations during ML-Cirrus flight 12.	3
2.1	NIXE-CAPS dismantled. The upper flat box contains the CAS instrument; its laser beam is hidden in the housing. The CIP laser beam is located between the two arms capped with oranges spikes, which lead shattered particle fragments away from the measurement area. The blue arrows indicate the air flow direction in flight.	6
2.2	NIXE-CAPS mounted on HALO.	6
2.3	Schematic setup of the CAS instrument. Monochromatic polarized laser light is scattered by particles entering the beam. The scattered light is measured a) in the forward direction by two sensors, the sizing detector and the qualifying detector, and b) in the backward direction by two sensors, one who measures the backwards scattered p-polarized light and a second one measuring the s-polarized component. Image taken from Baumgardner et al. (2014).	7
2.4	Scattering cross sections (SCS) of spherical water and glass particles. For water particles, the SCS for varying particle sizes are not unique. To perform particle sizing with the obtained SCS, size bins have to be applied that are constrained at unique values. D_p : Particle diameter. Image taken from DMT (2009).	8
2.5	CIP image data were evaluated with different settings for two cloud situations. 'Allin' means that only particles that do not touch the borders of the array were accepted. In the 'Reconstructed' mode, an estimated diameter is calculated for particles which extend over the array borders. 'GT 0' means 'grey threshold 0': here, all shaded areas are counted as particle pixels. 'GT 2' restricts the image area to core shadow pixels (grey threshold 2: at least 65% shading). Image: courtesy of Anna Luebke.	11

2.6	In this AIDA experiment (RICE03, Exp. 20) a water cloud was generated which froze as the chamber was cooled down. Panel 1 shows the development of temperature, pressure and relative humidities wrt water/ice with time. Panel 2 shows the NIXE-CAPS particle size distributions with time. As the cloud is initiated, a large number of small droplets forms, along with few large ice crystals that froze heterogeneously. When the relative humidity with respect to water sinks below 100%, the droplets evaporate and the ice particles grow.	13
2.7	Measurements of cross-polarized light in the backscatter direction as an indicator for particle sphericity during experiment 20, RICE03. Each particle is characterized by a size value, obtained via the forward scattering measurement, and a backward cross polarized intensity (see subsection 2.1.1). The color depicts the frequency of occurrence; the darker the color, the more particles with the respective characteristics were found. a) liquid droplet phase, b) at the initial freezing, few larger particles appear; their backscatter intensities are well above the threshold for spherical particles. c) Seconds later, the small round particles start to disappear, with the large, aspherical fraction growing. d) The remaining ice particles show a strong backscatter intensities.	14
2.8	Comparison of the aspherical fractions obtained by NIXE-CAPS and PPD-2K (Järvinen et al., 2016). D_p stands for particle diameter. The NIXE-measurements become insensitive to aspherical particles for particle sizes smaller than $20 \mu\text{m}$. For this reason, the NIXE total aspherical fractions only cover particles larger than $20 \mu\text{m}$	15
2.9	CIP images of ice plates during ML-Cirrus Flight 02, 21.03.2014.	16
2.10	Same as Figure B.1, but with 'single particle event' correction in the CAS data.	17
2.11	Top: Frequency of occurrence of particle concentrations measured with an FSSP instrument, which has a sampling volume comparable to the NIXE-CAS. Image taken from Krämer et al. (2009). Bottom: Frequency of occurrence of particle concentrations measured with the NIXE-CAPS in cirrus clouds (bottom left panel), in combination with a fast CDP in tropical cirrus (bottom right panel). Images taken from Krämer et al. (2016a).	19
2.12	Frequency of occurrence of cloud particle concentrations in the ML-Cirrus measurements.	19
2.13	Frequency of occurrence of cloud particle concentrations measured with NIXE-CAPS during ML-Cirrus 2014. Top panel: Original dataset, bottom: dataset after 'single particle event' correction. Plot: Courtesy of Nicole Spelten.	20

2.14	Shattering analysis for several cloud sections of flight 18 of the ACRIDICON-CHUVA campaign. Section description: A - warm cloud, B - mixed-phase cloud, C - cumulonimbus anvil, D - cirrus, E - secondary ice cloud (see chapter 3). Left column: Particle interarrival time histograms for CAS (black line) and CIP (blue line); the plot also shows the total number of particles whose IAT was analyzed here. Right column: Average particle size distribution for the chosen section.	25
2.15	Influence of the Poisson spot correction on a cloud measurement with out-of-focus particles (detected manually in the image preview).	26
2.16	At cold temperatures, some diodes of the CIP instruments are sensitive to aircraft vibrations or electric charges (personal communication, A. Afchine). These vibrations cause the instrument to record 'noise' particles. It's always the same set of diodes that are affected. The noise can therefore be filtered out using its regularity. The blue curve shows shadow counts for all diodes (diode numbers: 1 to 64) in a noise-dominated time buffer. In contrast, the red curve shows the average shadow counts per buffer for all diodes for the entire flight - here, the noisy diodes no longer show an enhanced signal.	26
2.17	Measurement uncertainties can influence two parameters: the obtained particle sizes and particle concentrations. This plot shows the accumulated influence of the NIXE-CAPS measurement uncertainties described by Meyer (2012). Black lines: calculations with standard settings. The pink lines (minimum estimations) and purple lines (maximum estimations) enclose the range of the measurement uncertainty.	27
3.1	Possible paths to glaciation in the mixed-phase temperature regime	29
3.2	Liquid water content (dashed lines) and ice water content (solid lines) development with altitude ($\sim 1/\text{temperature}$) in mixed-phase clouds for different vertical velocities (adapted from Korolev, 2007a, with modification). Blue lines (updraft 1 m s^{-1}): the cloud glaciates when RHw falls below 100% (WBF = Wegener-Bergeron-Findeisen regime); red lines (updraft 2 m s^{-1}): RHw stays above 100%, liquid droplets and ice crystals coexist (Coexistence regime).	31
3.3	Locations of the campaigns comprised in this study.	34
3.4	Size distributions along time during flight 08 of the VERDI campaign. Two types of clouds can be distinguished; one is dominated by the large particle mode (Type 2, example in lower left panel), the second by small particles (Type 1, example in lower right panel). The two cloud types are also associated with strongly differing particle number concentration ranges, cf. Figure 3.5.	39

3.5	Histogram of cloud particle concentrations (D_p $3 \mu\text{m}$ to $937 \mu\text{m}$) of Type 1 and Type 2 clouds in the mixed-phase temperature regime between 0°C and -38°C . For cloud type definitions see subsection 3.3.1. The 6% between the two clear modes were classified as 'Type 1' in this study. N_{small} : Particles with diameters between $3 \mu\text{m}$ and $50 \mu\text{m}$. N_{large} : Particles with diameters $> 50 \mu\text{m}$. N_{cloud} : All particles with diameters of $3 \mu\text{m}$ and larger.	40
3.6	Type 1 clouds: Example of CIP images and average particle size distributions (PSDs) in 5 K intervals, all campaigns. The thin vertical line at $3 \mu\text{m}$ marks the boundary between aerosol and cloud particles. The line at $20 \mu\text{m}$ marks the transition from the NIXE-CAS-DPOL to the NIXE-CIPg instrument. The thick blue line divides the cloud particle population in particles smaller and larger than $50 \mu\text{m}$	42
3.7	Same as in Figure 3.6, but for Type 2 clouds.	43
3.8	Frequencies of ice nucleating particle number concentrations (N_{INP}) vs. temperature for all measurement campaigns, estimated from NIXE-CAPS measurements of aerosol concentrations (D_p $0.6 - 3 \mu\text{m}$) following DeMott et al. (2010). The black lines indicate INP concentrations for constant aerosol concentrations of 0.01 cm^{-3} (leftmost line), 0.1 cm^{-3} , 1 cm^{-3} (thick line), 10 cm^{-3} and 100 cm^{-3} (rightmost line).	44
3.9	Same as Figure 3.8, but frequencies of cloud particle number concentrations for N_{small} (left panel) and N_{large} (right panel). Top row: Type 1 clouds, bottom row: Type 2 clouds.	45
3.10	Aspherical fractions (AF) for $D_p = 20$ to $50 \mu\text{m}$. Type 1 clouds show a variety of AF. Type 2 shows AFs comparable to cirrus clouds - which is illustrated by observations from the ML-Cirrus campaign (see chapter 4) - throughout the temperature range.	46
3.11	Frequency of occurrence for vertical velocities (w) within mpt clouds during the campaigns VERDI (Arctic), COALESC (mid-latitudes) and ACRIDICON-CHUVA (tropics).	47
3.12	Frequencies of occurrence of INP concentrations (N_{INP}) vs. temperature during VERDI and RACEPAC (Arctic), COALESC (mid-latitudes) and ACRIDICON-CHUVA (tropics). INP number concentrations are estimated via aerosol concentrations for particles $> 0.6 \mu\text{m}$ following DeMott et al. (2010). The black lines indicate INP concentrations for constant aerosol concentrations of 0.01 cm^{-3} (leftmost line), 0.1 cm^{-3} , 1 cm^{-3} , 10 cm^{-3} and 100 cm^{-3} (rightmost line). . . .	48

3.13	Occurrence of the cloud types defined in subsection 3.3.3: "Mostly liquid" clouds are dominated by small, exclusively spherical particles. They have high overall number concentrations. "Coexistence" clouds are dense, too, but do contain some small aspherical particles, indicating that a glaciation process has begun. The "secondary ice" cloud type is again very dense - the particle numbers exceed the INP concentration estimations by far (see subsection 3.3.2). Here, most of the small particles in the size range between 20 μm and 50 μm are aspherical; the cloud must therefore consist of ice. In contrast, clouds in the category "WBF/large ice" show low overall number concentrations. These clouds are dominated by large ice particles which may resume from the Wegener-Bergeron-Findeisen process or, especially in the tropics, be large, sedimenting ice aggregates from cumulonimbus anvils.	49
3.14	Temperature vs. altitude for the four field campaigns VERDI, RACEPAC, COALESC and ACRIDICON-CHUVA. Due to the varying latitudes, the profile differs for the four measurement campaigns.	50
4.1	Probability of occurrence of RH _i measurements within clouds as a function of temperature. The expected distribution would have a peak at RH _i = 100%. Graphic: courtesy of Christian Rolf.	57
4.2	24 backward trajectories are calculated by CLaMS that show the air parcel origin and the temperature/pressure history before the air reached the flightpath. Temperature, pressure, relative humidity and ice water content based on the ECMWF data fields are assigned to the trajectory.	59
4.3	Backward trajectories on different pressure altitudes starting at the flightpath (dark blue line) of HALO flight 06 of ML-Cirrus, 27.03.2014.	60
4.4	CLaMS-Ice simulates cirrus clouds in forward direction along the trajectories (red line, see Figure 4.2). As an air parcel cools along its trajectory, a cloud can form and the ice particle concentration (N _{ice}) is rising (blue line).	61
4.5	Agreement between CLaMS-Ice and ECMWF and observations during ML-Cirrus: The values show for how many data points the agreement criterion was fulfilled. This criterion (tolerated deviation) is given below the bars. Top: Temperature comparison based on BAHAMAS data, bottom: RH _i comparison based on SHARC data.	66
4.6	Random temperature fluctuations after Gary (2006) trigger cloud nucleation events at different points along the trajectory. This has a strong influence on the comparison between simulation and observation at the end point of the trajectory. Purple: Simulated trajectories, black square: NIXE-CAPS observation at flightpath.	70

4.7	Agreement between CLaMS-Ice/ECMWF and observations as in Figure 4.5, but restricted to insitu cirrus clouds during ML-Cirrus. Top: Temperature comparison, bottom: RH _i comparison.	71
4.8	Agreement between CLaMS-Ice/ECMWF and observations as in Figure 4.5, but restricted to liquid origin clouds during ML-Cirrus. Top: Temperature comparison, bottom: RH _i comparison.	72
4.9	20 Minutes of measurements by the HALO instrumentation during the entry of a cold cirrus field west of Portugal. From top to bottom: a) temperature, b) relative humidity, c) ice water content and d) ice particle number concentrations.	75
4.10	'Cold cirrus' case study: The trajectories leading to the flightpath reveal that a bifurcation point was passed. Maritime trajectories from southwest meet continental trajectories from northeast. The color code denotes the pressure along the trajectory.	76
4.11	'Continental air' trajectories. Top left: This graph shows the model's deviation from the observed values for 352 model runs with regard to the parameter RH _i . Each colored square depicts a model/observation comparison of 1100 data points (1 Hz observational data, 1 simulation result per minute interpolated to 1 Hz values). The deviation is given as absolute difference in the simulated and measured RH _i . The model runs below the horizontal line show the results for a purely homogeneous nucleation; in this case, the initial model concentration for IN is 0 cm ⁻³ . Top right: Model deviation from the observed values for 352 model runs with regard to the parameter IWC. The deviation is given as relative error between the simulated and measured IWC. Bottom left: As top right, but for N _{ice}	77
4.12	Model deviations from observed values. Like Figure 4.11, but for the maritime trajectories.	78
4.13	Case study II: The model input parameters that led to the best results are quite different for each respective cloud segment. The plot shows the cloud edge (left panels), top (middle panels) and cloud middle (right panels). The top row shows the results from the RH _i comparison, middle row: ice water content, bottom row: cloud particle concentrations.	80

4.14	Two segments of flight 06 of ML-Cirrus, on the 27th of March 2014. The left panels show CLaMS trajectories leading to two chosen flightpath segments: One close to the ascent region of the warm conveyor belt (top), the other in the warm conveyor belt's outflow regions over the Alps (bottom). (Color code: pressure along trajectory as in Figure 4.10. Grey line: flightpath.) The solid blue diamonds in the panels on the right show cloud particle number concentrations (N_{ice}) and ice water contents (IWC) measured by NIXE-CAPS in these segments. Blue lines show the location of these values to indicate the range of the observations on the axes. The empty diamonds show the CLaMS-Ice simulation results. The red stars show the IWC that ECMWF predicts. The respective N_{ice} are calculated using the Boudala et al. (2002) parametrization.	82
4.15	Top: CIP images recorded within the cirrus cloud layer at the higher altitude above the liquid origin clouds (compare Figure 4.17). Middle panels: As the aircraft descends into the liquid origin cloud region, a shift in the particle habits towards larger diameters and more complex shapes can be observed. Bottom: Within the liquid origin clouds, large rosettas and aggregates are recorded by the CIP.	83
4.16	The region near Corsica was probed for about 40 minutes during flight 06 of ML-Cirrus. The measurements are divided into two parts that are different with regard to the cloud particle number concentration's variability (lowest panel) and the cloud particle size range (middle panel).	84
4.17	CLaMS-Ice simulation results for a curtain from 400 to 200 hPa along the flightpath. The x-axis shows kilometers of flight. The section between kilometers 1000 and 1500 clearly shows the increased variability of cirrus cloud ice particle concentrations compared to the WCB below. For N_{ice} observations along the flightpath see Figure 4.16.	85
A.1	Frequency of occurrence of cloud particle concentrations in the ML-Cirrus measurements.	101
A.2	The CAS sampling volume (SV) only depends on the speed of the aircraft. . .	102
A.3	The CIP sampling volume (SV) in dependence on the speed of the aircraft and the size of the measured particles.	103
A.4	Particle concentrations obtained from one single particle passing the CAS' sampling volume at different airspeeds.	104
A.5	Particle concentrations obtained from one single particle passing the CIP's sampling volume at different airspeeds, for the size range of particles detectable by CIP.	105
A.6	Simulated size distribution for a typical cirrus cloud.	106

A.7	Particle counts and resulting size distributions for an idealized cirrus cloud measurement. One particle at $20\ \mu\text{m}$ is recorded. This single particle has a significant influence on the size distribution averaged for 1 second of flight (yellow). When averaging over 10 seconds (blue line), the single particle's influence on the size distribution is still comparable to the numbers obtained by the the bulk of larger cloud particles. Only when averaging over 100 seconds (red line), the size distribution gives a hint that the small particle was a rare event compared to the frequent occurrence of large particles.	107
A.8	Left panel (a): Overview of measurements during ML-Cirrus: Low concentrations of small particles (CAS size range) could not be detected, although they are simulated to occur in the microphysical model MAID (right panel, b). The colors indicate the associated ice water content. Image taken from Krämer et al. (2016b).	108
A.9	Frequency of occurrence of cloud particle numbers in the ML-Cirrus measurements. 'Single particle events' are more common in the CAS than in the CIP. Figure A.10 explains the background.	110
A.10	Frequency of occurrence of cloud particle concentrations in an ideal case. The yellow curve marks the 'real' cloud particle concentration distribution. The green and red curve show what the CAS and CIP instrument would measure, respectively: all concentrations below the detectable concentration limit cause signals at this detection limit. The actual low concentrations that lead to the peak cannot be derived from the measurements.	110
B.1	Standard NIXElib plot for ML-Cirrus flight 03 on 22.03.2014.	115
B.2	Same as Figure B.1, but with 'single particle event' correction in the CAS data.	116

List of Tables

3.1	Characteristics of the cloud types expected in the mpt regime.	33
3.2	Flight table for COALESC	35
3.3	Flight table for VERDI	36
3.4	Flight table for RACEPAC	37
3.5	Flight table for ACRIDICON	38
3.6	Average cloud particle concentrations for the two cloud types defined in subsection 3.3.1 (see also Figure 3.4), for both small ($D_p < 50 \mu\text{m}$) and large ($D_p > 50 \mu\text{m}$) cloud particles.	41

List of Abbreviations and Acronyms

<i>ACRIDICON-CHUVA</i>	Measurement campaign - 'Aerosol, Cloud, Precipitation, and Radiation Interactions and Dynamics of Convective Cloud Systems/Cloud processes of the main precipitation systems in Brazil: A contribution to cloud resolving modelling and to the GPM (Global Precipitation Measurements)'
<i>AF</i>	Aspherical Fraction
<i>AIDA</i>	'Aerosol Interactions and Dynamics of the Atmosphere'; experiment chamber at KIT
<i>BAHAMAS</i>	Basic HALo Measurement And Sensor system
<i>CAS</i>	See NIXE-CAS
<i>CLaMS</i>	Chemical Lagrangian Model of the Stratosphere
<i>CDP</i>	Cloud Droplet Probe
<i>CIP(g)</i>	See NIXE-CIPg
<i>COALESC</i>	Measurement campaign - 'Combined Observation of the Atmospheric boundary Layer to study the Evolution of StratoCumulus'
<i>CoCIP</i>	Contrail Cirrus Prediction tool
<i>DLR</i>	Deutsches Luft- und Raumfahrtzentrum/German Aerospace Centre
<i>DLR-FX</i>	DLR - Flight Experiments
<i>DMT</i>	Droplet Measurement Technologies (Inc.)
<i>D_p</i>	Particle diameter
<i>ECMWF</i>	European Centre for Medium-Range Weather Forecasts
<i>FAAM</i>	Facility for Airborne Atmospheric Measurements
<i>FSSP</i>	Forward Scattering Spectrometer Probe
<i>GT</i>	Grey threshold
<i>HALO</i>	High Altitude and Long Range Research Aircraft
<i>IAT</i>	Inter-arrival time

<i>ICCP</i>	International Commission on Clouds and Precipitation
<i>IN</i>	Ice nucleus (nuclei)
<i>INP</i>	Ice Nucleating Particle
<i>IWC</i>	Ice Water Content
<i>KIT</i>	Karlsruhe Institute of Technology
<i>MAID</i>	Model for Aerosol and Ice Dynamics
<i>ML-Cirrus</i>	Measurement campaign - 'Mid-Latitude Cirrus'
<i>mpt</i>	mixed-phase temperature
<i>NCAR</i>	National Center for Atmospheric Research
<i>NIXE-CAS</i>	New Ice Experiment - Cloud and Aerosol Spectrometer
<i>NIXE-CIPg</i>	New Ice Experiment - Cloud Imaging Probe - grey scale
<i>NIXE-CAPS</i>	New Ice Experiment - Cloud and Aerosol Particle Spectrometer
<i>OAP</i>	Optical Array Probe
<i>PPD-2K</i>	Particle Phase Discriminator mark 2, Karlsruhe edition
<i>Prob of Occ</i>	Probability of occurrence
<i>PSD</i>	Particle number Size Distribution
<i>RACEPAC</i>	Measurement campaign - 'Radiation-Aerosol-Cloud ExPeriment in the Arctic Circle'
<i>RH</i>	Relative Humidity
<i>RHi</i>	Relative Humidity with respect to ice
<i>RHw</i>	Relative Humidity with respect to water
<i>RICE03</i>	Measurement campaign - 'Rough Ice'
<i>SCS</i>	Scattering Cross Section
<i>SHARC</i>	Sophisticated Hygrometer for Atmospheric ResearCh
<i>SPE</i>	Single Particle Event
<i>SODA2</i>	Software for OAP Data Analysis, version 2
<i>UCAR</i>	University Corporation for Atmospheric Research
<i>UTC</i>	Coordinated Universal Time
<i>VERDI</i>	Measurement campaign - 'Study on the VERTical Distribution of Ice in Arctic clouds'
<i>WBF</i>	Wegener-Bergeron-Findeisen (process or regime)

1 Introduction: Mixed-phase and ice clouds

The earth's atmosphere is usually defined as a layer covering the planet's solid surface, consisting of a mixture of gases: nitrogen (78%), oxygen (21%), argon (1%), water (0-5%), and various trace gases (Wallace and Hobbs, 2006). In the considered atmosphere's temperature range (180 to 330 K), three phases are possible for water: gaseous, liquid and solid (ice). The water vapour percentage is so variable, because water vapour is not mixed homogeneously with the other components: The water vapour capacity of the air decreases with decreasing temperature. During vertical air movements, phase transitions can be triggered. The water vapour capacities sink in uplifts accompanied by adiabatic cooling which leads to supersaturation and, eventually, to cloud particle formation. The formation of liquid and ice cloud particles rapidly decreases the water vapour content of the concerned air parcel. In the same way, the evaporation of a cloud will increase the humidity of the surrounding air. This can occur in sinking air parcels that are subject to adiabatic warming, or when dry air is mixed into a cloud air parcel. Cloud formation and evaporation are therefore key factors in the distribution of water in the earth's atmosphere. Clouds cover approximately 75% of the earth (Wylie et al., 2005). Associated with precipitation and weather changes, clouds have been observed, described and interpreted since ancient times (Frisinger, 1977). In the beginning of the 20th century, the emerging technical possibilities (aircrafts, radar) on one hand and the need of reliable meteorological forecasts for civil and military aviation on the other hand greatly increased the number and quality of cloud studies (Pruppacher et al., 1998). Recently, the increasing demands on weather forecast models have led to a closer investigation of cloud processes. Additionally, the role of clouds as a factor in the climate system has become widely known (Boucher et al., 2013). Cloud tops scatter sunlight back into space and help to cool the earth; at the same time, clouds absorb infra-red radiation that is partially emitted back to the planet's surface, thus contributing to the greenhouse effect. The warming and cooling influence can balance out or one of them can prevail. The microphysical properties of the cloud - particle concentrations, particle sizes, particle phase - determine the cloud's net radiative impact (e.g. Boucher et al., 2013; Ehrlich, 2009). These microphysical properties vary greatly over different cloud types, and in some cases also between clouds of the same category. Clouds can be classified according to their altitude (low, mid-level, high clouds), their temperature (warm, cold clouds) or their cloud particle phase (liquid, mixed-phase - both liquid and ice, ice). Especially for intermediate altitudes, these classification criteria overlap: ice particles may sediment into warm cloud layers; uplifts can transport liquid cloud particles into cold cloud regions, droplet formation may produce liquid

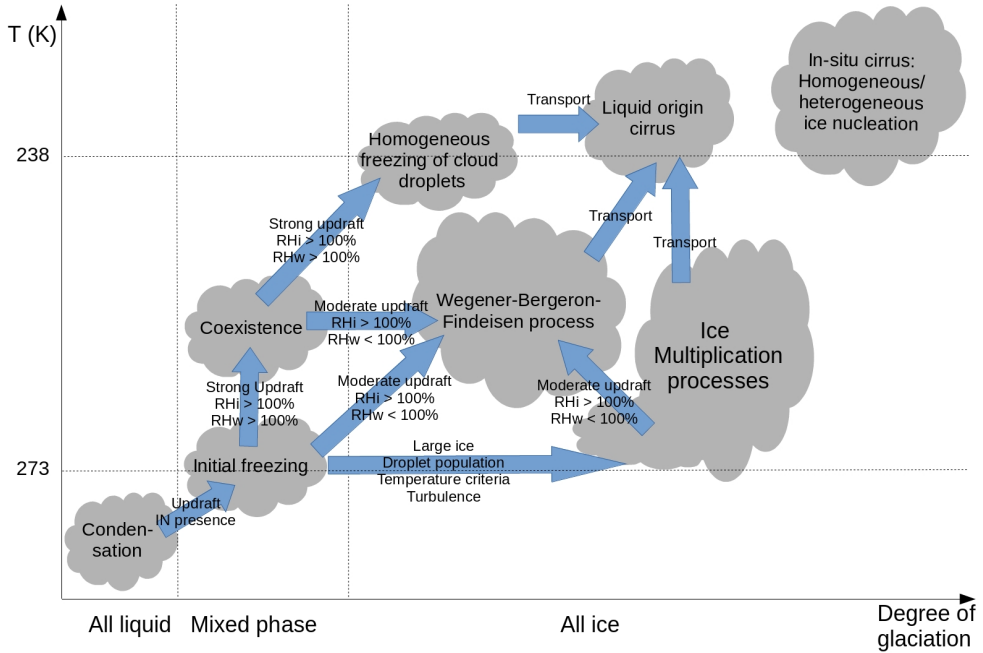


Figure 1.1: Ice clouds in the mid-level and high atmosphere can form under various circumstances.

water content in a cold, formerly fully glaciated cloud (Findeisen et al., 2015; Korolev, 2007a). Figure 1.1 presents an overview of cloud formation and transformation processes from low to high altitudes. Initially, if the cloud formation starts at low altitudes, a warm cloud will form via condensation, as soon as a critical relative humidity with respect to water (RH_w) is reached. This process can also take place at temperatures below 0°C ; in this case, a supercooled liquid cloud is formed. At those colder temperatures below 273 K (0°C), a second relative humidity is defined: the RH with respect to ice (RH_i). If ice nuclei (IN) are present and if the RH_i is above the critical threshold for these IN, initial freezing will produce a small number of ice crystals ('primary ice'). If a sufficient population of supercooled droplets in a certain size range is available, these droplets can freeze when touching the ice crystals, and shed a high number of ice splinters during the rapid freezing process. This is known as Hallett-Mossop process of ice multiplication (Hallett and Mossop, 1974). Other processes such as ice-ice collisions can also produce a large number of small ice crystals. Ice particles resulting from such multiplication processes are called 'secondary ice'.

If strong updrafts keep RH_w and RH_i at values $> 100\%$ after the initial freezing occurred, both the liquid droplets and the ice crystals can persist, thus forming a mixed-phase cloud. In

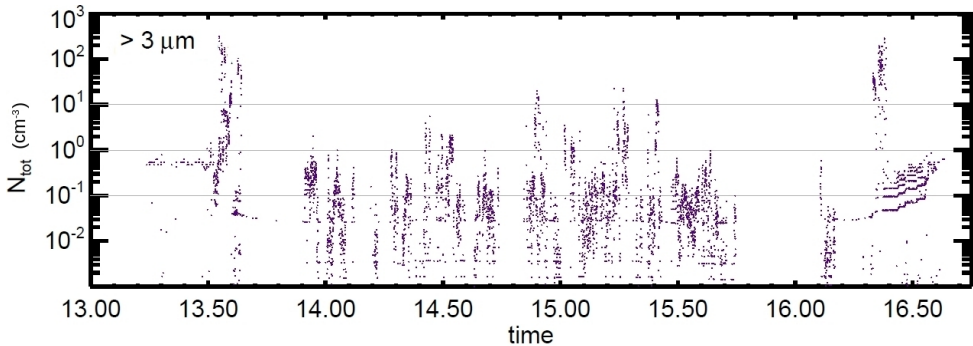


Figure 1.2: Highly variable cloud particle concentrations during ML-Cirrus flight 12.

moderate updrafts, a state with $RH_w < 100\%$ and $RH_i > 100\%$ is more likely (Korolev, 2007a), which allows the Wegener-Bergeron-Findeisen process to happen: Liquid droplets evaporate, while ice crystals grow to large sizes.

Updrafts can carry all of the described cloud types near and below the homogeneous freezing threshold at 235-238 K. At colder temperatures, supercooled water cannot persist; all liquid water will freeze spontaneously. These glaciated clouds fall into the category of liquid-origin cirrus, which was recently defined by Krämer et al. (2016b); Luebke et al. (2016). Also, cirrus clouds can be formed in-situ (ibid.): Heterogeneous ice nucleation creates cirrus clouds via deposition freezing on aerosol particles. Homogeneous ice nucleation causes the freezing of small sulphuric acid droplets (< 200 nm) at high supersaturations.

The microphysical properties of the cloud particle populations undergo many changes as the cloud evolves: The three possible phases (gaseous, liquid, ice), the various possibilities of phase changes (condensation, evaporation, freezing, melting, deposition, sublimation), and the additional cloud feedbacks via radiation cause chaotic patterns of new cloud particle formation, growth and loss. It is therefore not trivial to measure and also to simulate characteristics like cloud particle number concentrations and size distributions that influence - as described above - the cloud's radiative properties.

To characterize mixed-phase and ice clouds, the NIXE-CAPS particle spectrometer (described in chapter 2) was deployed during five airborne field campaigns. NIXE-CAPS has recorded particle number concentrations, particle size distributions, and particle shape information for aerosol and cloud particles over tropical regions (ACRIDICON-CHUVA 2014), mid-latitude regions (COALESC 2011, ML-Cirrus 2014) and polar regions (VERDI 2012 and RACEPAC 2014). Detailed information on the campaigns is given in chapter 3. Additionally, cloud chamber measurements were performed at the AIDA chamber of KIT, Karlsruhe (campaign RICE03, 2014, see subsection 2.2.1). In total, the dataset comprises about 61 hours of 1 Hz data within natural mixed-phase and ice clouds.

With regard to the manifold possible particle populations especially in the mid-level atmosphere, this extensive dataset is used to investigate whether the relative importance of the cloud processes can be determined using simple cloud characteristics. The results are shown in chapter 3.

In the observations, cloud particle concentrations span over more than six orders of magnitude (see Figure 1.2). The last goal of this thesis is to assess how closely simulations can reproduce the microphysical features of observed clouds. This question is investigated in chapter 4, using cirrus cloud observations obtained during the ML-Cirrus campaign (2014).

2 The NIXE-CAPS instrument: Description and data analysis

Cloud particle spectrometer measurements provide insight into the multi-layered, complex structures of cold clouds that cannot be assessed in such detail with remote instrumentation. The following chapter explains the principles of the in situ measurements with the NIXE-CAPS instrument, a two-component cloud spectrometer usually mounted on research aircraft. As NIXE-CAPS has already been described in detail by Meyer (2012); Baumgardner et al. (2001, 2014), the instrument is described here only briefly, while the focus of this work is to illustrate the main uncertainties of airborne in situ cloud observations.

NIXE-CAPS (New Ice eXpERiment: Cloud and Aerosol Particle Spectrometer) is an instrument designed by Droplet Measurement Technologies (DMT), USA. Figure 2.1 shows the instrument dismounted; in Figure 2.2 NIXE-CAPS is installed in a wing pot of the HALO aircraft during the ML-Cirrus campaign.

Two instruments are incorporated in the NIXE-CAPS unit: The NIXE-CAS (Cloud and Aerosol Spectrometer with Detection of POLarization) and the NIXE-CIP-G (Cloud Imaging Probe - Greyscale). Both detect sizes and shapes of particles, saving these information with one time stamp per particle into so-called particle-by-particle files. This information allows the calculation of particle concentrations and number size distributions. In combination, particles with diameters between $0.61\ \mu\text{m}$ and $937\ \mu\text{m}$ can be recorded. NIXE-CAPS thus covers a significant part of the aerosol and cloud particle size range ($3\ \text{nm}$ to $3000\ \mu\text{m}$). It is usually mounted below the aircraft wing, so that during measurement flights, air and particles pass through the sampling areas of the two instruments. The particle information - specified below - are recorded with $1\ \text{Hz}$ (histogram data) and $10^6\ \text{Hz}$ for single particle information, respectively. NIXE-CAS and NIXE-CIP-G use, however, different measurement principles and focus on different particle sizes. These two instrument components will be described in the next section. Three additional components of NIXE-CAPS provide further information: the air speed close to the CIP-G laser beam is measured by a Pitot tube, and a Hotwire is available to perform liquid water content measurements. Furthermore, the NIXE-CAPS has a temperature sensor (not visible in Figure 2.1).

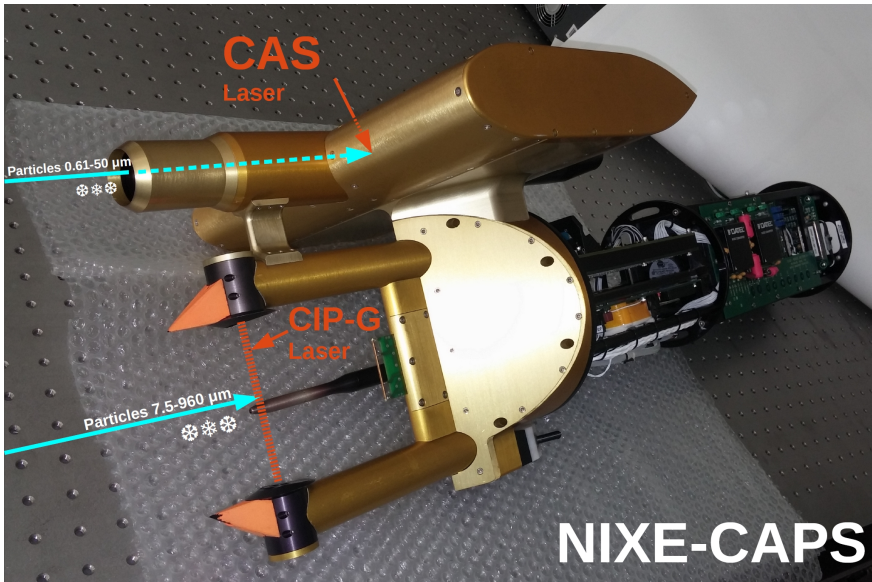


Figure 2.1: NIXE-CAPS dismounted. The upper flat box contains the CAS instrument; its laser beam is hidden in the housing. The CIP laser beam is located between the two arms capped with oranges spikes, which lead shattered particle fragments away from the measurement area. The blue arrows indicate the air flow direction in flight.



Figure 2.2: NIXE-CAPS mounted on HALO.

2.1 NIXE-CAPS: Instrument description

2.1.1 NIXE-CAS-DPOL

The NIXE-CAS-DPOL (in the following: CAS) covers the small particle size range between $0.61\ \mu\text{m}$ and $50\ \mu\text{m}$. It consists of an inlet tube pointing in the direction of the flight, into which cloud particles enter. In the middle of the tube, they pass a laser beam and scatter its light. This event is recorded by four sensors: two measure the intensity of the forward scattered light, two more the backward scattered light. The width of the laser beam and its DOF (depth of field) define the CAS' sampling area. The actual sampling volume, the basis for the calculation of the particle concentrations, depends on the airspeed (usually the cruising speed of the aircraft, in laboratory setups the speed of the particle flow). The recorded forward scattering intensity is used for particle sizing. The backward scattering intensities are modified by a polarization filter, thus giving information about the sphericity of a particle. For a detailed schematic view of the CAS instrument, see Figure 2.3.

The CAS laser beam is hidden in the CAS housing (see Figure 2.1). Inside the CAS tube, it crosses the air flow through the instrument on a path approximately 5 cm long. The focus area of the laser beam is smaller - approximately 1 mm long - and is located in the middle of the CAS tube. Only cloud particles passing this part of the laser beam are taken into account in the CAS measurements.

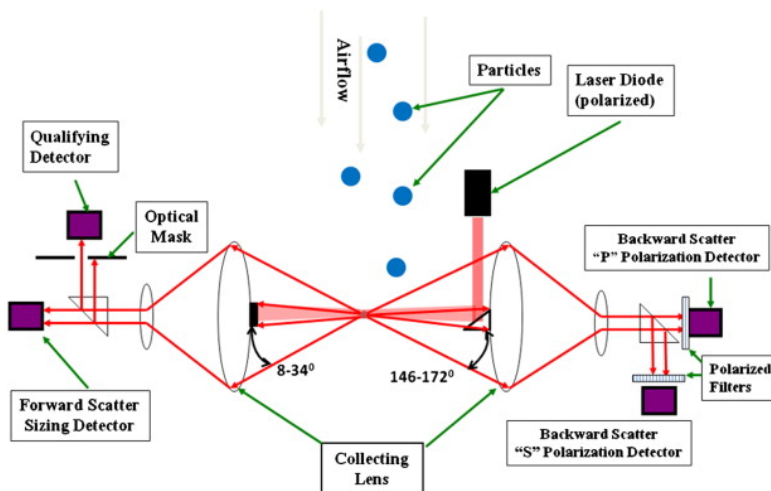


Figure 2.3: Schematic setup of the CAS instrument. Monochromatic polarized laser light is scattered by particles entering the beam. The scattered light is measured a) in the forward direction by two sensors, the sizing detector and the qualifying detector, and b) in the backward direction by two sensors, one who measures the backwards scattered p-polarized light and a second one measuring the s-polarized component. Image taken from Baumgardner et al. (2014).

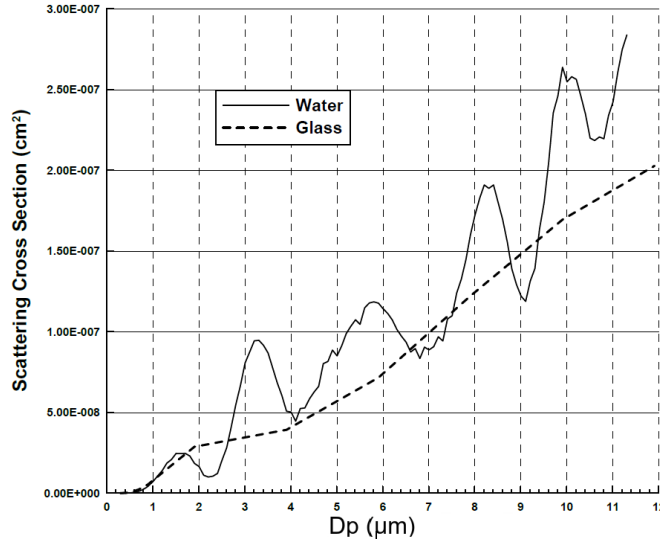


Figure 2.4: Scattering cross sections (SCS) of spherical water and glass particles. For water particles, the SCS for varying particle sizes are not unique. To perform particle sizing with the obtained SCS, size bins have to be applied that are constrained at unique values. Dp: Particle diameter. Image taken from DMT (2009).

Measurement principle

This paragraph summarizes the description of CAS in Meyer (2012) and DMT (2009).

In clear air, no light reaches the four detectors within the CAS. The laser beam itself is blocked by a 'blind spot'. When a particle enters the CAS laser beam, however, it scatters the laser light in a pattern that depends on i) the particle size, ii) the particle shape, iii) the particle's refractive index and iv) the wavelength of the incident light.

A fraction of the forward scattered light is collected by a lens and transferred to the sizing detector. The sizing uses the following assumptions: Particles are considered to have the refractive index of liquid water (1.33). For the first guess, particles are assumed to be spherical. Since the laser beam is monochromatic (wavelength 638 nm), these assumptions allow to calculate expected intensities of the forward scattered light using the Mie theory (Mie, 1908). These scattering cross sections only depend on the particle's size.

The recorded scattering cross sections can, however, not directly be related to particle sizes. For spherical liquid water droplets, the scattering cross sections of particles with varying diameters are not unique (see Mie (1908) and Figure 2.4). The sizing procedure has to take these Mie ambiguities into account. To avoid mis-sizing, the CAS size bins have to be placed in a way that allows a definite classification of each particle within the bin borders. Due to this, the initial number of 30 size bins is reduced to 16 size bins in the CAS data evaluation.

Before reaching the forward scattering sensor, the forward scattered light passes a beam splitter where a fraction is directed to a second sensor. Particles that pass the laser beam outside the focus area (DOF) will cause a detectable ratio between this redirected fraction and the signal on the forward scatter sensor. Based on this ratio, the CAS will reject particles that are outside its DOF.

The particle sizes are calibrated by the manufacturer. For measurement campaigns, it can be checked by inserting borosilicate beads of defined sizes into the CAS laser beam on ground, usually after every measurement flight. The refractive index of borosilicate differs from liquid water and ice, which causes the CAS electronics to sort the beads into wrong size bins. Since the refractive indices are constant, this method is nevertheless suited to prove the functionality of the CAS sizing. Wrong sizing can indicate problems of the laser or contaminated laser windows. During field campaigns, these windows have to be cleaned frequently from dust, soot and ash.

2.1.2 NIXE-CIP-G

The NIXE-CIP-G (CIP) is an optical array probe (OAP) that nominally records particles between $7.5\ \mu\text{m}$ and $960\ \mu\text{m}$. It is an open-path instrument, its sampling volume is located between the two orange tips in Figure 2.1.

Measurement principle

A laser beam crosses this open section and is reflected after re-entering the instrument, so that it enlightens a sensor array of 64 square diodes (width: $15\ \mu\text{m}$ each) that are set in one line perpendicular to the direction of flight. These diodes measure the intensity of the incoming laser light; the frequency of the measurements depends on the air speed between the CIP arms.

Data processing

Particle sizes and concentrations are derived from their CIP images by the SODA2 program, provided by A. Bansemmer (NCAR/UCAR, 2013). For a detailed description of this program, see for example Frey (2011). Appendix B describes which options can be chosen when running SODA2.

As a particle passes the CIP laser beam, its shadow shades the diode array for a certain time. The CIP sensor array detects light intensities of 100%-65%, 65%-35%, and 35%-0% (full shadow). Records are taken with an airspeed-dependant rate; these single 'slices' can later be recomposed to particle shadow images. The image rate is higher the faster the air flow between the CIP arms is, so that even fast particles are 'photographed' with enough image slices (DMT, 2009). A certain amount of particles is recorded temporally in a buffer. The data are written on the CIP memory card a) when the buffer is full, but also b) at least once per second.

From the detectable size range between 7.5 and $960\ \mu\text{m}$, only 22 - $937\ \mu\text{m}$ is used. Electronic noise can produce artificial signals that are counted as particles in the size range below $22\ \mu\text{m}$.

On the other end of the size spectrum, particles with a diameter of $960\ \mu\text{m}$ would cover all 64 diodes. For such particles it cannot be excluded that they are even larger; the shadow image might only show a partial shadow. Also, particles which are not in the middle of the sampling area can cause partial images touching the borders of the CIP image array. This can be treated in two different ways: either, only particles that do not touch these borders are considered to be valid ('allin' method); in this case, the effective sampling volume of the instrument is small. Alternatively, the 'reconstruct' method can be chosen: Here, particle shadows that touch the image border are reconstructed into full particle images, assuming that the particle center was recorded in the image. This method comes with large uncertainties and is usually not employed, as further explained in the following.

The effects of choices in grey threshold and image method ('allin'/'reconstruct') were evaluated in greater detail (work in cooperation with Anna Luebke). Figure 2.5 shows an excerpt of the findings:

In both of the investigated cloud segments, the choice of settings influences the diagnosed particle size distribution. The first case (left panel) shows a cloud with a diameter mode around $400\ \mu\text{m}$. Here, many cloud particles fit easily into the sampling area of the CIP instrument without touching the array borders, so that there are no significant differences between the 'reconstruct' or 'allin' method. When only the core shadow of a particle is considered ('GT 2'), the particle size distribution is shifted towards smaller diameters, because the outer region of the shadow images are ignored. Especially for partially transparent ice crystals, this method may lead to underestimated maximum diameters.

In the second case (right panel of Figure 2.5), the cloud consists of very large rosettes and aggregates close to the detector array extent. In this case, the choice of 'reconstruct' or 'allin' method has a stronger influence on the particle size distribution than the choice of the grey threshold. The 'allin' analysis finds a larger concentration of particles with the maximum detectable size: With this setting, more particles get rejected, but the few remaining ones are related to a significantly smaller sampling volume than it would be the case for the 'reconstruct' setting (see Heymsfield and Parrish, 1978, a detailed explanation is given in section 2.4, see also Figure A.3). Although the sampling statistics, and thus the confidence in the data, are low for large particles, the 'allin' setting is subject to smaller uncertainties. The 'reconstruct' mode employs algorithms to estimate the geometrical center of the partial image and then 'reconstructs' the missing part using the maximum distance between this center point and the visible edge of the image. It thus assumes that all ice crystal images have a symmetric geometry, and that the center of an image is always visible. Both assumptions are subject to large uncertainties. Also, the method complicates concentration calculations due to the unknown effective sampling area. Therefore, in the CIP data used in this thesis, only particles are accepted whose shadow does not touch the borders of the diode array ('allin' method).

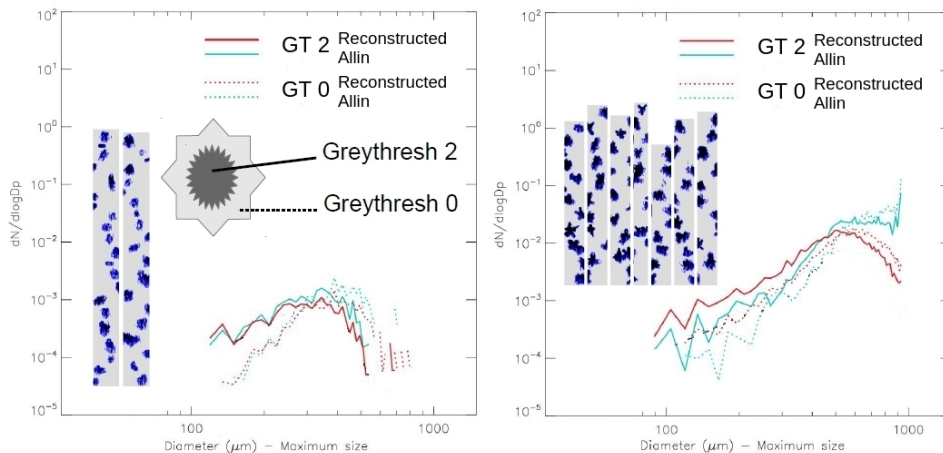


Figure 2.5: CIP image data were evaluated with different settings for two cloud situations. 'Allin' means that only particles that do not touch the borders of the array were accepted. In the 'Reconstructed' mode, an estimated diameter is calculated for particles which extend over the array borders. 'GT 0' means 'grey threshold 0': here, all shaded areas are counted as particle pixels. 'GT 2' restricts the image area to core shadow pixels (grey threshold 2: at least 65% shading). Image: courtesy of Anna Luebke.

2.2 Particle asphericity

2.2.1 NIXE-CAS: Description and verification in AIDA cloud chamber experiments

The backward scattering signal is used to identify aspherical particles. The measurement is based on the assumption that spherical particles hardly change the polarization of the laser light, while aspherical particles will do this. Like the forward scattered light, the backscattered light is split into two fractions by a beam splitter (Figure 2.3). One fraction is filtered by a p-pol filter. The second part passes a s-pol polarization filter which removes the fraction of light whose plane of polarization has not been altered by the particle in the laser beam. Aspherical particles are expected to cause strong s-pol signals. Spherical particles will ideally cause no signal on the s-pol detector, or a very weak signal: as the detector does not restrict the measurement of the intensity to the plane of incidence, but over a certain angle, light that is not s-polarized might still cause a weak signature (Meyer, 2012).

Since the intensities of all scattering signals are additionally size dependant, the s-pol backward scattering intensity has to be assessed with regard to the particle size detected by the forward scattering sensor. Thresholds have to be defined - over the whole CAS size range - that allow the differentiation between spherical and aspherical particles. These size-dependant values are found by using 'calibration' measurements in warm clouds > 0 °C, where it can be assumed that all recorded particles are liquid and therefore near spherical (see first panel in Figure 2.7). For

each size bin, the highest s-pol backward scattering intensity counts that are found in this warm cloud defines the maximal value that are accepted for spherical particles. All higher counts are then assumed to be caused by aspherical particles. Since small changes in the instrument setup, the gain stage setup or the laser intensity might change these threshold values, regular checks are performed before and during each NIXE-CAPS field campaign. Optimally, the 'warm cloud calibration' is performed for each measurement campaign separately, using warm cloud measurements performed during the respective campaign.

In general, small particles cause weaker backscatter signals than large particles. To be able to record all particles in the CAS size range, amplifiers are used. The sensors' signals are recorded in three gain stages, enlarging especially the signatures of small particles. Which gain stage is used for each specific particle is again defined by the sizing performed by the forward scattering sensor.

A second variation in the backscattering signals of aspherical particles is caused by the particles' orientation in the laser beam. Depending on the crystal shape and orientation, even strongly aspherical particles can cause only weak s-pol signals (Nicolet et al., 2007; Baumgardner et al., 2014). Due to this uncertainty, the asphericity analysis is not done for single particles, but for larger populations. Thus it can be assumed that in ice clouds, enough particles cause detectable s-pol values. Note that due to this uncertainty, all aspherical fractions (percentage of aspherical particles per second) are minimum values - the largest detected aspherical fractions did not exceed 70-80% even in cirrus clouds (cf. 3.3.3).

To gain experience in the interpretation of CAS data and to compare the instrument's performance with other detectors for cloud particle sizing and shapes, experiments have been performed at the AIDA chamber of the KIT, Karlsruhe. AIDA stands for 'Aerosol Interactions and Dynamics in the Atmosphere'; the chamber is described e.g. in Möhler et al. (2003). During the AIDA campaign RICE03 in 2014, the cloud particle aspherical fraction measured with NIXE-CAS have been compared to the AIDA instrument PPD-2K (Particle Phase Discriminator mark 2, Karlsruhe edition). For details and scientific background of this study see Järvinen et al. (2016).

At the AIDA chamber, clouds can be produced under controlled conditions. Aerosol and water vapour input help to control particle sizes; initial temperatures and cooling rates control the conditions under which the cloud particles form and evolve.

An AIDA experiment was performed with the phases (a) formation of a liquid cloud, (b) beginning freezing process, (c) late freezing process, and (d) fully frozen cloud (Figure 2.6). Figure 2.7 shows the s-pol intensity measurements of the NIXE-CAS during those four stages of the experiment. They show the particle shape changes during the experiment:

- a) liquid droplet phase: These particles - with s-pol signals up to 100 - are assumed to be spherical (see also Järvinen et al., 2016). Note that large, spherical particles are missing:

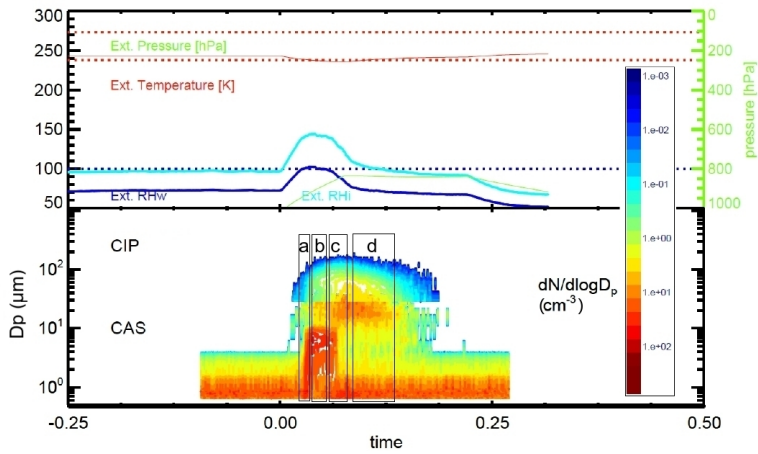


Figure 2.6: In this AIDA experiment (RICE03, Exp. 20) a water cloud was generated which froze as the chamber was cooled down. Panel 1 shows the development of temperature, pressure and relative humidities wrt water/ice with time. Panel 2 shows the NIXE-CAPS particle size distributions with time. As the cloud is initiated, a large number of small droplets forms, along with few large ice crystals that froze heterogeneously. When the relative humidity with respect to water sinks below 100%, the droplets evaporate and the ice particles grow.

Due to high aerosol (ice nuclei) concentrations, the available water vapour is distributed among a high number of small droplets, thus limiting their growth.

- b) As the freezing starts, a few larger particles appear; their s-pol signals are well above the threshold for spherical particles.
- c) Seconds later, the large particle fractions with high s-pol signals is growing.
- d) The liquid droplets have evaporated; ice particles have grown (Wegener-Bergeron-Findeisen process). The cloud is fully frozen; larger ice particles appear. These ice particles show a strong s-pol signal. Nevertheless there still is a significant number of particles with weak s-pol signals (< 100) that are classified as 'spherical'. This demonstrates that spherical particles cannot be used as a proxy for liquid water: The temperature at this moment is below 238K, all cloud particles must be frozen (see again Järvinen et al., 2016). Note also that the aerosol section below $3 \mu\text{m}$ has become smaller: During the cloud formation, especially the larger aerosol particles were consumed.

For spherical particles, the measurements have shown a good agreement between both instruments. The NIXE-CAPS was able to accurately define liquid water droplets and spherical ice crystals as spherical, which shows that the classification algorithm depends on the shape alone, not on the particle phase (see Järvinen et al., 2016).

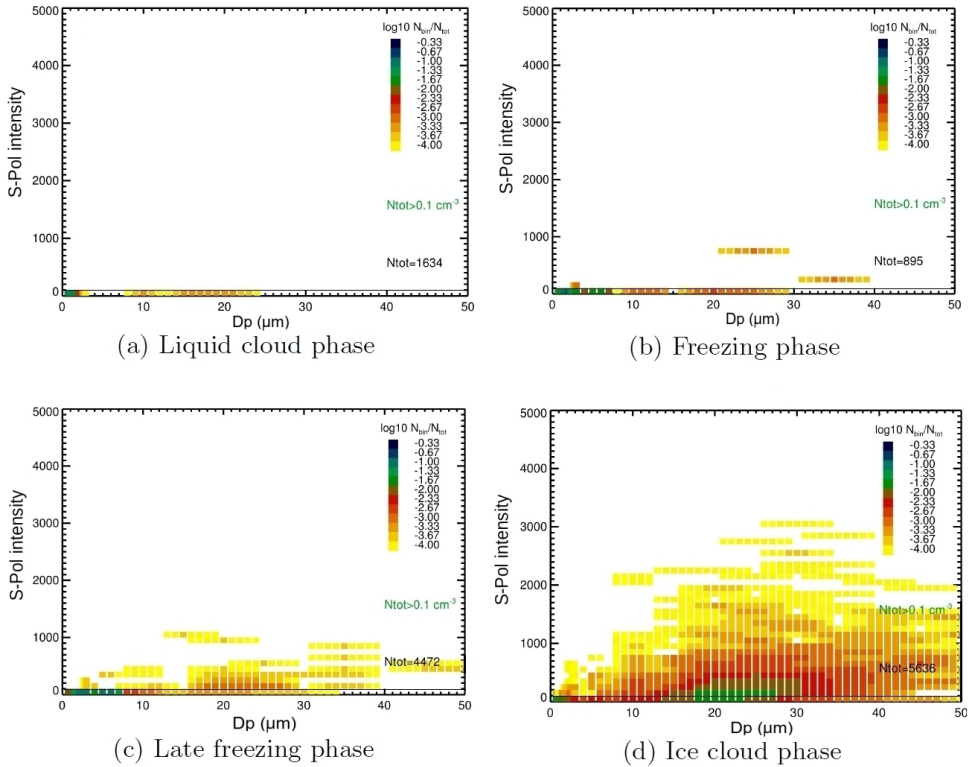


Figure 2.7: Measurements of cross-polarized light in the backscatter direction as an indicator for particle sphericity during experiment 20, RICE03. Each particle is characterized by a size value, obtained via the forward scattering measurement, and a backward cross polarized intensity (see subsection 2.1.1). The color depicts the frequency of occurrence; the darker the color, the more particles with the respective characteristics were found. a) liquid droplet phase, b) at the initial freezing, few larger particles appear; their backscatter intensities are well above the threshold for spherical particles. c) Seconds later, the small round particles start to disappear, with the large, aspherical fraction growing. d) The remaining ice particles show a strong backscatter intensities.

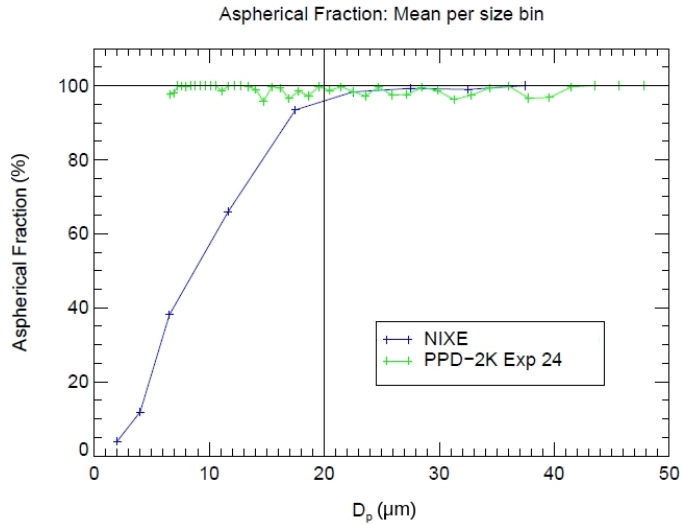


Figure 2.8: Comparison of the aspherical fractions obtained by NIXE-CAPS and PPD-2K (Järvinen et al., 2016). D_p stands for particle diameter. The NIXE-measurements become insensitive to aspherical particles for particle sizes smaller than $20 \mu\text{m}$. For this reason, the NIXE total aspherical fractions only cover particles larger than $20 \mu\text{m}$.

The RICE03 campaign has brought a second important result: For aspherical particles, the NIXE-CAPS instrument has been shown to suffer from a considerable insensitivity towards the asphericity of small particles with diameters lower than $20 \mu\text{m}$. Measurements in artificial clouds consisting of pristine ice columns yielded a lower detected asphericity the smaller the particle size was Figure 2.8. This adds to the uncertainty of the asphericity data obtained by the CAS and has to be taken into account when computing ‘overall aspherical fractions’ over the whole CAS size range (cf. chapter 3). For the analyses presented in chapter 3, only aspherical fractions of particles between $20 \mu\text{m}$ and $50 \mu\text{m}$ are used.

2.2.2 NIXE-CIP: Description of the asphericity analysis

Korolev and Sussman (2000) have developed an algorithm to assess the particle shapes of the CIP shadow images.

The CIP images are examined using the particle shadow image’s circumference; this value is compared to the circumference of a spherical particle image with the equal number of shadowed pixels. The ratio defines the ‘sphericity’ of the particle. A minimum of 7-10 pixels of particle diameter is required for this algorithm (as shown by Paul Lawson, ICCP workshop, Boston 2014); particles with diameters between 50 and about $100 \mu\text{m}$ can therefore not be included in the shape analysis. The CIP images are taken in a resolution of $15 \mu\text{m}$, which restricts any

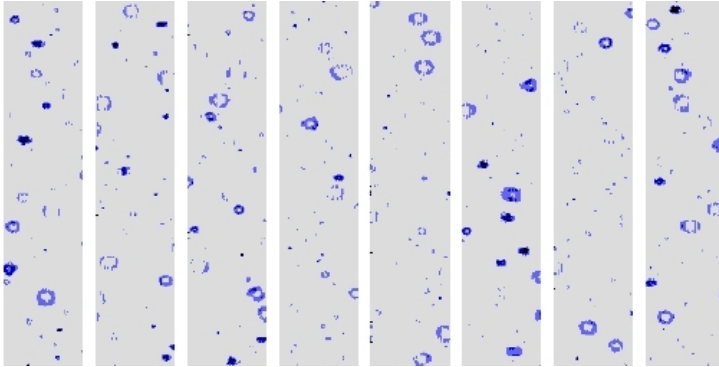


Figure 2.9: CIP images of ice plates during ML-Cirrus Flight 02, 21.03.2014.

image analysis to particles larger than about $100\ \mu\text{m}$ in diameter, as all other particles do not contain enough pixels to apply the algorithm. Due to this, a large fraction of the particles can not be assessed at all, and the others are subject to a large uncertainties regarding the CIP image asphericity analysis. Additionally, as shown in the previous section, the grey threshold chosen for the image analysis can strongly influence the detected particle image.

In general, this shape recognition method has to be used with care. We learned from careful inspection of many observations that it likely misclassifies hexagonal ice plates and similar particles as 'spherical' (see e.g. Figure 2.9). It is therefore not used in the frame of this work.

2.3 NIXE-CAPS data evaluation

The NIXE-CAPS data sets can be evaluated with the IDL routine library NIXElib (see also Meyer, 2012; Luebke et al., 2016). The raw data formats and evaluation procedures are described in more detail in Appendix B. Figure 2.10 shows the standard overview plot produced by the NIXElib, including the most important data products as a function of the experiment time:

- external data such as temperature, pressure, and humidity (top panel),
- particle size distributions (second panel),
- total particle concentrations for the aerosol and cloud particle fraction (middle panel),
- concentrations of spherical and aspherical cloud particles as well as aspherical fractions (forth panel), and
- the distribution of aspherical fractions over the measured size range (bottom panel).

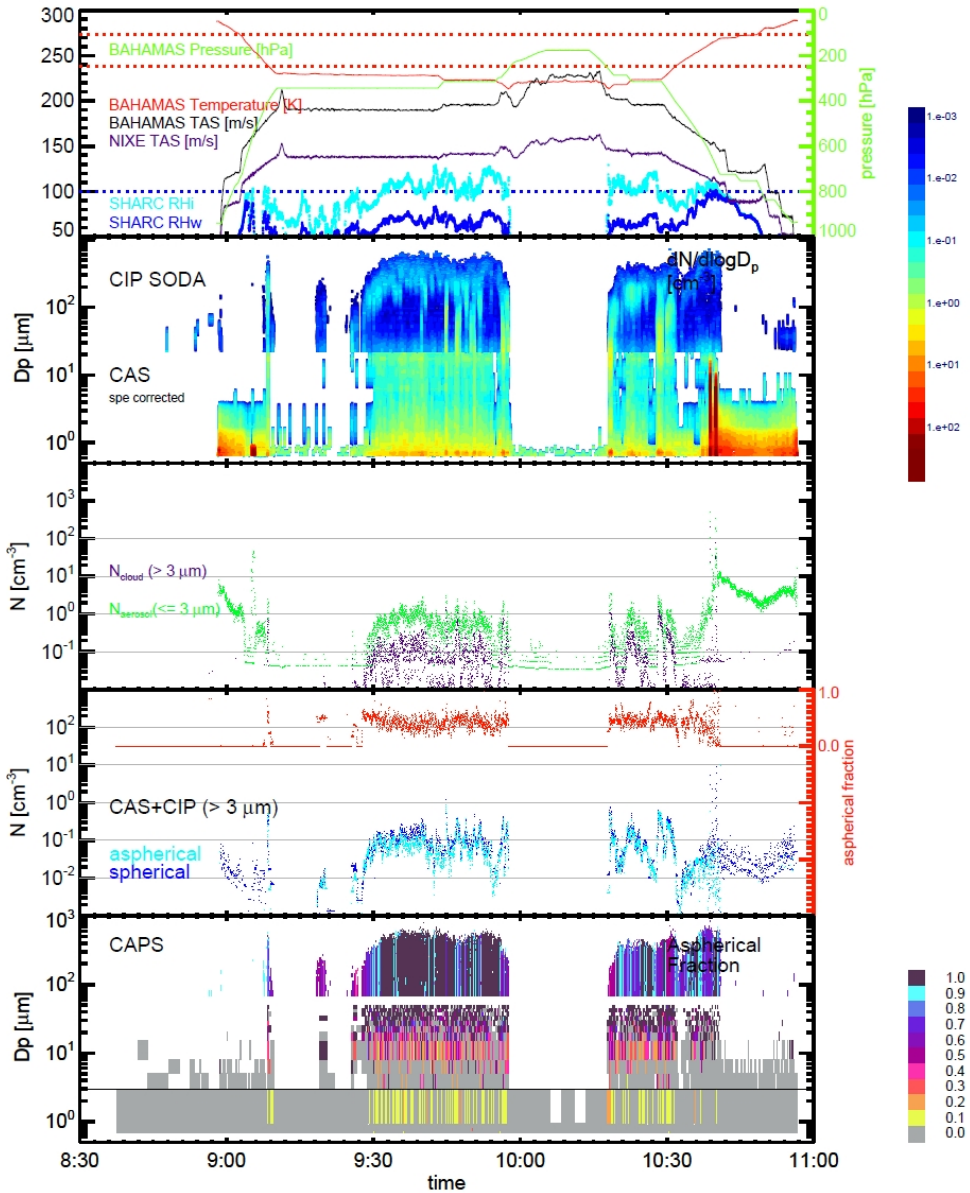


Figure 2.10: Same as Figure B.1, but with 'single particle event' correction in the CAS data.

2.4 Sampling volume effects: 'Single particle events'

Krämer et al. (2016b) suggest possible cirrus cloud particle concentrations between roughly 0.001 cm^{-3} and 10 cm^{-3} , covering a wide range of possible atmospheric conditions. The concentration spectrum is expected to shift depending on the dominant cloud type (Luebke et al., 2016). Various datasets of cirrus cloud particle number concentrations, however, show an unexpected feature in this spectrum: A sharp peak in the frequency of occurrence at intermediate concentrations close to 0.01 cm^{-3} (see top panel Figure 2.11). This peak can not be explained by any theoretical contemplation of cloud evolution, and it is not restricted to specific particle measurement instruments (compare bottom panels in Figure 2.11). It is caused by statistical effects due to the measurement design, as elaborated in detail in Appendix A. This section provides a short summary of the findings.

A closer look at the NIXE-CAPS cloud particle concentration frequency spectrum during the ML-Cirrus campaign shows that such peaks occur at the lowest detectable concentration for each instrument (see Figure 2.12). The high occurrence of this narrow concentration range might hide other patterns in the occurrence of cirrus cloud particle concentrations and shift the median values that are used as input and validation parameter for global models (e.g. Wang and Penner, 2010; Liu et al., 2012; Wang et al., 2014). The explanation and removal of this feature are therefore important to provide reliable particle statistics.

The high occurrence of certain cloud particle concentrations is caused by sampling volume limitations, as shown in Appendix A. It concerns instruments whose measurable concentration range ends not at the lower edge of possible cloud particle concentrations, but in the middle of this range. When clouds with lower particle concentrations are probed, these lower concentrations cause a signal at the minimum detectable concentration of the respective instrument.

Due to the wide range of low cloud particle concentrations that can cause 'single particle events', the occurrence of one particle per bin and time unit can not be interpreted. Therefore, the particle concentration caused by one single particle in the respective instrument should be excluded from the measurable concentration range. This approach clears the dataset from the artificial concentration feature at the instrument's detection limit, as can be seen in Figure 2.13. The resulting minimum measurable concentration will depend on the instrument's sampling area and the air speed at the respective measurement. These limiting factors have to be pointed out when describing the dataset. 'Single particle events' might be less common if the measurements are averaged over larger time periods. The considered time interval can be adapted according to the required spatial resolution of the measurements.

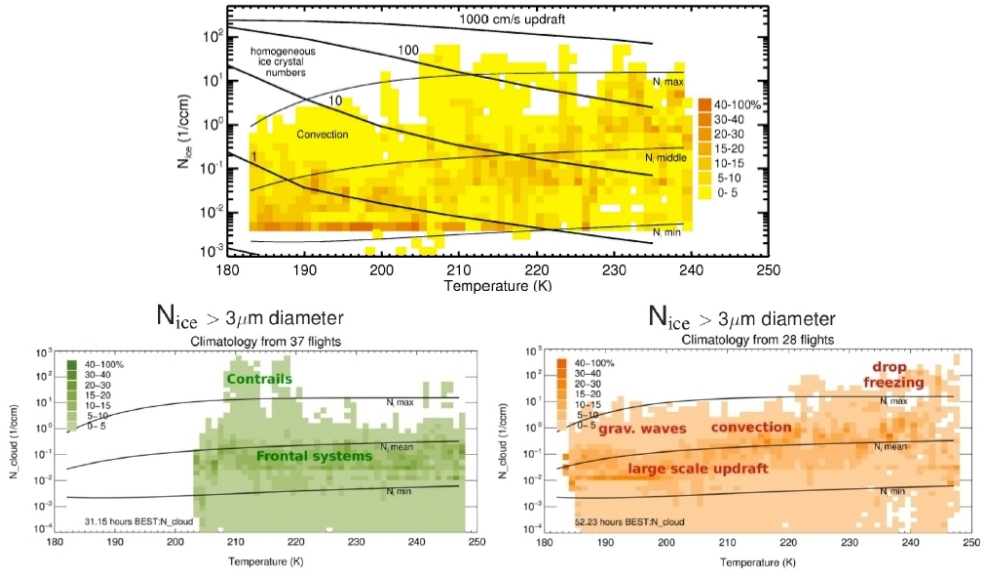


Figure 2.11: Top: Frequency of occurrence of particle concentrations measured with an FSSP instrument, which has a sampling volume comparable to the NIXE-CAS. Image taken from Krämer et al. (2009). Bottom: Frequency of occurrence of particle concentrations measured with the NIXE-CAPS in cirrus clouds (bottom left panel), in combination with a fast CDP in tropical cirrus (bottom right panel). Images taken from Krämer et al. (2016a).

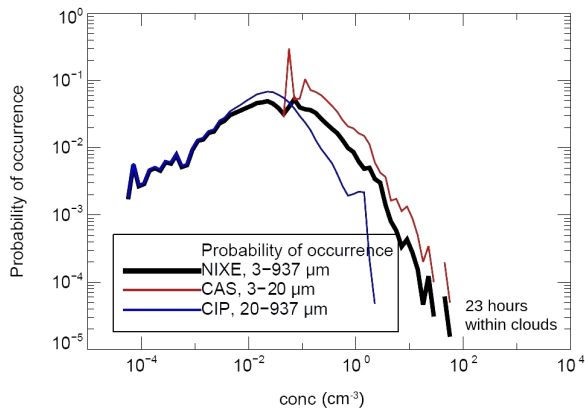


Figure 2.12: Frequency of occurrence of cloud particle concentrations in the ML-Cirrus measurements.

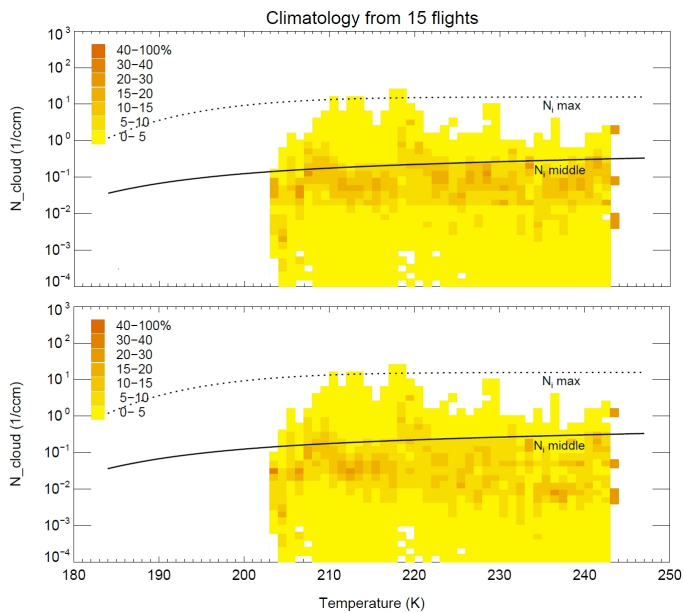


Figure 2.13: Frequency of occurrence of cloud particle concentrations measured with NIXE-CAPS during ML-Cirrus 2014. Top panel: Original dataset, bottom: dataset after 'single particle event' correction. Plot: Courtesy of Nicole Spelten.

2.5 Sources of measurement uncertainties

2.5.1 Particle sizing

Meyer (2012) report a sizing uncertainty of about 20% for the CAS due to laser beam inhomogeneities, particle shape influences and more. An additional sizing uncertainty is induced in mixed-phase clouds, when the refractive index of liquid water is applied on the small - potentially frozen - particles. This causes sizing errors up to about 15% (Meyer, 2012).

The particle sizing of the CIP instrument is subject to an uncertainty of $\pm 20\%$ and a possible overestimation of particle sizes by up to $20\ \mu\text{m}$ due to the CIP's optical setup: A sensor diode is $15\ \mu\text{m}$ wide, and 35% shadowing intensity are sufficient to trigger the particle detection (see subsection 2.1.2). This effect makes it necessary to discard the smallest particles in the CIP dataset, as their sizes are subject to large errors. However, this error becomes less significant with growing particle diameters.

2.5.2 Particle shattering (CAS, CIP)

When clouds consisting of large ice crystals are probed, these crystals can hit the instrument housing and shatter into small pieces (Korolev et al., 2011). These pieces artificially enlarge the measured cloud particle number concentrations of small particles. To correct for these shattering events, an interarrival time (IAT) correction can be applied (Field et al., 2006). This algorithm is based on the assumption that the shattering fragments will arrive very close to each other in the sampling volume, i.e. with very short inter-arrival times. Two ways of applying this correction are possible: i) a predefined IAT threshold can be set, all IATs smaller than the threshold will lead to a rejection of both particles; and ii) IAT histograms can be created that show two IAT modes when shattering occurs: the regular cloud's average IAT and a second peak at small IATs. The IAT value between the two peaks will then be used to define a local IAT threshold below which particles are rejected.

Other instruments similar to the CAS, e.g. the FSSP, have been shown to produce shattering artefacts (Korolev et al., 2011). The NIXE-CAS has been modified to avoid such events. In particular, the inlet tube's edges have been sharpened (Meyer, 2012). After this modification, the IAT correction algorithm does not longer alter the data. Also, Korolev et al. (2011) have shown that a modified inlet tube reduces shattering events to a minimum.

Analogue to the CAS, an interarrival time (IAT) correction for CIP particles can be applied. So-called Korolev tips have been attached to the instrument (Korolev et al., 2013) to minimize ice particle shattering (see comparison study in Korolev et al., 2011). To clear the datasets from the shattering events that still take place, particles can be rejected if the IAT between them is below a certain threshold (analogue to the CAS, Field et al., 2006). The combination of Korolev tips and the rejection of CIP particles smaller than $22\ \mu\text{m}$ results in a low impact of shattering on the NIXE-CIP data, as shown in Figure 2.14, where different types of clouds are

analyzed for shattering. No cloud type shows high occurrence of short IATs in both CAS and CIP, not even cumulonimbus anvils and cirrus clouds probed during AC18, which consisted of large ice particles up to $900\ \mu\text{m}$.

It is important to note that the IAT rejection method by Field et al. (2006) fails when particles shatter not immediately before the sampling area, but e.g. on the aircraft's body; their IAT time might then be comparable to the one of the cloud particles. In very dense clouds, on the other hand, the IATs are always very short. In these cases, too, the Field et al. (2006) method can not be used. As Figure 2.14 shows, however, the IAT rejection is not expected to have a significant influence on the NIXE-CAPS data in any case. It is therefore only used when the experiment conditions suggest that the danger of shattering is larger than usual, for example when probing snow or other very large particles with diameters $> 1000\ \mu\text{m}$. In the cloud studies presented here, no IAT correction is applied.

2.5.3 Poisson spots (CIP)

Due to diffraction, a bright spot can appear in the middle of shadow images of spherical particles (Korolev, 2007b; DMT, 2009, with image examples). The size of the spot increases with increasing distance of the particle from the focal point of the laser beam. A careful analysis of several measurement campaigns has shown that these so-called Poisson spots usually occur in clouds, where small and large liquid water droplets coexist with ice particles. The total number of erroneous images is small compared to the absolute number of particles in this cloud regime (see Figure 2.15). In contrast, an overcorrection is possible: the Poisson spot correction may wrongly recognize and 'correct' hexagonal ice plates that appear as ring shapes in the CIP images (see also Korolev, 2007b). Due to this and because the benefits are negligible, the algorithm is not used for the studies presented in this thesis.

2.5.4 Artificial particles (CIP)

During the airborne campaign ML-Cirrus in 2014 (cf. chapter 4), an additional CIP data correction was necessary due to the combination of aircraft wing vibrations that occurred on the fast flying aircraft HALO and very low ambient temperatures during the measurements. Under these conditions, a certain set of diodes in the CIP sensor are more sensitive to small light intensity fluctuations and frequently created artificial 'particle' signals when vibrations occurred. To a smaller extent, this behaviour was already observed in the earlier COALESC campaign (2011, cf. chapter 3), using the slower aircraft BAe-146.

Each diode's sensitivity can be changed manually; it is therefore possible that the concerned diodes react more sensitively to the vibrations and other influences than the others. This 'noise' in the CIP data was always caused by the same diodes (mostly diodes 17, 29 and 45), thus forming a regular pattern in the CIP image record. A filter was applied during the data evaluation procedure using this regularity: 'Noise buffers' are defined as those buffers where the

affected diodes cause concentrations of more than 2/3 of the maximum concentration found at that time, while the unaffected bins in between show less than 1/3 of the maximum concentration (see Figure 2.16). These 'noise buffers' are rejected, which means that no particle from these time sequences are counted into the total concentrations.

Whenever the 'noise' occurred within clouds thicker than about 0.01 cm^{-3} , the buffers were not rejected any more, because the relatively few artificial particles didn't make the sensitive diodes stand out among the others, i.e. the noise is not longer detectable. For these cases, an error estimation has to be made by taking into account two information:

- The number of 'noise' counts per second is limited. The influence of artificial particles on the total particle concentration decreases therefore with an increasing number of real cloud particles. In cloud-free air, on the other hand, all artificial particles are detected and removed.
- In the ML-Cirrus flights, where the occurrence of CIP noise was higher than in all other campaigns, the 'noise buffers' never caused artificial particle concentrations higher than 0.01 cm^{-3} in cloud-free air.

Since the signals from the noise diodes have to dominate the total signal of a buffer to trigger the noise correction, only time periods with weak signals in the other diodes can actually cause errors. In this case, the largest possible error on the counts per second is 18%. The effect on the particle number concentration will be lower, because the artificial particles usually trigger only one, maximally two diodes per second. For these 'small' particles, the assumed sampling volume is larger than for other particles (see section 2.4). Since $\text{conc} = N/SV$ (N = number of particles, SV = sampling volume; see section 2.4), this will scale down the influence of the artificial particles further. The 'noise' error decreases rapidly as the cloud particle concentration grows, because the number concentrations of 'noise' particles remains below 0.01 cm^{-3} per time unit. For that reason, an error estimation in warm or mixed-phase clouds is unnecessary, as these clouds' concentrations usually lie around several hundred cm^{-3} (see chapter 3).

2.5.5 Particle coincidence (CAS)

With such high concentrations in warm or mixed-phase clouds, it is possible that more than one particle passes the laser beam at the same time. This phenomenon causes 'particle coincidence errors'. Previous studies have found that this error can lead to a serious underestimation of particle concentrations, starting at measured concentrations of about 500 cm^{-3} (Lance, 2012). Lance (2012) suggest a correction formula based on the probability for these coincidence measurements, which depends on the observed cloud particle concentration. The NIXE-CAPS dataset was so far not corrected for coincidence, because sufficiently high particle number concentrations were either not reached (ML-Cirrus 2014, AIDA campaigns, ACRIDICON/Zugspitze) or were

irrelevant to the scientific analysis (ACRIDICON-CHUVA 2014, COALESC2011, VERDI2012, RACEPAC2014; cf. chapter 3).

2.5.6 Total concentrations, total masses (CAS and CIP combined)

The measurement uncertainty of the NIXE-CAPS concentration measurements is estimated to be about $\pm 20\%$ (Meyer, 2012; DMT, 2009) due to the effects described in the previous sections. Since mass calculations are influenced by both concentration and size uncertainties, their uncertainty is larger (cf. Figure 2.17). For mass calculations, the uncertainties with respect to concentrations, particle sizes and particle phase (liquid water or ice) sum up to a range of uncertainty that can cover more than one order of magnitude, as can be seen in Figure 2.17.

The upper panel of Figure 2.17 shows the standard particle concentration as used in the NIXE-CAPS analyses (black, e.g. Krämer et al. (2016b); Luebke et al. (2016)), an upper estimation (purple) and a lower estimation (pink). For the particle concentrations, the errors sum up to a total of $\pm 20\%$.

The lower panel shows the total mass of all particles per flight second, derived from particle concentrations and particle sizes. Both parameters are subject to uncertainties. For the mass calculation, the minimum estimation is calculated with the Erfani and Mitchell (2016) parametrization which assumes non-spherical, flat shapes especially for large particles. The maximum estimation works with spheres. The black line shows the setup used in Luebke et al. (2016), in which the Erfani and Mitchell (2016) parametrization is applied only on large particles, whereas small particles are considered to be spherical.

An additional difficulty is the distinction between ice and liquid water: Depending on the phase, the particle density varies, adding another 8% to the uncertainty. Due to these added influences (and because the sizing uncertainty influences the mass calculation to a power of three), the uncertainty range with respect to total masses is significantly higher than the one with respect to concentrations alone, covering up to one order of magnitude.

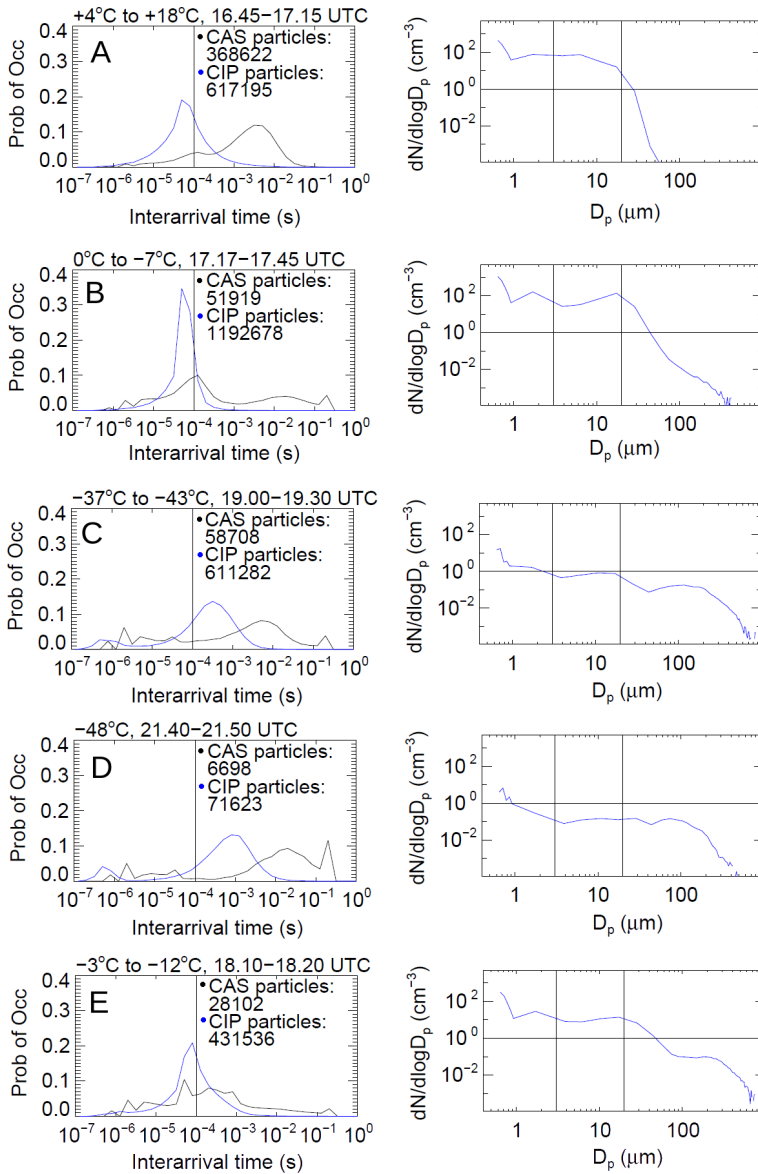


Figure 2.14: Shattering analysis for several cloud sections of flight 18 of the ACRIDICON-CHUVA campaign. Section description: A - warm cloud, B - mixed-phase cloud, C - cumulonimbus anvil, D - cirrus, E - secondary ice cloud (see chapter 3). Left column: Particle interarrival time histograms for CAS (black line) and CIP (blue line); the plot also shows the total number of particles whose IAT was analyzed here. Right column: Average particle size distribution for the chosen section.

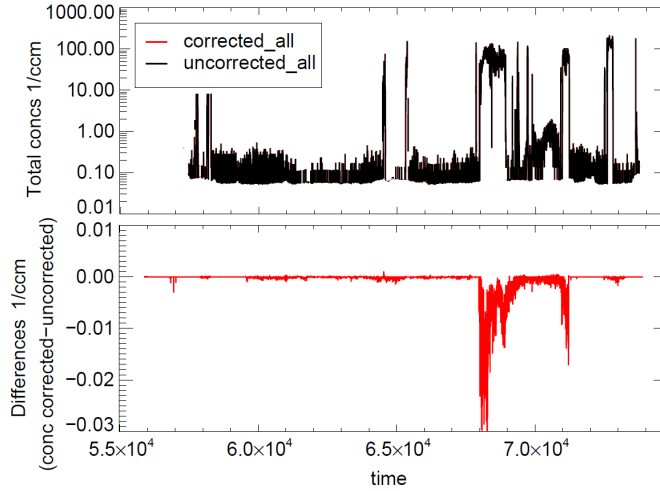


Figure 2.15: Influence of the Poisson spot correction on a cloud measurement with out-of-focus particles (detected manually in the image preview).

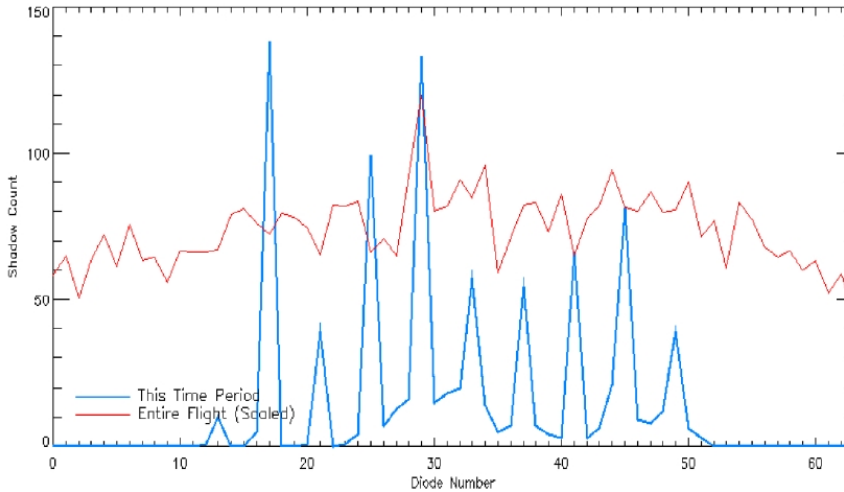


Figure 2.16: At cold temperatures, some diodes of the CIP instruments are sensitive to aircraft vibrations or electric charges (personal communication, A. Afchine). These vibrations cause the instrument to record 'noise' particles. It's always the same set of diodes that are affected. The noise can therefore be filtered out using its regularity.

The blue curve shows shadow counts for all diodes (diode numbers: 1 to 64) in a noise-dominated time buffer. In contrast, the red curve shows the average shadow counts per buffer for all diodes for the entire flight - here, the noisy diodes no longer show an enhanced signal.

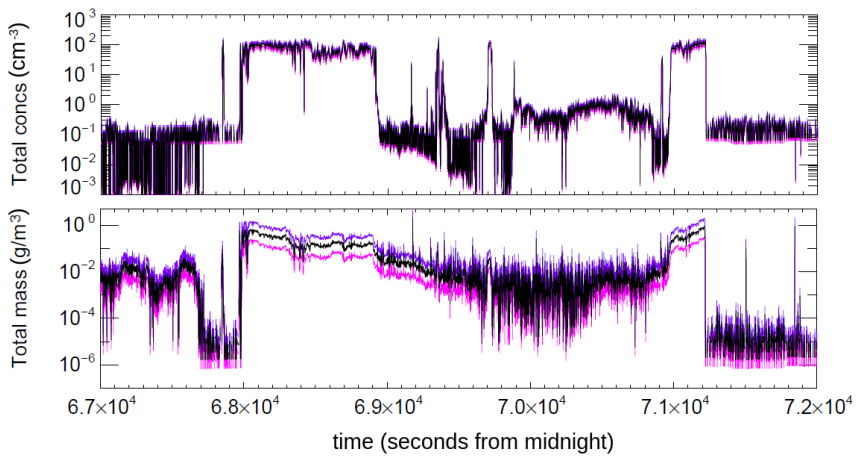


Figure 2.17: Measurement uncertainties can influence two parameters: the obtained particle sizes and particle concentrations. This plot shows the accumulated influence of the NIXE-CAPS measurement uncertainties described by Meyer (2012). Black lines: calculations with standard settings. The pink lines (minimum estimations) and purple lines (maximum estimations) enclose the range of the measurement uncertainty.

3 Classification of mid-level clouds derived from NIXE-CAPS observations¹

3.1 Clouds in the mixed-phase temperature regime

To avoid ambiguities, all clouds observed at temperatures between 0 °C and -38 °C are addressed as 'clouds in the mixed-phase temperature regime' (mpt clouds). In that temperature regime, purely liquid (supercooled) clouds can be found as well as mixed-phase clouds (where liquid water droplets and ice crystals coexist), and also fully glaciated clouds (Pruppacher et al., 1998). Within this temperature range, important processes take place that transform the cloud's phase or microphysical characteristics significantly. This phase transition is not only an important part of precipitation-forming processes like the cold rain process, it also affects the cloud's

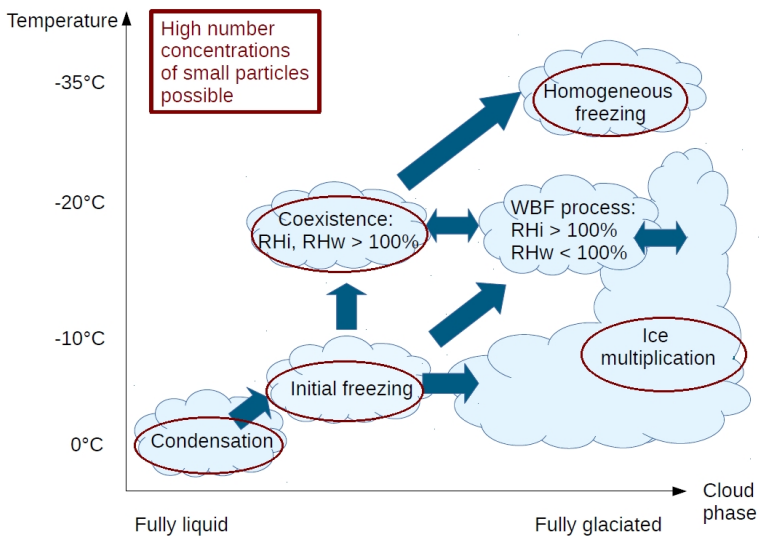


Figure 3.1: Possible paths to glaciation in the mixed-phase temperature regime

¹ The contents of this chapter were published in ACP in October 2017 as research paper 'Classification of Arctic, Mid-Latitude and Tropical Clouds in the Mixed-Phase Temperature Regime' (Costa et al., 2017).

radiative properties by influencing the solar albedo of mpt clouds in the sense that with growing ice fraction, their solar albedo (cooling) effect is reduced (Ehrlich, 2009; Wendisch et al., 2013). Thus a correct representation of this cloud type in global climate models is of importance for an improved certainty of climate predictions (Wendisch et al., 2013).

The transformation from a fully liquid to a fully frozen cloud can follow different, sometimes non-linear paths, as illustrated in Figure 3.1. At first, due to the activation of cloud condensation nuclei, small droplets $< 50 \mu\text{m}$ (all-liquid state) are formed. Initial freezing can occur in those droplets that contain an ice nucleating particle (INP) which can be activated in the ambient cloud environment (resulting in a mixed phase state: coexistence of ice and water). Different INP can induce ice nucleation at different temperatures, depending on their nature, e.g. if they are of biological or mineral origin, their morphology, and freezing efficiency. Therefore, the number of droplets containing an INP to heterogeneously form ice is important for its glaciation, and also the temperature of the mpt cloud is relevant, as the freezing efficiency of different INP varies with temperature. The nature of the INP properties that favor ice formation is one of the major open questions in cloud and climate research. This is summarized in the recent review article by Kanji et al. (2017) and references therein. The conditions that favor drop freezing are simplified: cold temperatures, high relative humidities and a 'good freezing ability'. Biological particles are known to induce ice nucleation in the temperature range between about 0 to -20°C , while mineral dust particles initiate ice at temperatures below about -20°C (Kanji et al., 2017; Augustin-Bauditz et al., 2014).

The persistence of supercooled liquid clouds in case no ice active INP are present is also reported by Korolev (2007a). Moreover, the further development of the glaciation degree of a mpt cloud, where a few ice crystals are present, is discussed in this study with dependence on the environmental dynamical conditions. This is illustrated in Figure 3.2 based on theoretical considerations (Korolev, 2007a) of the partitioning of liquid and ice water content in rising mixed-phase cloud parcels under different conditions. The first scenario represents an intermediate vertical velocity (1 m s^{-1} ; blue lines), where the Wegener-Bergeron-Findeisen process (Findeisen et al., 2015) is triggered above the altitude marked by the blue line (note that the temperature decreases with increasing altitude), which leads to full glaciation of the cloud. At that point, the relative humidity over water falls below 100% ($\text{RH}_w < 100\%$), as more and more water vapour is consumed by the many small liquid cloud droplets. As a result, these droplets evaporate, decreasing the liquid water content. The RH over ice remains above 100% ($\text{RH}_i > 100\%$), allowing the few ice crystals to grow to large sizes $> 50 \mu\text{m}$, thus increasing the ice water content. In contrast, the red graphs show a scenario for higher vertical velocities (2 m s^{-1}). In this case, the updraft preserves the supersaturation over both water and ice ($\text{RH}_w, \text{RH}_i > 100\%$) over the complete altitude range. Subsequently, the liquid and ice water content increase in coexistence and the cloud continues to be only partly glaciated ('coexistence cloud'). These simulations demonstrate that vertical velocity is a major parameter controlling the occurrence of different cloud types, because the updraft is the crucial parameter for possible supersaturations. The

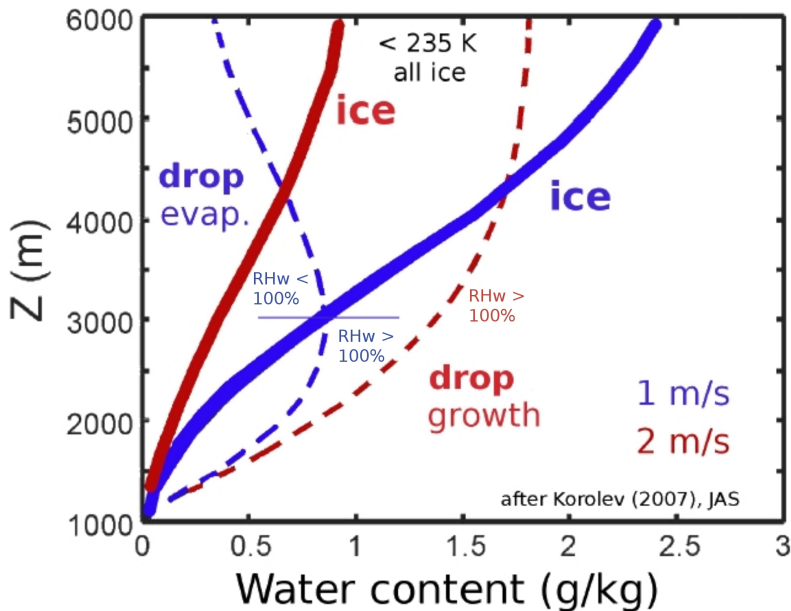


Figure 3.2: Liquid water content (dashed lines) and ice water content (solid lines) development with altitude ($\sim 1/\text{temperature}$) in mixed-phase clouds for different vertical velocities (adapted from Korolev, 2007a, with modification). Blue lines (updraft 1 m s^{-1}): the cloud glaciates when RH_w falls below 100% (WBF = Wegener-Bergeron-Findeisen regime); red lines (updraft 2 m s^{-1}): RH_w stays above 100%, liquid droplets and ice crystals coexist (Coexistence regime).

supersaturation over water can remain at or above 100% only in high updrafts, thus allowing coexistence clouds to survive down to about -38°C , where the supercooled liquid cloud droplets will freeze homogeneously (Pruppacher et al., 1998; Koop et al., 2000). Also, secondary ice production can take place producing high number concentrations of small ice particles (see overview in Field et al., 2015). Known processes are e.g. the Hallett-Mossop process (Hallett and Mossop, 1974) and ice-ice collisions (Yano and Phillips, 2011). When one of these processes has started, the remaining liquid fraction of a cloud can glaciates quickly via contact freezing. Evaporation of both numerous small liquid droplets and large ice particles occurs when the environment is subsaturated with respect to both water and ice ($\text{RH}_i < 100\%$, $\text{RH}_w < 100\%$), as predicted by Korolev (2007a) for downdraft regions within the cloud. If this state persists sufficiently long, the cloud will fully evaporate.

As illustrated in Figure 3.1 and summarized in Table 3.1, four types of mpt clouds are expected to occur: The first type describes purely liquid clouds with many small (diameter $< 50 \mu\text{m}$) liquid droplets that appear often at slightly supercooled conditions and with lesser frequencies as the temperature becomes colder (Bühl et al., 2013). This cloud type may additionally contain a

low concentration of large particles (large droplets from coalescence or ice particles sedimenting from above). The second cloud type are coexistence clouds with a high concentration of small cloud particles $< 50 \mu\text{m}$ that can be liquid or frozen. The coexistence cloud type appears at decreasing temperatures in higher updrafts. In case the updrafts are very strong as in tropical convective clouds, the supercooled liquid cloud droplets can reach cold temperature regions around -38°C and freeze homogeneously. Furthermore a third type with a high concentration of small ice particles (diameter $< 50 \mu\text{m}$) might emerge as a result of secondary ice production e.g. due to the Hallett-Mossop process at temperatures between 3°C and 8°C or ice splintering. As fourth cloud type in case of lower updrafts, fully glaciated Wegener-Bergeron-Findeisen (WBF) clouds containing only very few or no small liquid droplets ($< 50 \mu\text{m}$), but consisting mostly of large ice crystals, are expected to appear with increasing frequency when the temperature decreases.

Due to the manifold interactions between large-scale and small-scale dynamics, aerosol/INP availability, and complex processes of formation and evolution of supercooled liquid and frozen cloud particles, mpt clouds are not well understood and therefore poorly represented in global climate models (Boucher et al., 2013). As a consequence, the uncertainties concerning the global mpt cloud cover's radiative impact are large. Of particular interest is the partitioning of ice and liquid water, i.e. the glaciation degree. An important step to improve the incomplete understanding of the phase transition processes are reliable observations of the different types of mpt clouds. However, cloud particle phase observations are limited by technical constraints: passive satellite data mostly provide information on cloud tops, ground-based lidars can not quantify thick layers of liquid water (Shupe et al., 2008; Storelvmo and Tan, 2015). Active sensors have been used to derive liquid and ice water paths for the full depth of the atmosphere (reported in Boucher et al., 2013, p.580), but are subject to large errors. In situ measurements may cover the full vertical extent (Taylor et al., 2016; Lloyd et al., 2015; Klingebiel et al., 2015), but are restricted to the flightpath and have to be analysed carefully (Wendisch and Brenguier, 2013). Also, the phase identification often depends on cloud particle sizes. Small cloud particles $< 50 \mu\text{m}$ are usually regarded as liquid (see e.g. Taylor et al., 2016). With particle imaging probes like OAPs (Optical Array Probes), more sophisticated shape recognition algorithms can be used (e.g. Korolev and Sussman, 2000), which are nevertheless limited: Usually, they require a minimum number of pixels (corresponding to cloud particles with diameters of $70 \mu\text{m}$ and more) to recognize round or aspherical particles reliably.

In the study presented here, in situ airborne cloud measurements in the cloud particle size range from $3 \mu\text{m}$ to $937 \mu\text{m}$ are used to classify the above described types of clouds in the mpt regime (see Table 3.1): 'Mostly liquid' clouds after drop formation, 'coexistence clouds' after initial freezing, 'secondary ice' clouds influenced by ice multiplication, and clouds after the WBF process. This classification allows to revisit a statistical overview published by Pruppacher et al. (1998), stating at which temperatures purely liquid or ice-containing clouds were found.

For all except the fourth cloud type, high cloud particle number concentrations are expected,

	Cloud particle concentration	Particles Dp < 50 μm	Particles Dp > 50 μm	Dominant mass mode
"Mostly liquid"	high	Liquid	Drizzle drops/few ice crystals possible	Dp < 50 μm
"Coexistence"	high	Mostly liquid, some ice crystals	Glaciated	Dp < 50 μm
"Secondary ice"	high	Glaciated	Glaciated	Dp < 50 μm
"Large ice/ WBF"	low	Glaciated	Glaciated	Dp > 50 μm

Table 3.1: Characteristics of the cloud types expected in the mpt regime.

with a peak at cloud particle sizes < 50 μm . Thus, particle size distributions and concentrations allow the differentiation between glaciated clouds mainly formed via the WBF process and other cloud types in the mpt regime. To identify these other types more closely, the NIXE-CAS detector is used which can quantify the aspherical fractions of the small (< 50 μm) cloud particles (see chapter 2 and Baumgardner et al., 2014) together with a visual shape inspection of particles > 50 μm . The occurrence of the four cloud types is quantified with regard to measurement location and temperature by performing a statistical analysis of the 1 Hz data.

The chapter is structured as follows: In section 3.2, the field campaigns are described. In section 3.3, the observations are evaluated with respect to the clouds' size distribution, the correlation of cloud particle concentrations and expected ice nucleating particle concentrations, the cloud particle asphericity and the associated vertical velocities. Section 3.4 summarizes the findings of this study.

3.2 Field campaigns

The measurements used for this study were conducted during four field campaigns (see Figure 3.3) which are briefly described in the following. In total, the dataset in the mixed-phase temperature regime between 0°C and -38°C covers 38.6 hours within clouds in Arctic, mid-latitude and tropical regions. The data were obtained with the cloud spectrometer NIXE-CAPS. The NIXE-CAPS instrument and the data analysis are described in chapter 2.

The first campaign, COALESC (Combined Observation of the Atmospheric boundary Layer to study the Evolution of StratoCumulus), was based in Exeter, UK, in February and March 2011. The NIXE-CAPS was installed as a wing probe on the BAe146 aircraft operated by the Facility for Airborne Atmospheric Measurements (FAAM), UK. All flights took place in the coastal area of south-east England and Wales; the main campaign target were low stratus and stratocumulus clouds. The campaign is described in Osborne et al. (2014). Table 3.2 provides an overview of the flights. Out of 16 measurement flights, 14 provided observations of mpt clouds, with in total 41042 seconds (11.4 hours) of data.

Measurements in Arctic clouds have been conducted during the campaigns VERDI (April and May 2012, Study on the VERTical Distribution of Ice in Arctic clouds, see also Klingebiel

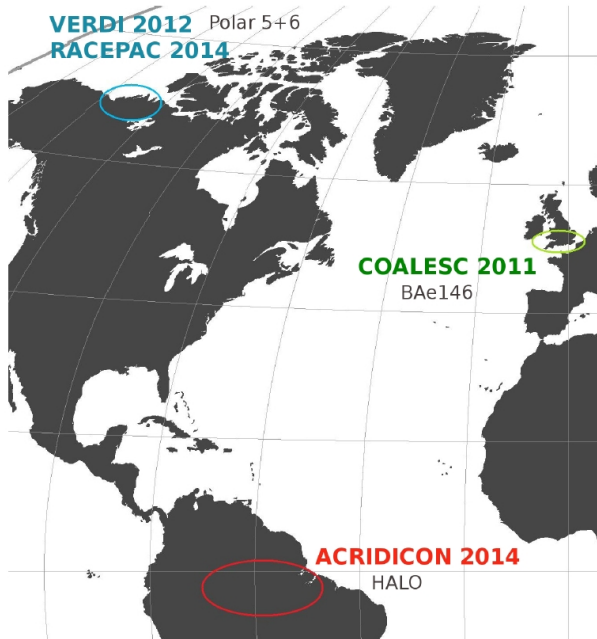


Figure 3.3: Locations of the campaigns comprised in this study.

et al., 2015) and RACEPAC (April and May 2014, Radiation-Aerosol-Cloud ExPeriment in the Arctic Circle). Both campaigns took place in Inuvik, Northern Canada. Research flights were performed with the Polar-5 and Polar-6 aircraft of the Alfred-Wegener-Institut, Germany. The 13 flights of both VERDI (see Table 3.3) and RACEPAC (Table 3.4) covered the region of the Arctic Beaufort Sea coast with its retreating sea ice in spring. VERDI yielded 59028 seconds (16.4 hours) of observations within mpt clouds, RACEPAC contributed 33354 seconds (9.3 hours). Although both campaigns took place at the same time of the year, different synoptic situations lead to different cloud characteristics: VERDI was dominated by stable anticyclonic periods with weak gradients of atmospheric parameters that allow to form a strong inversion in the boundary layer associated with persisting stratus, whereas during RACEPAC frontal systems frequently passed the area of the observations and initiated a more variable and short living cloud situation.

The tropical measurement campaign ACRIDICON-CHUVA (Aerosol, Cloud, Precipitation, and Radiation Interactions and Dynamics of Convective Cloud Systems/Cloud processes of tHe main precipitation systems in Brazil: A contribUtion to cloud resolVing modelling and to the GPM (Global Precipitation Measurements)) was carried out in September and October 2014. The instrument platform was HALO (High Altitude and Long Range Research Aircraft), a Gulfstream V aircraft operated by DLR (Deutsches Luft- und Raumfahrtszentrum/German

Aerospace Centre). Based in Manaus, Brazil, ACRIDICON-CHUVA was aimed at convective clouds over tropical rainforest and deforested areas (cf. Table 3.5; for details, see Wendisch et al., 2016). The campaign comprises 14 flights, 11 of which contained clouds in the mixed-phase temperature regime. Although cloud profiling at various altitudes and temperatures was a main directive of ACRIDICON-CHUVA, the total time spent within mpt clouds was only 5368 seconds (1.5 hours). The relatively limited time span was caused by the high flying speed of HALO (up to 240 m s^{-1}); it results in short penetration times (in the range of several seconds) of the convective towers. A second reason is the increasing danger of strong vertical winds and icing in developing cumulonimbus clouds. From certain cloud development stages on, only the cloud's anvil and outflow at cold temperatures lower than -38°C could be probed.

Date	Probed clouds - flight objectives	Cloud T in the mpt regime	Minutes in mpt clouds
15.02.2011	Warm clouds, mixed clouds, cirrus; test flight	-1.5°C to -37.6°C	85.1
23.02.2011	Warm clouds, cirrus clouds	0°C to -37.8°C	11.7
24.02.2011	Warm Stratocumulus	0°C to -0.1°C	0.1
26.02.2011	Stratocumulus in mixed-phase T regime	0°C to -17.9°C	46.0
01.03.2011	Stratocumulus in mixed-phase T regime	0°C to -6.4°C	124.7
02.03.2011	Stratocumulus	0°C to -3.1°C	92.0
03.03.2011	Stratocumulus	0°C to -4.4°C	61.9
05.03.2011	Stratocumulus	0°C to -3.3°C	51.4
07.03.2011	No clouds	–	0
08.03.2011	Warm stratocumulus and cirrus clouds	0°C to -38.0°C	47.0
11.03.2011	Stratocumulus	0°C to -4.9°C	105.9
14.03.2011	Mostly cirrus clouds	-8.9°C to -37.9°C	10.6
15.03.2011	Stratocumulus and cirrus	0°C to -38.0°C	25.8
16.03.2011	Stratocumulus	0°C to -0.3°C	6.7
18.03.2011	No clouds	–	0
19.03.2011	Mostly contrail cirrus	-18.1°C to -38.0°C	11.9

Table 3.2: Flight table for COALESC

Date	Probed clouds - flight objectives	Cloud T in the mpt regime	Minutes in mpt clouds
25.04.2012	Low mostly liquid stratus, test flight	-3.7 °C to -9.1 °C	47.1
27.04.2012	Stratus (liquid and ice) over sea ice	-8.1 °C to -16.5 °C	73.4
27.04.2012	Low dissipating clouds over sea ice	-9.1 °C to -17.3 °C	47.6
29.04.2012	Stable stratus over sea ice	-8.4 °C to -12.5 °C	77.9
30.04.2012	Extensive cloud with layer structure	-6.3 °C to -19.1 °C	212.8
03.05.2012	Thin low subvisible clouds	-9.4 °C to -12.1 °C	56.15
05.05.2012	Patchy low cloud layer at mpt regime	-8.6 °C to -16.8 °C	77.9
08.05.2012	Mostly supercooled liquid clouds, two layers	-4.9 °C to -9.7 °C	65.8
10.05.2012	Dissolving altostratus layer	-5.5 °C to -11.2 °C	45.1
14.05.2012	Two thin stratus and cumulus	-1.4 °C to -5.8 °C	41.9
15.05.2012	Mostly liquid stratus and a cumulus	-0.7 °C to -14.1 °C	73.2
16.05.2012	Thin, mostly liquid stratus	-1.7 °C to -5.3 °C	95.2
17.05.2012	Mostly liquid stratus with large snow	0 °C to -6.3 °C	54.5

Table 3.3: Flight table for VERDI

Date	Probed clouds - flight objectives	T range/cloud top T	Minutes in mpt clouds
28.04.2014	Cumulus	-12.9 °C to -17.8 °C	54.1
30.04.2014	Low level clouds in cold sector of a low	-2.3 °C to -14.4 °C	70.2
01.05.2014	Thin fog layer	-2.0 °C to -9.6 °C	5.0
03.05.2014	Single/double layer liquid dominated cloud	0 °C to -2.4 °C	27.2
06.05.2014	Single/multilayer clouds	0 °C to -6.3 °C	55.6
08.05.2014	Thick stratus	0 °C to -3.8 °C	22.5
10.05.2014	Two stratus clouds	-3.0 °C to -9.1 °C	49.0
11.05.2014	No clouds	–	0
13.05.2014	No clouds	–	0
14.05.2014	Homogeneous stratus	-1.9 °C to -10.1 °C	25.8
16.05.2014	Midlevel clouds	0 °C to -10.1 °C	75.7
17.05.2014	Liquid and ice clouds on various altitudes	0 °C to -11.3 °C	22.7
20.05.2014	Low-level clouds	-1.5 °C to -9.5 °C	54.2
22.05.2014	Low-level clouds before front	-6.1 °C to -15.0 °C	29.2
22.05.2014	Stratus behind front	-1.5 °C to -11.8 °C	29.6
23.05.2014	Midlevel clouds	-2.3 °C to -15.1 °C	14.3

Table 3.4: Flight table for RACEPAC

Date	Probed clouds - flight objectives	Cloud T in the mpt regime	Minutes in mp clouds
06.09.2014	Convective cloud profiling and outflow	0 °C to -32.2 °C	13.2
09.09.2014	Convective cloud profiling	0 °C to -1.2 °C	1.1
11.09.2014	Convective cloud profiling and outflow	0 °C to -38.0 °C	8.6
12.09.2014	Cloud tops for satellite comparison	0 °C to -29.6 °C	5.5
16.09.2014	Pyrocumulus profiling and outflow	0 °C to -38.0 °C	18.1
18.09.2014	Shallow convective cloud profiling and outflow	-36.6 °C to -38.0 °C	1.4
19.09.2014	Pyrocumulus profiling, convective outflow	-0.4 °C to -35.1 °C	8.8
21.09.2014	Albedo flight	–	0
23.09.2014	Convective cloud profiling and outflow	0 °C to -38.0 °C	5.5
25.09.2014	Cb anvil/outflow	-29.4 °C to -38.0 °C	13.5
27.09.2014	Warm clouds over forested and deforested areas	–	0
28.09.2014	Convective cloud profiling	0 °C to -38.0 °C	11.1
30.09.2014	Albedo flight	–	0
01.10.2014	Convective cloud profiling and outflow	0 °C to -5.6 °C	2.6

Table 3.5: Flight table for ACRIDICON

3.3 Results and Discussion

3.3.1 Mpt cloud classification based on particle number size distributions

Four cloud types are expected in the mpt regime (see Table 3.1). As mentioned in the introduction, however, only two typical particle number size distributions (PSD) are found frequently in mpt clouds (Type 1 and Type 2). Figure 3.4 shows NIXE-CAPS PSDs measured during VERDI flight 08, where both types alternate: Some cloud regions show very high particle concentrations of small particles with a mode diameter $< 50 \mu\text{m}$ (see example PSD in the lower right corner). Alternatively, the clouds consist mostly of large ice crystals $> 50 \mu\text{m}$ with either no small particles or concentrations below the NIXE-CAS detection limit (see example PSD in the lower left corner).

As a first step of the mpt cloud classification, all clouds are sorted according to their particle size distribution type; the types can then be addressed separately. To this end, two cloud particle number concentrations are calculated, one for particles with diameters between $3 \mu\text{m}$ and $50 \mu\text{m}$ (N_{small}) and one for all larger particles (N_{large}). For the classification of the first cloud type (Type 1), N_{small} must exceed 1 cm^{-3} , while N_{large} can be zero or larger. The mode of the cloud

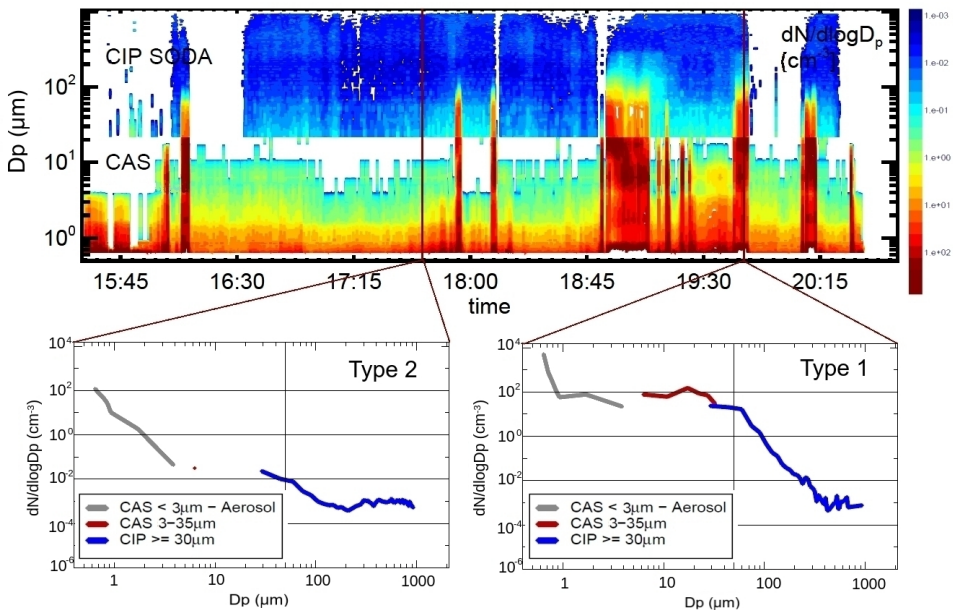


Figure 3.4: Size distributions along time during flight 08 of the VERDI campaign. Two types of clouds can be distinguished; one is dominated by the large particle mode (Type 2, example in lower left panel), the second by small particles (Type 1, example in lower right panel). The two cloud types are also associated with strongly differing particle number concentration ranges, cf. Figure 3.5.

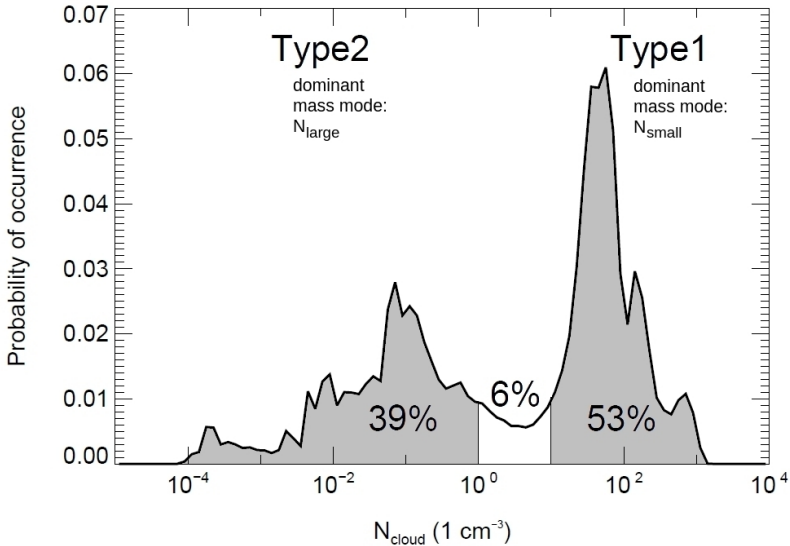


Figure 3.5: Histogram of cloud particle concentrations (D_p $3 \mu\text{m}$ to $937 \mu\text{m}$) of Type 1 and Type 2 clouds in the mixed-phase temperature regime between 0°C and -38°C . For cloud type definitions see subsection 3.3.1. The 6% between the two clear modes were classified as 'Type 1' in this study. N_{small} : Particles with diameters between $3 \mu\text{m}$ and $50 \mu\text{m}$. N_{large} : Particles with diameters $> 50 \mu\text{m}$. N_{cloud} : All particles with diameters of $3 \mu\text{m}$ and larger.

particle mass distribution is at particle diameters $< 50 \mu\text{m}$. This type matches the young clouds after droplet condensational growth in Figure 3.1.

In the second cloud type (Type 2) those clouds are compiled with N_{small} below 1 cm^{-3} and N_{large} present. The mode of the cloud particle mass distribution is here at particle diameters $> 100 \mu\text{m}$. This type matches fully glaciated clouds, e.g. as a result of the WBF process (see Figure 3.1).

In Figure 3.5, a histogram is provided that shows the occurrence of cloud particle concentrations throughout our dataset. The spectrum of observed concentrations is continuous, but the two modes associated with the Type 1 and Type 2 clouds (as described above) are clearly visible. The area between the two modes (a total of 6% of all observations) might result from clouds in a 'transition' state to glaciation. In this study, these measurements were assigned to Type 1 clouds. The smallest mode with a peak at around 10^{-4} cm^{-3} shows concentrations around the detection limit of the CIP (a total of 5% of all observations). These might be measurements in precipitation, especially in snow that occurred frequently in the Arctic campaigns, and in sedimenting aggregates of ice crystals from tropical convective clouds (see subsection 3.3.3).

In the following, the cloud types described above are discussed in more detail. Type 1 cloud characteristics measured during VERDI are shown in Figure 3.6. These clouds have a clear mode between $3 \mu\text{m}$ and $50 \mu\text{m}$ and are very dense, cloud particle number concentrations reach

Type1	$N_{\text{small}} (\text{cm}^{-3})$	$N_{\text{large}} (\text{cm}^{-3})$
235 K	2.207	0.162
240 K	2.632	0.177
245 K	19.894	0.134
250 K	24.902	0.166
255 K	109.944	0.035
260 K	109.798	0.022
265 K	269.979	0.032
270 K	166.362	0.047
275 K	67.788	0.098

Type2	$N_{\text{small}} (\text{cm}^{-3})$	$N_{\text{large}} (\text{cm}^{-3})$
235 K	0.057	0.023
240 K	0.080	0.025
245 K	0.069	0.017
250 K	0.062	0.010
255 K	0.064	0.004
260 K	0.140	0.003
265 K	0.070	0.003
270 K	0.116	0.005
275 K	0.117	0.017

Table 3.6: Average cloud particle concentrations for the two cloud types defined in subsection 3.3.1 (see also Figure 3.4), for both small ($D_p < 50 \mu\text{m}$) and large ($D_p > 50 \mu\text{m}$) cloud particles.

average values of dozens to more than two hundred cm^{-3} . Table 3.6 shows average cloud particle concentrations for the Type 1 clouds in 5 K intervals. Low number concentrations of large ice particles $> 50 \mu\text{m}$ are sometimes found, but all clouds of this type are dominated by N_{small} , which may consist of liquid droplets, frozen droplets, or small ice from ice multiplication processes. With regard to the concentrations of N_{small} in the different temperature intervals (Figure 3.6 and Table 3.6), it can be clearly seen that they decrease with decreasing temperature. When a cloud consists of liquid droplets, they grow by condensation when lifted to higher altitudes - and thus colder temperatures - followed by an increasing coalescence of the droplets, which consequently causes a higher number of N_{large} while depleting the concentration of small droplets. This is also visible in Figure 3.6. Note, however, that N_{large} also decreases with increasing temperature, reaches a minimum around 260 K, and then rises again, possibly reflecting the increasing occurrence of sedimenting particles. Visual inspection of the CIP images indicates that in the N_{large} cloud mode ice crystals can be found in addition to the drizzle drops. Three of the cloud types of the mpt regime are expected to show Type 1 cloud characteristics: 'Liquid', 'coexistence' and 'secondary ice' clouds.

The second set of PSDs (Type 2: Figure 3.7) is not strongly dominated by N_{small} . Here, N_{large} form a distinct mode. Both mode concentration and maximum values decrease with decreasing temperatures. Clouds of this PSD type have low number concentrations of - on average - less than 0.1cm^{-3} in the size range 3 to $50 \mu\text{m}$ (see Table 3.6). For the sizes $> 50 \mu\text{m}$, the CIP images show ice crystals or aggregates. This is the typical appearance of a fully glaciated

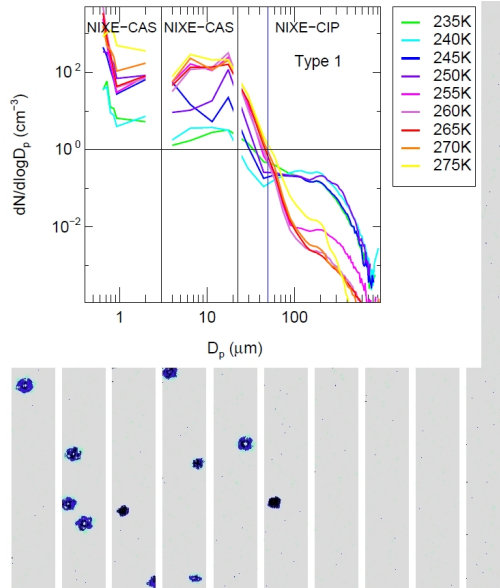


Figure 3.6: Type 1 clouds: Example of CIP images and average particle size distributions (PSDs) in 5 K intervals, all campaigns. The thin vertical line at $3 \mu\text{m}$ marks the boundary between aerosol and cloud particles. The line at $20 \mu\text{m}$ marks the transition from the NIXE-CAS-DPOL to the NIXE-CIPg instrument. The thick blue line divides the cloud particle population in particles smaller and larger than $50 \mu\text{m}$.

cloud, formed either via the WBF process during which the small liquid droplets evaporate or, at lower altitudes (higher temperatures), due to sedimentation, when aggregates precipitate from higher levels. Again, the two temperature groups are seen as for the Type 1 clouds (Figure 3.6). An explanation can be that Type 2 clouds most probably develop from Type 1: once the environment becomes subsaturated ($\text{RH}_w < 100\%$, $\text{RH}_i > 100\%$), all liquid droplets evaporate leaving only the ice crystals that have already formed from droplets that contain an INP. Therefore, N_{large} of Type 2 is only a fraction of those of Type 1, which might reflect the number of active INP in the respective temperature interval in case no ice multiplication takes place (see subsection 3.3.2). Thus, the larger differences between the two temperature groups - as seen for Type 1 clouds - more or less balance out. Indeed, an increase of average ice crystal numbers can be seen (Table 3.6, bottom, N_{large}), which might be interpreted as increasing fraction of activated INP with decreasing temperature. Note that N_{small} is still larger than N_{large} . Since shattering artefacts are unlikely (cf. subsection 2.5.2), this means that in Type 2 clouds, too, a significant number of small particles persists over the whole temperature range.

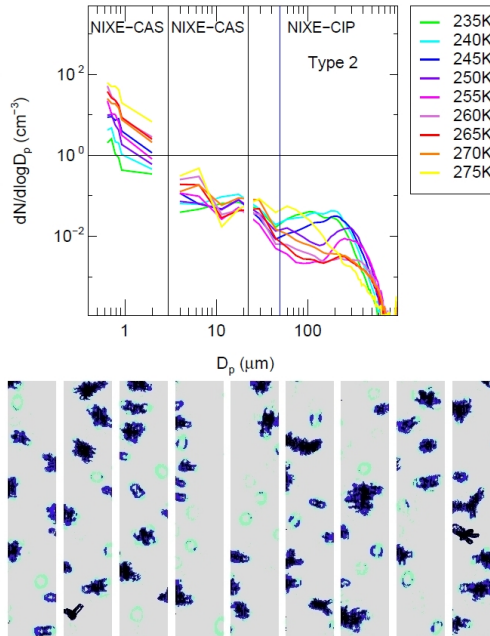


Figure 3.7: Same as in Figure 3.6, but for Type 2 clouds.

3.3.2 Comparison of cloud particle with with ice nuclei numbers

A comparison of the measured cloud particle number concentrations to INP concentrations (N_{INP}) can give an indication if the ice particles may result from primary ice nucleation. No direct INP measurements are available for this study, so N_{INP} is estimated using the formula provided by DeMott et al. (2010), where aerosol numbers of particles between $0.5 \mu\text{m}$ and $3 \mu\text{m}$ are related to INP concentrations. NIXE-CAPS records particles larger than $0.6 \mu\text{m}$; the fraction from $0.6 \mu\text{m}$ to $3 \mu\text{m}$ is used as 'aerosol fraction'. The results for N_{INP} are shown in Figure 3.8 as a function of temperature. Generally, N_{INP} increases with decreasing temperature, as already mentioned in the last section. The most frequent N_{INP} range between the lowest calculated value of 10^{-4}cm^{-3} (0.1L^{-1}) and $\sim 10^{-3} \text{cm}^{-3}$ (1L^{-1}), while the maximum reaches up to 0.3cm^{-3} ($\sim 300 \text{L}^{-1}$). In comparison to a compilation of INP measurements presented recently by Kanji et al. (2017), the estimated range of INP numbers is shifted to somewhat smaller concentrations.

In Figure 3.9, N_{small} and N_{large} for both Type 1 and Type 2 clouds are now shown in the same way of presentation as before N_{INP} . In Type 1 clouds, especially for N_{small} (upper left panel), concentrations range between 2cm^{-3} and more than 200cm^{-3} down to temperatures of -20°C , well exceeding all INP estimations in this temperature range. But also for N_{large} (upper

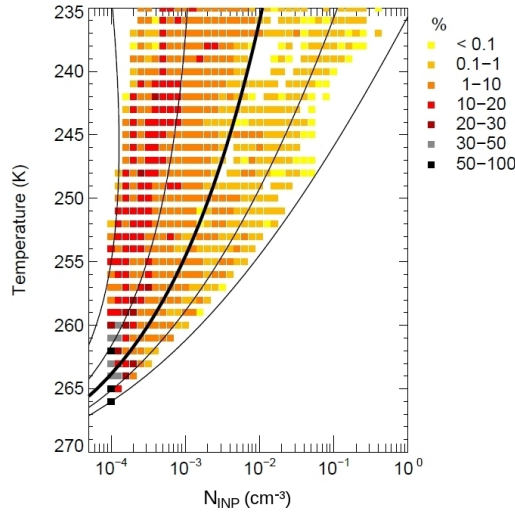


Figure 3.8: Frequencies of ice nucleating particle number concentrations (N_{INP}) vs. temperature for all measurement campaigns, estimated from NIXE-CAPS measurements of aerosol concentrations (D_p 0.6 - 3 μm) following DeMott et al. (2010). The black lines indicate INP concentrations for constant aerosol concentrations of 0.01 scm^{-3} (leftmost line), 0.1 scm^{-3} , 1 scm^{-3} (thick line), 10 scm^{-3} and 100 scm^{-3} (rightmost line).

right panel), the cloud particle concentrations exceed the expected N_{INP} by several orders of magnitude. For colder temperatures, where the measured cloud particle number concentrations are lower, the estimated N_{INP} are also mostly lower than the cloud particle concentrations. In general, primary ice nucleation can be excluded as origin for cloud particles in the Type 1 clouds.

The N_{large} of Type 2 clouds (lower right panel) agree quite well with N_{INP} for a wide range of temperatures. However, in warm areas, the cloud particle concentrations can be higher - they might represent large ice crystals sedimenting from upper layers, as mentioned in Section 3.1. For the colder regions, the agreement is consistent with the assumption that the Type 2 clouds we observed were formed by the WBF process (see subsection 3.3.1) and that the initial ice crystals have likely formed around INP. N_{small} is slightly increased in comparison with N_{INP} . Again, it is possible that this is an effect of the CAS' limited detectable concentration range, as discussed in chapter 2.

3.3.3 Mpt cloud classification based on sphericity

Size distributions, cloud particle number concentrations and comparisons with expected INP number concentrations provide little information on the cloud particle phase (cf. subsection 3.3.1, subsection 3.3.2). For further insights on the nature of the observed clouds, information on

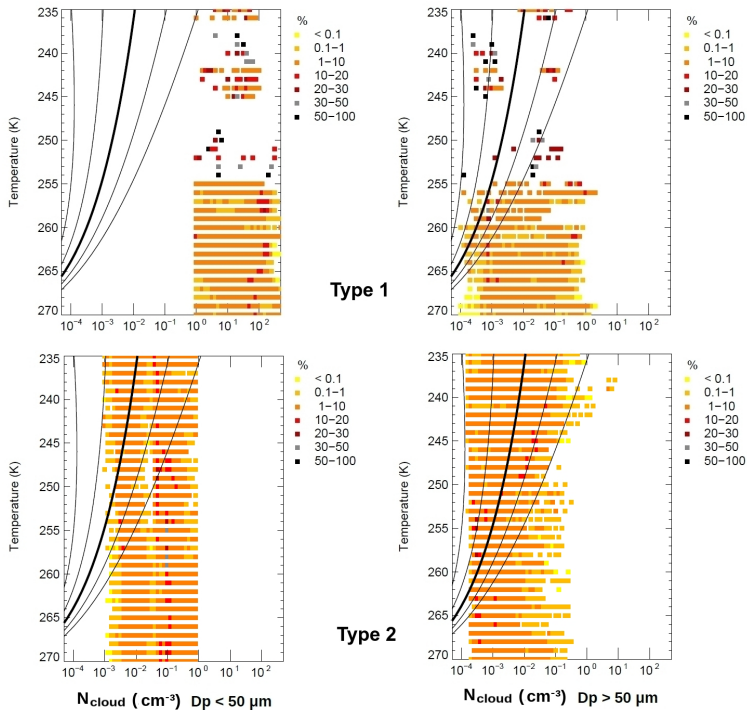


Figure 3.9: Same as Figure 3.8, but frequencies of cloud particle number concentrations for N_{small} (left panel) and N_{large} (right panel). Top row: Type 1 clouds, bottom row: Type 2 clouds.

cloud particle asphericity is used, as described in chapter 2: For this, an asphericity analysis is performed for particle sizes between $20 \mu\text{m}$ and $50 \mu\text{m}$, the range with the strongest particle asphericity signal. For this size range, 'aspherical fractions' (AF) are derived: the percentage of aspherical particles per second, which means that particle bulk properties are analyzed, not single particle signatures alone. This approach does not require an interpretation of each aspherical fraction measurement alone, but divide the AFs into three groups: (i) AF = 0% (zero), (ii) AF: 0 - 50% (low) and (iii) AF = 50 - 100% (high).

Figure 3.10 shows the aspherical fractions of Type 1 and 2 cloud particles vs. temperature, the data points are color coded by the respective field campaigns. The horizontal lines show the 0°C (liquid) and -38°C (ice) temperature thresholds. Looking at the data points in pure ice clouds below -38°C it can be seen that most of the measurements are found in group (iii) 'high AF' range. These AF can therefore be associated with fully glaciated clouds. Note that Type 2 clouds show AF comparable to those of cirrus clouds. The small particles found in relatively large number concentrations in this cloud type (see subsection 3.3.1 and Table 3.6) must therefore be small ice crystals.

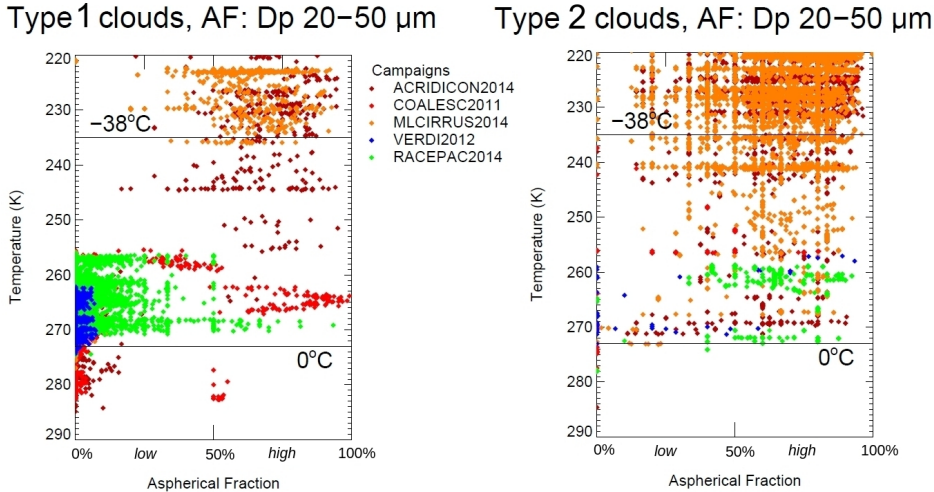


Figure 3.10: Aspherical fractions (AF) for $D_p = 20$ to $50 \mu\text{m}$. Type 1 clouds show a variety of AF. Type 2 shows AFs comparable to cirrus clouds - which is illustrated by observations from the ML-Cirrus campaign (see chapter 4) - throughout the temperature range.

Due to the ambiguities of the polarization measurement discussed in Section 2.2.1, AF covers a broad range, most often between 70%-80%. Note that even in the cirrus clouds the AF never reaches 100%. A possible reason for this deviation can be columnar ice crystals: these are not well recognized by the CAS sensor (see Järvinen et al., 2016). Alternatively, frozen droplets might have maintained their compact, quasi-spherical shape. All aspherical fractions derived from CAS measurements must therefore be seen as 'minimum aspherical fractions'.

AF found in group (i) - 'zero AF' - are classified as liquid, while AF observations in group (ii) - 'low AF' - are regarded as mixed-phase clouds (liquid + ice). Group (iii) - high AF - is most likely fully frozen. Particles $> 100 \mu\text{m}$ are mostly irregular (i.e. ice) in group (ii) and (iii). In group (i), large ice particles can occasionally be found. In the size range between $50 \mu\text{m}$ and $100 \mu\text{m}$, the distinction between drizzle drops and ice particles is not possible, because the shadow images do not contain enough pixels to differentiate between spherical and irregular particles (see chapter 2).

3.3.4 Cloud type detection in the mpt regime

The different cloud types that can be expected in the mpt regime (Table 3.1) can be identified by the combination of information about N_{small} , N_{large} , and the respective aspherical fractions (AF) in each size range. Following this line, the following sorting criteria are used to classify the mpt clouds - second by second - into the four cloud types:

1. 'Mostly liquid' Type 1 clouds are classified where N_{small} is $> 1 \text{ cm}^{-3}$ and AF is zero (liquid).
2. 'Coexistence' Type 1 clouds are classified where N_{small} is $> 1 \text{ cm}^{-3}$ and AF is low ($< 50\%$, liquid and ice) and large ice crystals N_{large} are present.
3. 'Secondary ice' Type 1 clouds are classified where N_{small} is $> 1 \text{ cm}^{-3}$, AF is high (ice) and large ice crystals N_{large} are present.
4. 'WBF/Large ice' Type 2 clouds are classified where N_{small} is $< 1 \text{ cm}^{-3}$, AF is high ($> 50\%$, ice) and large ice crystals N_{large} are present.

3.3.5 Mpt cloud classification: Results

The mpt clouds observed in this study were probed under a wide range of meteorological conditions (see section 3.2). Thus, these clouds have formed and evolved in different environments with regard to INP properties and updrafts, which are shown in the previous section to be the major parameters influencing the mpt cloud glaciation process.

For a comprehensive interpretation of the observed clouds, the clouds are divided into Arctic, mid-latitude, and tropical clouds. The vertical velocities from the aircraft's meteorological data are analyzed (Figure 3.11), as well as the estimated INP numbers (Figure 3.12). Finally, distributions of the four mpt cloud categories (see Section 3.4) are established as a function of temperature (note that the temperatures are related to different altitudes depending on the geographical region, Figure 3.14). The results are presented in Figure 3.13.

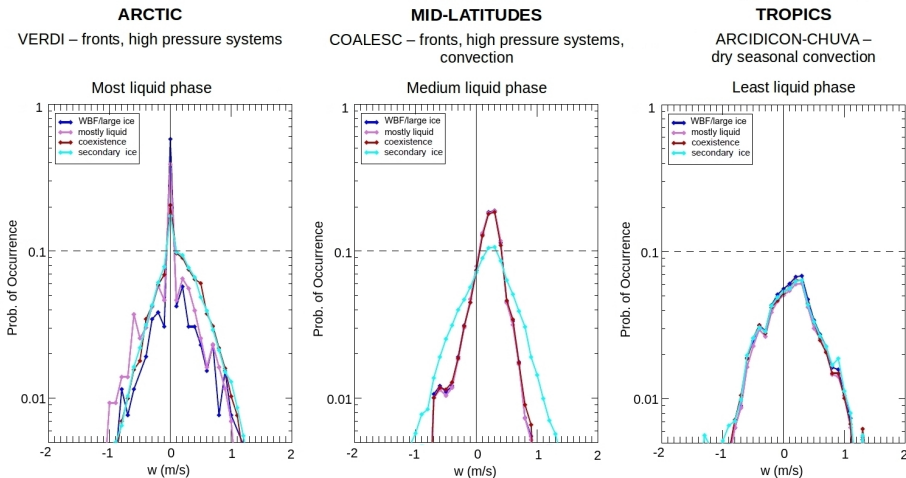


Figure 3.11: Frequency of occurrence for vertical velocities (w) within mpt clouds during the campaigns VERDI (Arctic), COALESC (mid-latitudes) and ACRIDICON-CHUVA (tropics).

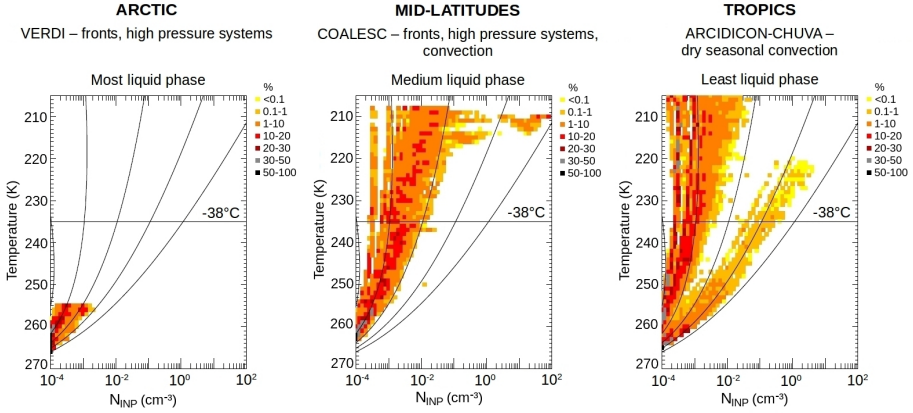


Figure 3.12: Frequencies of occurrence of INP concentrations (N_{INP}) vs. temperature during VERDI and RACEPAC (Arctic), COALESC (mid-latitudes) and ACRIDICON-CHUVA (tropics). INP number concentrations are estimated via aerosol concentrations for particles $> 0.6 \mu\text{m}$ following DeMott et al. (2010). The black lines indicate INP concentrations for constant aerosol concentrations of 0.01 cm^{-3} (leftmost line), 0.1 cm^{-3} , 1 cm^{-3} , 10 cm^{-3} and 100 cm^{-3} (rightmost line).

Arctic clouds

The cloud types found during the field campaigns VERDI and RACEPAC are shown in Figure 3.13 (left panel). For the probed temperature ranges (253 to 273 K - note that the temperature values in the figure indicate midbins), 50 to 80% of the mpt clouds belong to the 'Mostly liquid' (pink) category. Further, a low number of 'Coexistence' clouds (brown) is found, as well as a small percentage of glaciated 'WBF' clouds (dark blue). A possible explanation for the large amount of 'Mostly liquid' clouds could be a lack of biological INP at the time and location of the Arctic measurements as predicted in a model study by Wilson et al. (2015), so those clouds might not freeze at low temperatures (Shupe et al., 2008; Augustin-Bauditz et al., 2014).

The INP estimations for the Arctic (see Figure 3.12, left panel) can not be used to test this hypothesis, because the 'out of cloud' probed altitude range only covers warm temperatures, where the INP estimation is not very sensitive to the measured aerosol concentrations.

However, an inspection of the vertical velocities measured during the Arctic campaigns in Figure 3.11 (left panel) indicates that 60% of the 'mostly liquid' (pink) clouds are found in areas with very low updrafts, fluctuating around zero, while 40% are found in weak updrafts/downdrafts, respectively. Comparably weak updrafts are also frequently found in the 'WBF' (dark blue) clouds. This is to be expected, because the WBF regime develops in weak updrafts, implying that the trigger to transform a cloud from liquid to ice is the available INP concentration. The 'Coexistence' (brown) and 'Secondary ice' clouds were observed with low frequency ($<1\%$)

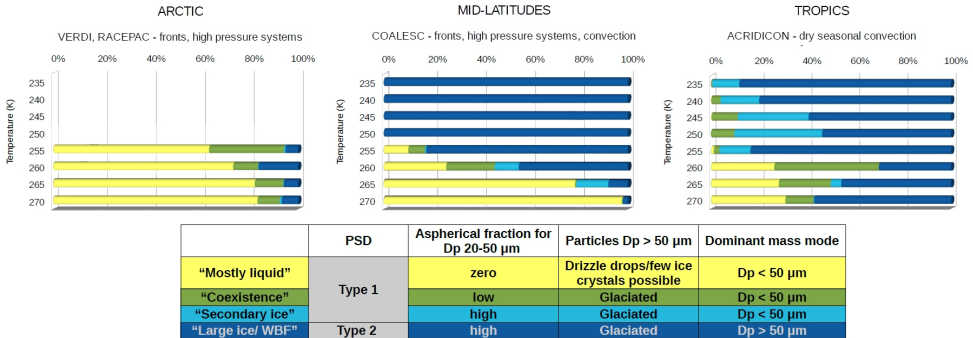


Figure 3.13: Occurrence of the cloud types defined in subsection 3.3.3: "Mostly liquid" clouds are dominated by small, exclusively spherical particles. They have high overall number concentrations. "Coexistence" clouds are dense, too, but do contain some small aspherical particles, indicating that a glaciation process has begun. The "secondary ice" cloud type is again very dense - the particle numbers exceed the INP concentration estimations by far (see subsection 3.3.2). Here, most of the small particles in the size range between 20 μm and 50 μm are aspherical; the cloud must therefore consist of ice. In contrast, clouds in the category "WBF/large ice" show low overall number concentrations. These clouds are dominated by large ice particles which may resume from the Wegener-Bergeron-Findeisen process or, especially in the tropics, be large, sedimenting ice aggregates from cumulonimbus anvils.

in the Arctic and show a slightly wider spread in updraft velocities. In particular, higher updrafts occurred more often ($\sim 30\%$) in these clouds, which is consistent with the theoretical considerations shown in Figure 3.2 for the 'Coexistence' regime.

Mid-latitude clouds

At mid-latitudes (COALESC field campaign), the largest cloud fraction are the fully glaciated WBF clouds (dark blue in Figure 3.13, middle panel). This is consistent with the assumption that at mid-latitudes, the WBF process is the dominant process for cloud evolution (Boucher et al., 2013). More INP seem to be available that are ice active at and below -10°C (263K). At temperatures warmer than -20°C (253K), the fraction of this cloud type is slowly reduced, while more and more 'mostly liquid' clouds (pink in Figure 3.13) and coexistence clouds (brown in Figure 3.13) are found for higher temperatures. The WBF process depends on the presence of INP, which are observed in higher quantities at mid-latitudes in comparison to the Arctic (compare Figure 3.12). The varying occurrence of different cloud types with temperature - i.e. 'mostly liquid' clouds at higher temperatures (lower altitudes) and an increasing part of 'WBF' clouds with decreasing temperature (increasing altitude) - might correspond to different INP regimes. At temperatures below about -20°C , for example, efficient mineral dust INP initiate the freezing process, while at warmer temperatures less efficient biological particles act as INP (Augustin-Bauditz et al., 2014; Kanji et al., 2017). In addition, the increasing fraction of 'WBF' clouds with decreasing temperature reflects the fact that the colder the environment is, the

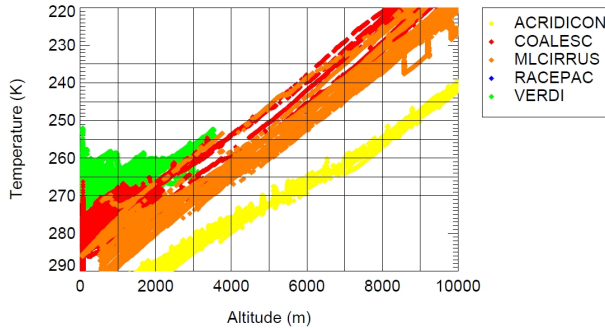


Figure 3.14: Temperature vs. altitude for the four field campaigns VERDI, RACEPAC, COALESC and ACRIDICON-CHUVA. Due to the varying latitudes, the profile differs for the four measurement campaigns.

higher the probability is that the RH_w falls below 100%: With decreasing temperature, more and more droplets freeze and exploit the gas phase water when they grow. In consequence, less gas phase water is available the colder the temperature is. In the transition range between predominantly 'mostly liquid' and only 'WBF' clouds (temperatures between -20 to -10 °C - 253 and 263 K:), 'Coexistence' clouds appear, which can be interpreted as clouds where the freezing process has started, but in which the RH_w is still above 100% (blue curve slightly below RH_w = 100% in Figure 3.2).

Additionally, 'Secondary ice' clouds appear in mid-latitude clouds more often than in the Arctic. It is unlikely that these small particles are shattering artefacts, because they often occur in clouds with no or few large ice particles - these large particles, however, are the ones that usually shatter (Korolev et al., 2011). In contrast, the majority of those clouds occur at temperatures between -5 to -13 °C (268 to 258 K) which is an indication for an efficient Hallett-Mossop process having altered the cloud at slightly warmer temperatures. Note that the classification aims at the result of an cloud transforming processes, not the cloud transformation itself. Which process precisely took place before the cloud section was probed can not be proven with this 1 Hz data set.

At mid-latitudes, 'mostly liquid', 'Coexistence' and 'WBF' clouds show the same vertical velocity distributions (Figure 3.11). The peak updrafts are slightly higher and the widths slightly narrower in comparison to the Arctic clouds. This is another hint that underscores the above discussed dependence of the cloud categories on RH_w: within the same vertical velocity range, the relative humidity can vary strongly depending on the available amount of water and the cloud development stage (cloud particle nucleation, sedimentation, evaporation). The 'Secondary ice' clouds show a different updraft distribution with faster vertical velocities, which might indicate that these clouds occurred in more turbulent environments.

Tropical clouds

During the tropical field campaign ACRIDICON-CHUVA in convective towers, stronger updrafts and downdrafts were observed more frequently than during the other campaigns (Figure 3.11, right panel). The records show extreme vertical velocities up to -10 m s^{-1} and $+15 \text{ m s}^{-1}$. However, these events were rarely observed, because due to flight safety, these cloud sections were mostly avoided. Velocities of 0.5 m s^{-1} to 1.0 m s^{-1} were observed in more than 10% of all data points. The wider distribution of vertical velocities shows that the cloud dynamics are much stronger in the tropical clouds than at mid-latitudes and in the Arctic.

In comparison to the other regions, less 'mostly liquid' clouds are found in the tropics, also for warmer temperatures. This indicates a higher concentration of INP that are already ice active at comparably high temperatures, pointing at biological INP. This seems to be plausible for tropical regions, but is only partially confirmed by the INP estimate (see Figure 3.12, right panel). The probed clouds occurred in both very clean air with less INP than at mid-latitudes case and in heavily polluted areas over fire clearance regions. A more detailed study on how the aerosol concentration affects the cloud type distribution during ACRIDICON-CHUVA was done by Cecchini et al. (2017), also based on NIXE-CAPS aspherical fractions. The study shows that clouds in polluted environments contained more and smaller liquid water droplets and less ice, while clouds in clean conditions held more ice crystals and few liquid water droplets.

As a consequence of the higher vertical velocities in the convective towers, more 'Coexistence' clouds are observed than at mid-latitudes or in the Arctic. A small part of the liquid droplets $< 50 \mu\text{m}$ survived down to the homogeneous drop freezing temperature ($\sim -38^\circ\text{C}$) in cases where the vertical velocity was high enough (see also Figure 3.2, red).

However, the 'WBF/large ice' (Figure 3.13, right panel) clouds are the most frequent at all temperatures. Those large cloud particles might stem from sedimentation out of the cloud anvils, which usually consist of mostly large aggregates, or might be transported downwards in the strong downdrafts within the convective clouds (compare Jäkel et al., 2017).

It is, nevertheless, important to note again that due to security restrictions, the in-situ measurements were mostly restricted to cloud regions with small updraft velocities (see Figure 3.11), i.e. to young developing clouds or edges of convective towers. Due to this flight pattern, conditions were probed that favor the WBF process (consistent with Figure 3.2, blue) even if those conditions might not be representative for tropical convective clouds in general. This part of the analysis should therefore be seen as an incentive for further studies and not be used as a basis for cloud type statistics in tropical dry seasonal convection.

In the tropical dataset, 'Secondary ice' is scarce at the low levels - as at mid-latitudes - but prevalent at cold temperatures, i.e. at high levels. The high concentrations of small aspherical particles might indicate a population of frozen droplets that quickly develop complex shapes in supersaturation. Alternatively, other ice multiplication processes (e.g. ice splintering) take place more frequently at later cloud development stages. Again, shattering artefacts can be excluded as

the reason for the high number of aspherical particles: Large ice crystals appear at temperatures up to 0 °C; the 'secondary ice' cloud type is, however, only observed at temperatures between -38 °C and -20 °C. Additionally, an analysis of inter-arrival times of the 'Secondary ice' cloud sections did not show shorter inter-arrival times than in other parts of the dataset.

3.4 Summary and conclusions

The study presented here gives an overview of typical cloud properties observed between 0 °C and -38 °C ('mixed-phase temperature regime') and links the clouds at differing stages of glaciation to ice formation and evolution mechanisms. It gives hints to the relevance of cloud processes at different geographical locations and altitudes.

To this end, the cloud spectrometer NIXE-CAPS was deployed in four airborne field campaigns to conduct measurements of cloud particle sizes, number concentrations and, as an additional parameter, the cloud particles' asphericity. Based on the observations, which consist of 38.6 hours within clouds, algorithms were developed based on the measurements of particle size distributions and aspherical fractions to identify four cloud types:

- 'Mostly liquid': Dense clouds consisting of mostly small droplets: All particles in the size range from 20 μm to 50 μm are spherical. The few large cloud particles > 50 μm might occasionally include ice crystals.
- 'Coexistence': Dense clouds consisting of mostly small particles with a low percentage (< 50%) of small aspherical ice particles, ice crystals > 50 μm are present. The coexistence of liquid droplets and ice crystals is most probably due to supersaturation over both water and ice caused by higher vertical velocities.
- 'Secondary Ice': Dense clouds consisting of mostly small particles between 3 μm and 50 μm with a high percentage (> 50%) of aspherical ice particles. The aspherical fractions found are comparable to those of cirrus clouds; these clouds are thus completely glaciated. The large cloud particles > 50 μm are also frozen. The ice crystal numbers exceed the expected ice nuclei concentrations by several orders of magnitude, which suggests that the small crystals result from secondary ice production. As shown in subsection 2.5.2, it is not likely that these measurements result from ice particle shattering.
- 'WBF/Large ice': Thin clouds with low number concentrations, whose mass distribution is dominated by large cloud particles > 50 μm ; the aspherical fractions of the small particles are high and the large particles are frozen: These clouds are fully glaciated. The reduced number of small particles in comparison to the 'mostly liquid' clouds can be explained by the WBF process. However, from the asphericity detection it is obvious that small ice crystals are present in WBF clouds with higher concentrations than large ice crystals.

Alternatively, these clouds might consist of sedimenting aggregates. The cloud particle number concentration agree reasonably well with the estimated ice nuclei concentrations.

The occurrence of these cloud types was quantified for Arctic, mid-latitude and tropical regions, respectively.

For the Arctic, mpt clouds were observed at temperatures higher than -20°C . The largest part were 'Mostly liquid' clouds, with a small percentage of 'Coexistence' and 'WBF/Large ice' clouds. This cloud type distribution might be a result of low concentrations of ice active INP, particularly biological INP, during our field campaign in the Arctic. This hypothesis is in agreement with the low INP concentrations found for this region in a modelling study by Wilson et al. (2015).

At mid-latitudes, mpt clouds down to -40°C were probed, mostly in frontal systems with moderate updrafts between 0 and 0.5 m s^{-1} . Here, the glaciated 'WBF/Large ice' clouds dominate most of the temperature range, pointing to a sufficient availability of INP. Only at temperatures warmer than -20°C , increasing fractions of 'Coexistence' clouds and also 'Secondary ice' clouds were found. The temperature range for the 'Secondary ice' clouds is consistent with the preconditions for the Hallett-Mossop process.

In the tropics, mostly moderate, but also very strong vertical velocities were recorded. Correspondingly, the glaciated 'WBF/Large ice' clouds dominate the measurements over all temperature ranges, but also 'Coexistence' clouds are observed down to -40°C . The supercooled liquid droplets freeze homogeneously when transported to higher altitudes. 'Secondary ice' clouds are observed at colder temperatures (higher altitudes) than at mid-latitudes, indicating that other ice splintering processes than the Hallett-Mossop process might be active here.

Pruppacher et al. (1998) summarize several studies that tracked (a) the percentage of clouds containing no ice crystals or (b) the percentage of clouds containing ice crystals as a function of temperature. Their findings agree well with the presented observations at mid-latitudes. It is noteworthy, however, that in none of the studies presented therein, liquid cloud fractions as high as observed during VERDI and RACEPAC were reported.

In general, the analysis of small cloud particle aspherical fractions does not confirm the assumption that all cloud particles smaller than $50\text{ }\mu\text{m}$ are liquid. On the contrary, small particles were frequently found to be aspherical. The aspherical particle fractions are an important parameter for the identification of the four cloud types investigated here. Observations that contain this information (e.g. Mioche et al., 2017) can be used to extend the cloud statistics presented here. In case no small particle shapes are available, particle size distributions can be used to differ between the Type 1 cloud group (mostly liquid/coexistence/secondary ice clouds) and the Type 2 clouds (WBF clouds - large ice). A sufficiently large data base would e.g. allow to quantify the efficiency of the WBF process with regard to temperature and location. Following this line, the NIXE-CAPS dataset might serve as a starting point for a growing cloud type database in the mpt regime.

4 Simulation of NIXE-CAPS observations during ML-Cirrus using CLaMS-Ice

4.1 Motivation

It is generally assumed that the majority of cirrus clouds, which cover significant parts of the earth (Liu et al., 2012), have a warming effect on climate (Boucher et al., 2013). The actual effect of cirrus clouds on the radiation budget, however, depends on the clouds' microphysical properties such as ice crystal concentration, size and shape (e.g. Kienast-Sjögren et al., 2015; Barthelmebs, 2015; Kienast-Sjögren et al., 2016). In-situ measurements have shown that cirrus clouds with potentially cooling properties exist (Luebke et al., 2016). Krämer et al. (2016b) hypothesize that the occurrence of the related microphysical properties might be connected to cirrus cloud formation out of a liquid cloud, i.e. the lifting of a formerly mixed-phase cloud into the cirrus cloud temperature regime, where all remaining liquid water freezes spontaneously ('liquid-origin cirrus', see chapter 1). These clouds have larger particles and higher cloud particle concentrations than 'in-situ origin cirrus', which form directly as ice clouds at temperatures below 238 K (Luebke et al., 2016; Krämer et al., 2016b). Backward trajectory analyses performed by Luebke et al. (2016) support this assumption. To quantify the occurrence of such clouds, model studies are necessary that provide both the microphysical information of the simulated clouds and their spatial extension on large (regional to global) scales.

CLaMS-Ice is a newly developed large-scale cirrus forecast and analysis tool. The CLaMS-Ice model consists of a detailed microphysical cirrus cloud box model (Spichtinger and Gierens, 2009a,b) which can be operated along trajectories of the global Lagrangian model CLaMS (Chemical Lagrangian Model of the Stratosphere, see McKenna et al., 2002a,b; Konopka et al., 2004). The box model's two-moment bulk approach compromises between the accurate representation of microphysical parameters and the computational efficiency required for large-scale simulations. It includes the main mechanisms for in-situ origin cirrus cloud formation: heterogeneous ice nucleation on ice nucleating particles (INP), and homogeneous nucleation of liquid solution particles of sulphuric acid. In addition to in-situ origin cirrus clouds, CLaMS-Ice also represents liquid-origin cirrus by transferring liquid and ice water content from ECMWF meteorological fields into the cirrus temperature regime; assuming that all liquid water freezes as soon as the trajectory crosses the temperature threshold of 238 K.

Based on CLaMS-Ice, it is possible to track the origin of cirrus clouds, their formation mechanisms

together with the frequency of occurrence of the respective cloud types. Thus, from CLaMS-Ice simulations, new insights on cirrus clouds microphysical and thus radiative properties are expected. As a first, important step, CLaMS-Ice has to be validated based on in-situ observations, which is done in this part of the study: the model's performance is tested against high-performance in-situ measurements of the NIXE-CAPS cloud spectrometer (see chapter 2) during the airborne campaign ML-Cirrus 2014 (see Voigt et al., 2016). Further, it addresses the question whether CLaMS-Ice simulations are suitable for predicting the regional or global cirrus cloud properties - the key parameters for modelling the cirrus' influence on the radiation budget.

The two-moment scheme in combination with the sedimentation provides an advantage of CLaMS-Ice e.g. over studies using solely the ECMWF cloud water content datasets (e.g. Wernli et al., 2016). When backward trajectory analyses are used to assess whether or not a cloud was influenced by a mixed-phase state, it is important to take into account that especially cloud particles formed via the Wegener-Bergeron-Findeisen process (see section 3.1) are usually large, and sediment fast. Close to the region where water content is transported from warm regions to temperatures below 238 K, the cirrus cloud might be influenced strongly by the cloud's mixed-phase past. However, this influence will decrease and then vanish after some hours of cloud evolution. Analyses that are based on cloud ice water contents alone cannot assess such microphysical developments (cf. Case Study III).

4.2 Brief description of the ML-Cirrus campaign

ML-Cirrus took place in Oberpfaffenhofen, South Germany, in March and April 2014. 16 flights were conducted over Western Europe (Germany, Netherlands, England/Scotland, France, Spain, Portugal, Italy, Austria) with a total of 23 hours within ice clouds. Various meteorological situations were probed: warm conveyor belts and conveyor belt outflows, lee waves, high pressure cirrus, jet stream induced cirrus, front cirrus, contrails and contrail induced cirrus. HALO (High Altitude and Long Range Aircraft) served as a platform; it was operated by DLR-FX, Oberpfaffenhofen, and carried redundant cloud instrumentation (see Voigt et al., 2016). Key parameters for the comparison between CLaMS-Ice simulations and observations are temperature, relative humidity, ice particle number concentrations and ice water content. The latter two parameters are obtained by the NIXE-CAPS instrument (see chapter 2); temperature data are taken from the BAHAMAS dataset (Basic HALO Measurement And Sensor system; DLR); relative humidities are provided by the SHARC instrument (Sophisticated Hygrometer for Atmospheric Research; DLR).

With regard to the temperature data, it has to be taken into account that there are strong indications for a bias in the BAHAMAS data. Both temperature data comparisons to ECMWF (Schumann, 2015) and the evaluation of in-cloud relative humidities during the campaign (Figure 4.1) give hints that the BAHAMAS temperatures are about 0.5 K too high. When

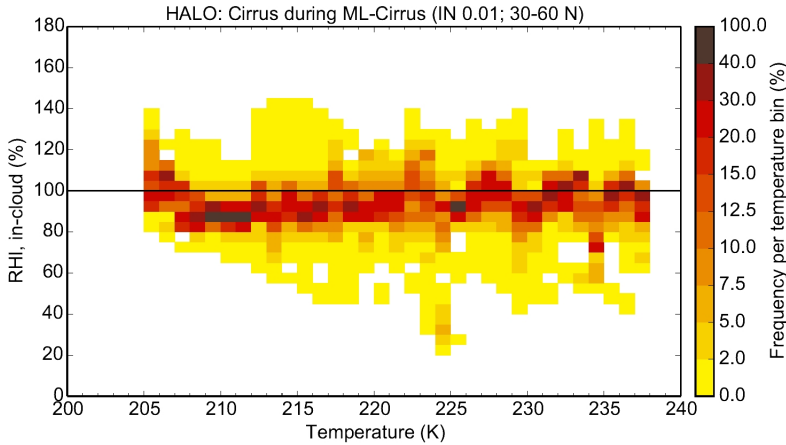


Figure 4.1: Probability of occurrence of RHi measurements within clouds as a function of temperature. The expected distribution would have a peak at RHi = 100%. Graphic: courtesy of Christian Rolf.

correcting for this, the peak of the RHi distribution would lay in the thermodynamic equilibrium of 100%. This potential bias has to be taken into account when comparing the temperature and RHi simulations from CLaMS-Ice to the in-situ observations.

The observed ice water contents are calculated from NIXE-CAPS number concentrations and measured size distributions as described in Krämer et al. (2016b). With its measurement range from 3 to 937 μm , NIXE-CAPS covers most of the relevant cloud particle spectrum. As a reminder, however, several measurement uncertainties add up when calculating IWCs from the particle observations (see section 2.5). A deviation of one order of magnitude between model simulations and observations can therefore still be regarded as good agreement.

In contrast, only uncertainties regarding the sampling volume and, to some extent, the particle sizing add up to the total uncertainty of the observed cloud particle number concentrations (cf. section 2.5). A deviation of one order of magnitude between model simulations and observations will still be used as 'agreement' criterion, because the concentration range of cirrus clouds covers several orders of magnitude: cloud simulations that represent the correct order of magnitude can be considered to be successful.

When comparing observations and simulations for the ML-Cirrus dataset, special care has to be taken with regard to artificial cirrus, i.e. contrails. Some measurement flights were dedicated to probing contrails immediately, or focussed on regions where cirrus clouds were - according to the CoCIP model (see Voigt et al., 2016) - initiated by contrails. Such clouds cannot be reproduced by CLaMS-Ice. In the observational dataset, the contrail segments are difficult to exclude, because their typical appearance (NO_y signature, large concentrations of small particles) quickly change towards the profile of natural cirrus clouds as the contrail is ageing. As long as those

segments cannot be identified in the dataset, simulations and observations are bound to show differences.

4.3 Coupling 3D trajectories with ice microphysics

CLaMS-Ice was established as a cirrus cloud forecast tool for measurement campaigns. As such, it has to meet specific requirements: it should need less calculation time than detailed microphysical models such as MAID (Bunz et al., 2008), which follow a sophisticated microphysical scheme and provide detailed results. On the other hand, it needs to provide more detailed information on the simulated clouds than low resolution products like the ECMWF forecasts, which are easily obtainable but provide no microphysical cloud characteristics (high/low ice crystal number concentrations, thin/thick cloud, expected cloud lifetime and so on). CLaMS-Ice performed reasonably well during the ML-Cirrus campaign. Its forecast products were used for flight planning and, later, showed a good agreement with the actual cirrus cloud cover found on satellite images (Rolf et al., 2015). The comparison presented here aims to show the agreement of the microphysical parameters 'ice particle number concentrations' and 'ice water content' between the simulation results and in-situ observations obtained during ML-Cirrus.

4.3.1 CLaMS trajectories

To initialize the model, 6 hourly ECMWF meteorological data are fed into the Chemical Lagrangian Model of the Stratosphere (CLaMS, McKenna et al., 2002a,b; Konopka et al., 2004) (see Figure 4.2). Various ECMWF products can be used, e.g. the operational forecasts (for flight planning), the operational analyses, or the ERA-Interim datasets for long-term studies. Based on locally interpolated temperature, pressure and wind fields, backwards trajectories with a length of 24 hours are calculated that show the origin of air masses that are sampled along the flightpath of the HALO aircraft during ML-Cirrus. Figure 4.4 illustrates the trajectory calculation, Figure 4.3 shows an example from the campaign. Alternatively, the backward trajectories can be started from grid points covering any extent of the latitude/longitude/pressure altitude space.

In the study presented here, temperature, pressure and wind fields are taken from ERA-Interim. The region of interest - where cirrus clouds form - is close to the tropopause. In regions with an atmospheric pressure larger than 300 hPa, vertical air movements and the associated temperature changes can be described well by the vertical velocity ω , the change in pressure over time. In the stratosphere, where the pressure gradient is very low, vertical movements are described by $\dot{\theta}$, the change in the potential temperature over time. For the CLaMS-Ice trajectories in the tropopause region, CLaMS uses the hybrid vertical coordinate zeta (Konopka et al., 2007), which allows a transition from pressure coordinates to potential temperature coordinates. The underlying vertical coordinate for the trajectory calculation changes at the 300 hPa level in the

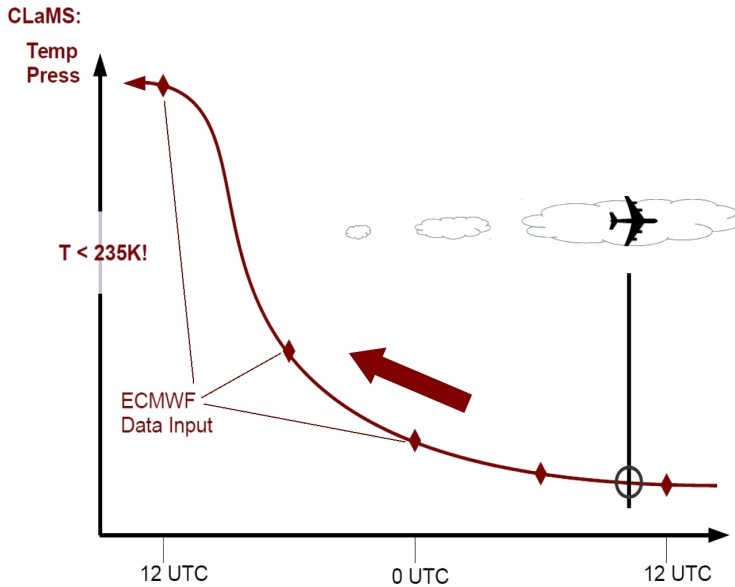


Figure 4.2: 24 backward trajectories are calculated by CLaMS that show the air parcel origin and the temperature/pressure history before the air reached the flightpath. Temperature, pressure, relative humidity and ice water content based on the ECMWF data fields are assigned to the trajectory.

ERA-Interim data.

The coarse ECMWF data does not represent the full range of temperature fluctuations in the atmosphere (Kienast-Sjögren, 2015). Small-scale fluctuations (e.g. induced by gravity waves) can play an important role in the cirrus' nucleation phase, where small changes in the relative humidity cause large differences in the resulting ice crystal concentrations. It is therefore essential to consider these fluctuations especially for simulations of inhomogeneous cirrus layers (Krämer et al., 2016b). Therefore, small fluctuations are adiabatically superimposed on the trajectory temperature and pressure, following a parametrization by Gary (2006).

A critical point that will persist to cause uncertainties in the cirrus cloud simulations with CLaMS-Ice is the ECMWF water vapour input. Under- and overestimations of the water content are frequently found (Lamquin et al., 2009; Rolf et al., 2012; Kunz et al., 2014) and might lead to cloud formation at wrong locations, with a negative influence not only on the microphysical cloud characteristics, but also on the expected temperatures and humidities.

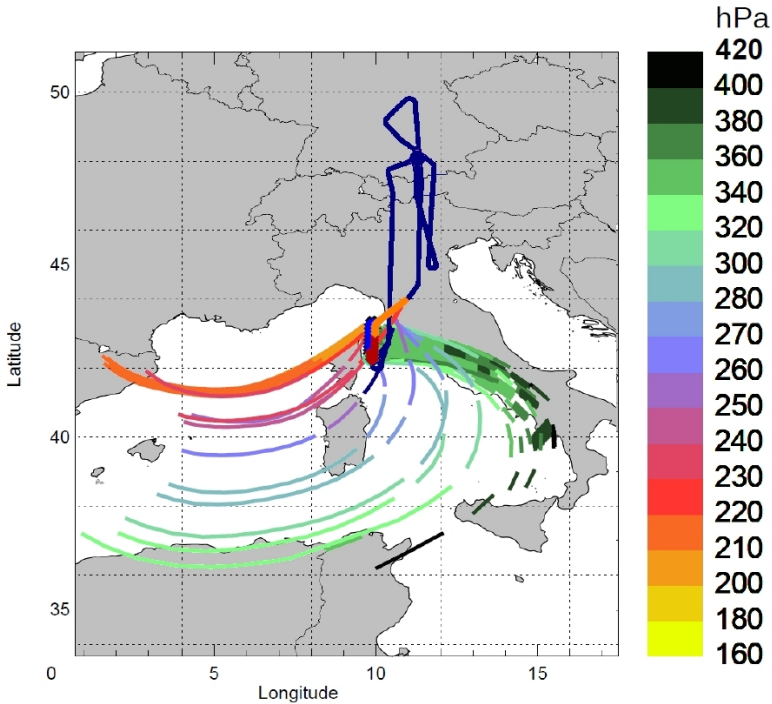


Figure 4.3: Backward trajectories on different pressure altitudes starting at the flightpath (dark blue line) of HALO flight 06 of ML-Cirrus, 27.03.2014.

4.3.2 Microphysical ice cloud simulation in CLaMS-Ice

Along the trajectories, the temperature and pressure forcing is used to simulate the formation and evolution of cirrus clouds, using the bulk model by Spichtinger and Gierens (2009a,b) (see Figure 4.4). The starting point is the earliest possible point in time on the trajectory, in the presented case 24 hours before reaching the flightpath. If the trajectory originates in regions warmer than 238 K, CLaMS-Ice starts the simulation where the temperature falls below 238 K. At this starting point, the ECMWF water vapour values are used as initial humidity for the CLaMS-Ice cloud simulation. After starting the simulation, the model uses the temperature and pressure values in each time step and calculates the respective relative humidity, which drives the cloud formation, evolution or sublimation.

Heterogeneous and homogeneous ice formation in the two-moment scheme

When a cloud-free air parcel is cooled, its relative humidity (RH_i) rises and will eventually reach the critical supersaturation threshold for ice nucleation. The bulk model applies homogeneous

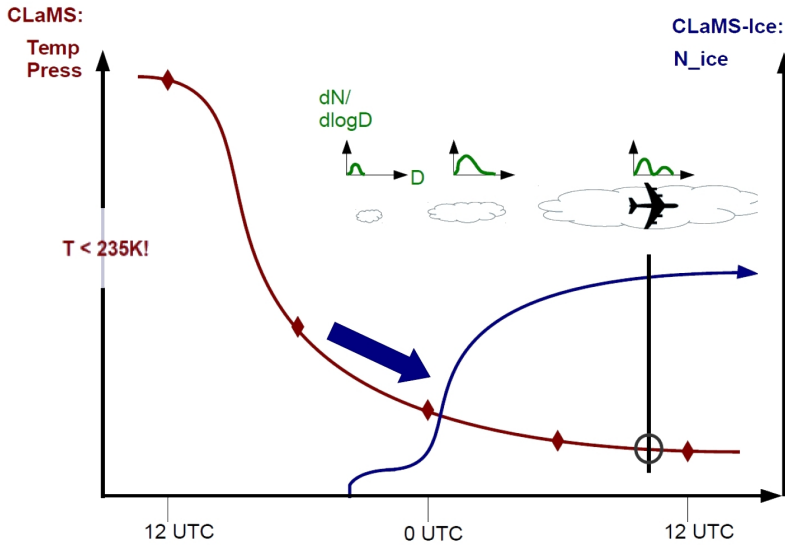


Figure 4.4: CLaMS-Ice simulates cirrus clouds in forward direction along the trajectories (red line, see Figure 4.2). As an air parcel cools along its trajectory, a cloud can form and the ice particle concentration (N_{ice}) is rising (blue line).

and heterogeneous ice nucleation depending on the availability of Ice Nucleating Particles (INP), which are quantified during the model initialization. The two nucleation mechanisms will be described shortly in the following (after Pruppacher et al., 1998; Koop et al., 2000; DeMott et al., 2010).

The air contains small particles such as mineral dust, bacteria, and sea salt. These particles can act as INP by providing a surface for ice deposition. The critical supersaturation threshold necessary for heterogeneous ice nucleation depends on the involved INP. In CLaMS-Ice, the initial concentration of INP and the associated supersaturation threshold are provided in an initialization file (see subsection 4.3.4), which allows the operator to choose different kinds of particles depending on the location of the simulation.

The ice particles formed by heterogeneous nucleation are described by the ice particle concentration information (N_{cloud}) in one moment of the model and by the ice particle masses in the second moment. CLaMS-Ice's two-moment scheme thus covers ice particle number concentration and ice mass independently. Particle sizes are derived from the ice mass using a pre-described log-normal particle size distribution. Due to deposition, the ice particle masses grow as the air parcel is cooled further, thus keeping the RH_i close to 100%. The larger the ice particle masses are, however, the faster the sedimentation (see section 4.3.2) becomes: N_{ice} is therefore decreasing. At some point, there are not enough ice crystals left to stabilize the relative humidity

at 100% by taking up water from the gas phase. The RH_i rises again, and when there are no INP for heterogeneous nucleation left in the air parcel, it can rise to supersaturations higher than the critical threshold for heterogeneous ice formation. If the air parcel is cooled long enough, it will then eventually reach the threshold for homogeneous freezing.

During the homogeneous ice nucleation, liquid solution particles (such as sulphuric acid) with radii smaller than 1 μm freeze at supersaturations of about 140% and higher, depending on the temperature (Koop et al., 2000). Homogeneous freezing events usually happen after the heterogeneous freezing due to the high required supersaturations. It can also constitute the first freezing event in case the respective air mass is very clean, i.e. does not provide INP for a heterogeneous nucleation. When the cooling rate is very large (e.g. in lee waves), a homogeneous nucleation can also take place before the heterogeneous nucleation is finished.

In CLaMS-Ice, heterogeneous freezing can be switched off completely by initializing the model with an INP concentration of 0. In this case, the RH_i may rise until it reaches the homogeneous freezing threshold.

Pre-existing ice: Boudala parametrization

If ECMWF predicts a cloud at the starting point of a trajectory, the ice water content is used to characterize this 'pre-existing cloud' in CLaMS-Ice by applying the Boudala et al. (2002) parametrization, which defines ice particle sizes as a function of temperature. The radius found for the respective temperature is used as the mode diameter in a lognormal size distribution. From the particle sizes and the ice water content, ice particle masses and number concentration can be derived for the trajectory starting point. This so-called 'pre-existing ice' is then fully implemented into both moments of CLaMS-Ice and is not treated differently from clouds that form later.

Note that pre-existing ice can occur for both in-situ and liquid origin cirrus clouds: When a trajectory originates in a cold area, e.g. at 220 K, any ice water content that already exists at the starting point of the trajectory will also be classified as 'in-situ origin'. When the trajectory starts at the temperature transition from warm areas to those colder than 238 K, the pre-existing ice leads to a classification as 'liquid origin' cloud. (For more details, see subsection 4.3.5.)

Sedimentation

Depending on the location of an air parcel within the cloud, the parcel might receive ice crystals sedimenting from cloud layers above. In CLaMS-Ice, a sedimentation factor specifies what percentage of particles falling out of the simulated air parcel are replaced by particles falling into this air parcel, as proposed by Spichtinger and Gierens (2009a,b). This setup allows to model cloud tops by applying a sedimentation factor of zero, i.e. no particles that sediment out will be replaced. For middle and base regions, which receive particles that sediment out of higher layers, the sedimentation factor can be chosen between 0 and 1.

The ice mass and the IN associated with the sedimenting particles are permanently removed from the simulated air parcel.

4.3.3 Model acceleration by variable time steps

A reasonable runtime of the model for large scale cirrus simulations is an essential requirement for usage as a forecast tool e.g. on measurement campaigns. Thus, CLaMS-Ice uses a flexible time step for these calculations. Whenever the simulated air parcel is cloud-free and has a relative humidity (RH_i) below 100% for the current and the next time step, the model increases the time step to 10 minutes to save calculation time. When ice nucleation becomes possible (RH_i > 100%), but the cloud is not expected to form yet within the next time interval, the time step is reduced to one minute. In general, the modelling time step is 1 second while clouds are present in the model. Both within existing clouds and in cloud-free air, the model time step is further reduced to a 0.1 seconds close to the homogeneous freezing threshold, where the cloud development changes at very small time intervals. If the cloud vanishes in the trajectory, either due to sublimation or due to sedimentation, the time step is enlarged again. A second case in which the time step is modified is when the trajectory is approaching the flightpath. First comparisons have shown that the model results are very sensitive to the time steps chosen in this area. As many flights were conducted in the troposphere - with occasionally strong vertical movements in the atmosphere - it is vitally important that the model trajectories end exactly at the latitude, longitude and altitude of the flightpath for comparing simulations and observations. This cannot be granted when, close to the flightpath, a fixed model time step is applied: The fixed time step might cause the trajectory to end e.g. one minute before reaching the flight path. In strong vertical motions during ML-Cirrus, cooling rates of more than 7 Kelvin per minute were found. In this example, one minute discrepancy between the trajectory end and the flightpath means that the simulated cirrus cloud will represent the conditions of a point 700 meters below the flightpath and 7 Kelvin warmer. A comparison to the observations made at the flightpath is therefore not meaningful.

4.3.4 CLaMS-Ice initialization

For the initialization of CLaMS-Ice, an initialization file has to be written that specifies a number of input parameters into the model. For the model performance tests, the following setups has been chosen on the basis of model studies with the MAID model (Rolf et al., 2012): At a critical supersaturation of 120%, heterogeneous ice nucleation will start, using INP of an initial concentration of 0.01 cm^{-3} . The initial concentration of H_2SO_4 particles - required for homogeneous ice nucleations - is 300 cm^{-3} . The sedimentation rate is set to 0.9, i.e. 90% of the particles sedimenting out of the simulated air parcel are replaced in the model. This setup resembles the situation in the middle of a cirrus cloud (Spichtinger and Cziczo, 2010). Additionally, a 'water factor' and 'water offset' can be chosen, which modify the water input

from ECMWF by a factor or a given amount of water vapour, respectively. For the general model performance tests, the water input was not modified.

4.3.5 Identification of in-situ and liquid origin cirrus clouds

Luebke et al. (2016) have shown that the microphysical properties of cirrus clouds depend on the region they originate in: 'Liquid origin cirrus' that were formed at warmer temperatures where liquid water can still exist reach larger particle number concentrations and ice crystal sizes due to the increased abundance of water vapour at warmer temperatures. 'Liquid origin' clouds can also contain ice particles that were formed via a liquid phase, e.g. from droplet freezing, from the Wegener-Bergeron-Findeisen process or similar.

In contrast, 'in-situ cirrus' form at cold temperatures directly via the ice phase. In these cold regions, less water vapour is available, resulting in lower number concentrations and smaller cloud particle sizes.

In the CLaMS-Ice dataset, these two cirrus types can be distinguished by analyzing the cloud history along the trajectory.

As in Luebke et al. (2016), the label 'in-situ' is applied when a trajectory

- never encountered temperatures warmer than 238 K during the 24 hours before reaching the flightpath
- never contained ice water content
- did not contain ice water content in sections warmer than 238 K but contains some later, at colder temperatures OR
- did contain ice water content from warmer regions to regions below 238 K but lost all of this IWC at some point before reaching the flightpath.

Again following Luebke et al. (2016), the label 'liquid origin' is applied when a trajectory

- originates in an atmosphere region warmer than 238 K
- already carries cloud particles in this section AND
- preserves some of those cloud particles until it reaches the flightpath

4.4 Simulations of ML-Cirrus clouds and CLaMS-Ice performance

4.4.1 Comparing simulations and observations

All in-situ observations were made along the flight paths of HALO during the ML-Cirrus campaign (see section 4.2). Basis for this study are 1 Hz data of temperature, relative humidity, ice particle number concentrations and ice water content (derived from ice particle concentrations). Each

measurement is associated with a position (latitude, longitude, pressure altitude) and a time stamp.

Backward trajectories are started at every minute of the HALO flight, i.e. relying on minutely values of latitude, longitude, and pressure altitude provided by the HALO instrumentation. The model thus provides one simulation per minute of flight; these results are interpolated to 1 Hz along the flightpath.

Alternatively, a comparison would have been possible by interpolating the 1 Hz observations to a minutely time grid to match the trajectories. This approach, however, would have a significant disadvantage: it would smooth all values, minimizing the observed variance along the flightpath, and thus hiding maximum supersaturations, maximum cloud particle concentrations and so on. In the simulation results for the flightpath, however, these values would still occur and would mislead to larger deviations between model and observations.

In subsection 4.4.2, all cirrus clouds that were observed during ML-Cirrus are compared to the respective model representations. This is helpful for a first glance at the model performance but can be an obstacle in the search for model errors, as the observed clouds form under various, very different conditions (compare Figure 1.1) and might show different sensitivities to the same input parameters. Subsequently, the clouds are therefore divided into two large, but microphysically different groups: insitu formed cirrus and liquid origin cirrus (Luebke et al., 2016, see further subsection 4.4.3 and subsection 4.4.4).

4.4.2 Overall model performance

To assess the overall model performance, CLaMS-Ice was initialized with the 'basic setup' for all flights of ML-Cirrus. The chosen parameters for this setup are described in subsection 4.3.4. The overall comparison between observations and simulations was done for the modelled parameters temperature, relative humidity, ice particle number concentrations and ice water contents independently.

Temperature. The temperature predicted by CLaMS-Ice along the flightpath differs from the ECMWF temperature. ECMWF parametrizes cloud processes on large scales; the temperature changes thus include e.g. latent heat release due to cloud particle growth, or latent heat uptake by sublimating ice. The cloud cover in ECMWF, however, differs from the one predicted by CLaMS-Ice. That means that the ECMWF temperatures might be influenced by diabatic processes, even though CLaMS-Ice predicts cloud free air for the respective section. Where clouds occur in both models, CLaMS-Ice would add its own latent heat release to trajectory temperatures which already account for diabatic temperature changes. This would result in an unrealistic warming.

Therefore, CLaMS-Ice only uses the ECMWF temperature fields as an input at the starting

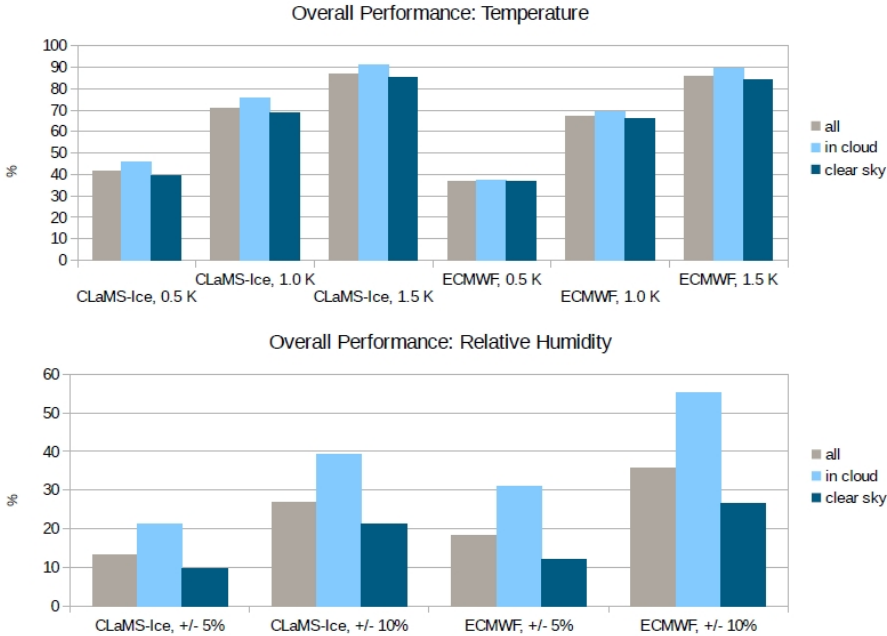


Figure 4.5: Agreement between CLaMS-Ice and ECMWF and observations during ML-Cirrus: The values show for how many data points the agreement criterion was fulfilled. This criterion (tolerated deviation) is given below the bars. Top: Temperature comparison based on BAHAMAS data, bottom: RHi comparison based on SHARC data.

point of each trajectory. From then on, the trajectory is defined by changes in pressure alone, and the temperature is found as the result of adiabatic warming or cooling by keeping the potential temperature θ constant, as long as no cloud processes take place. During cloud formation or sublimation, the temperature is additionally modified by diabatic cloud processes. This approach guarantees that the temperature data along the trajectory only contain adiabatic changes from ECMWF, while diabatic changes originate from CLaMS-Ice.

CLaMS-Ice and ECMWF temperatures should therefore be compared to the observed values separately.

The BAHAMAS temperature sensor on HALO has a possible bias of about 0.5 K (see section 4.2). An agreement of 0.5 K or smaller is therefore the maximum possible agreement between simulations and observations of the temperature. In the basic model setup, 41% of all observations on the flight path agreed within +/- 0.5 K with the CLaMS-Ice temperature (see Figure 4.5, top). Hereby, 46% of the simulated values are within the measurement uncertainties, if only flightpath segments within clouds are considered. Under clear-sky conditions, only 39% of the results match the measurements.

An agreement within ± 1 K is still tolerable. The most important impact of temperature errors is the relation between temperature and relative humidity (RH_i). 1 K temperature deviation translates to an uncertainty of $\pm 10\%$ regarding the RH_i in the cirrus temperature range below 238 K. 71% of all simulated CLaMS-Ice values agree within ± 1 K with the measurements. Concerning the flightpath segments within clouds, 75% of the simulated values are within this range, and 69% for clear-sky conditions.

Furthermore, the agreement within ± 1.5 K has been tested. 87% of all simulated values lie in this range, 91% of the values within clouds, and 85% outside clouds. Strong deviations > 1.5 K are therefore rare.

In conclusion, the deviations are usually smaller than 1.5 K, but this difference can already have a critical influence on the relative humidity, especially for regions near saturation or near the ice nucleation thresholds. Since the temperatures are influenced by the formation and sublimation of clouds, a suboptimal cloud representation in CLaMS-Ice might be a reason for these temperature deviations. It is, however, also possible that the initial temperature values from ECMWF cause errors. To investigate this, the following paragraph compares the original ECMWF temperature fields, interpolated to the flightpath, with the observations.

With 37% (± 0.5 K), 67% (± 1 K) and 86% (± 1.5 K), the ECMWF values score similarly to the CLaMS-Ice values. This dataset, too, compares better to the observations within clouds (37%/69%/90%) than in the sections outside clouds (37%/66%/84%). From this, it can be concluded that temperature uncertainties probably come from the ECMWF input data.

Overall, the model performance with regard to temperature requires improvement to provide a good basis for the calculation of relative humidities during the cloud simulation. A better representation of the cloud microphysical properties in CLaMS-Ice might lead to a positive effect on the temperature comparison, because the latent heat release might influence the temperature development. It is, however, also important to note that more precise temperature observations would be a precondition for a meaningful closure between simulations and measurements.

Relative humidity (RH_i). As it can be expected from the temperature comparison, the RH_i doesn't compare well between simulations and observations (see Figure 4.5, bottom). With more than 50% of all model values deviating by 0.5 K and more from the measured temperature, the relative humidity is likely to suffer from its temperature dependence.

Additionally, the RH_i reacts non-linearly to the CLaMS-Ice input parameters. The most significant factor for the RH_i simulated on the flightpath is the point in time of the last cloud nucleation event. Often, a trajectory causes the simulated cloud to reach the homogeneous freezing threshold multiple times in a row: of all trajectories in which cloud formation takes place, 60% have more than one nucleation event. Within these, there are on average 2.84 IWC maxima along the trajectory on hourly scale; a finer time grid might reveal more maxima. In consequence, the relative humidity often oscillates between 100% and 140-160% on hourly or sub-hourly scales along the trajectory. Furthermore, too early and/or too numerous nucleation

events might dry the trajectories too efficiently, thus leading to nucleation events near the flightpath that don't represent the actual clouds.

In this context, it is not surprising that only 13% of all simulated RH_i values lie within +/- 5% of the observed values. Within clouds, they compare significantly better (21%), mirroring the better temperature agreement between observations and simulations inside clouds.

The original relative humidities calculated from ECMWF water vapour and temperature fields compare better to the measurements than the simulation results (31% for all values, 18% within clouds). Since the temperatures of the ECMWF fields did not compare better than CLaMS-Ice, these differences in the agreement seem to come from the cloud microphysics in CLaMS-Ice.

When allowing a larger range of +/- 10% of difference between observations and simulations, the CLaMS-Ice results show agreements of 27% (all values) and 39% (within clouds). The ECMWF fields still agree better (36% and 55%, respectively).

Cloud ice water content (IWC). The model/observation comparison is limited by the accuracy of the cloud cover simulated by CLaMS-Ice. Ice water contents can only be compared for all cases where i) a cloud was observed on the flightpath and ii) CLaMS-Ice simulated a cloud for the same segment. As a first step, it is therefore assessed for which percentage of values one of the following criteria is fulfilled ('cloud cover representation'):

- NIXE-CAPS reports 'no cloud on flightpath', i.e. the ice number concentration is below 0.001 cm^{-3} (NIXE-CAPS detection limit, see chapter 2), AND CLaMS-Ice reports 'no cloud on flightpath', i.e. $\text{IWC} = 0$
- NIXE-CAPS reports an ice number concentration larger than 0.001 cm^{-3} AND CLaMS-Ice reports IWC larger than 0

In the standard setup, CLaMS-Ice reports the cirrus cover for 82% of the campaign correctly. Within all modelled clouds that were formed at flight segments containing clouds during the measurements, for 17% the IWC agreed within one order of magnitude with the observations. If the tolerated deviation is increased to two orders of magnitude, 23% of the simulated values match the observations. These results will be discussed together with the evaluation of cloud particle number concentrations.

The IWC is also available for ECMWF data. Here, 26% of all modelled values lie within the measurement uncertainty of the observations, and 33% within two orders of magnitude. However, only 67% of all values match the observed cirrus cloud cover in the ECMWF fields. The overall representation of clouds is therefore significantly worse than in CLaMS-Ice.

Cloud particle number concentrations. While in case of the IWC, all values larger than 0 were considered to be a 'cloud' in the model, the ice particle number concentrations have a limit: Whenever the model simulates particle number concentrations below 10^{-5} cm^{-3} , all

remaining particles are deleted. This approach saves calculation time, as cloud-free air parcels are treated with larger time steps. The cloud cover comparison in terms of N_{ice} , however, shows slightly different values than for the IWC.

In all simulated values, the observed cloud cover is represented accurately in 84% of the cases. This is slightly better than for the IWC comparison. Only 12% of the simulated N_{ice} , however, lie within one order of magnitude of the observed values, and 20% lie within two orders of magnitude from the measurements.

ECMWF does not provide ice particle number concentrations and can therefore not be compared here.

Reasons for suboptimal agreement with regard to IWC and N_{ice} . There are several possible explanations for the poor agreement in the comparison between CLaMS-Ice and observations regarding the parameters IWC and N_{ice} . One is that the observed variability for 1 Hz ice water contents and N_{ice} can be high in cirrus clouds (compare Figure 1.2). The second-to-second comparison can output bad numbers, even if median values and variability of the cloud's microphysical properties are captured accurately by the model.

A second reason is again the model sensitivity to the moment in time when a cloud nucleates (Figure 4.6). Especially in slow updraft, the model clouds consist of ice particles that grow to large sizes and sediment relatively fast. If the updraft continues, a new cloud will form eventually, leading to large oscillations in the IWC and N_{ice} along the trajectory. The period of these oscillations changes significantly if the model input is modified; e.g. less IN can cause the first cloud to grow to larger particle sizes and thus sediment fast, triggering an earlier second cloud formation, and so on. This non-linear behaviour is a constraint to an iterative search for correct model input parameters.

The missing part of small-scale temperature fluctuation and its replacement by the Gary (2006) parametrization might influence the comparison in a negative way, as nucleation events can be triggered too early or too late due to missing fluctuation frequencies (see subsection 4.3.1 and Kienast-Sjögren et al., 2015).

Once again, the small-scale inhomogeneities found in the CLaMS-Ice simulations at the flightpath can accurately describe the actual cloud situation. The quality of the cloud representation, however, is difficult to grasp in a direct model-to-observation comparison.

The local comparisons between in-situ observations and CLaMS-Ice simulations have large deviations, but a climatological analysis by Rolf et al. (2015) shows that the general range of simulated IWC and N_{ice} as a function of temperature agree well with the respective range in the observations. This climatological analysis does not restrict the comparison to the flightpath, which minimizes the influence of the inhomogeneities described above. This means that on average, the input parameters into the model seem to represent the actual atmospheric conditions, and CLaMS-Ice is able to simulate the microphysical properties of the bulk cloud population. A higher modelling resolution (i.e. a higher trajectory density) might allow to re-evaluate the

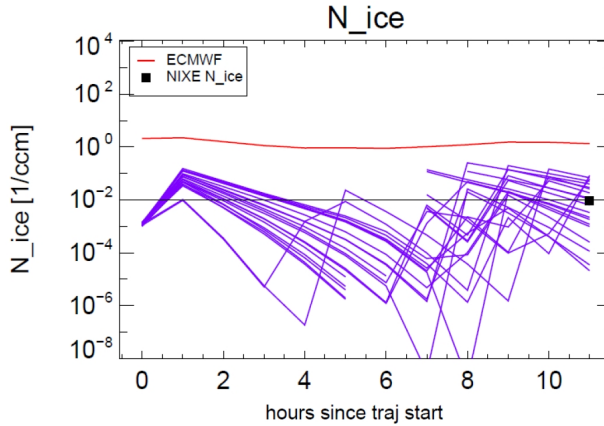


Figure 4.6: Random temperature fluctuations after Gary (2006) trigger cloud nucleation events at different points along the trajectory. This has a strong influence on the comparison between simulation and observation at the end point of the trajectory. Purple: Simulated trajectories, black square: NIXE-CAPS observation at flightpath.

simulated clouds at the flightpath and would likely yield better results, as in this case, the parameter variance could be considered in addition to the direct comparison.

4.4.3 Model performance, insitu cirrus

Temperature. Again, the selected trajectories contain clouds and cloud-free segments. Those regions are compared separately.

Inside insitu cirrus clouds, the temperature representation for insitu trajectories is better than the average shown in subsection 4.4.2 with an agreement of 46% (± 0.5 K), 77% (± 1 K), and 91% (± 1.5 K), as shown in Figure 4.7 (top). In clear-sky segments it is significantly worse (39%/68%/85%). Interestingly, the insitu CLaMS-Ice results are here slightly better than the comparison of the whole trajectory set described in the previous section, especially for the comparison with ± 0.5 K. Inside insitu cirrus, the ECMWF values match 39% (± 0.5 K), 74% (± 1 K), and 93% (± 1.5 K) of the observed values; under clear-sky conditions these numbers decrease to 35%/66%/84%.

Relative Humidity (RH_i). The relative humidity comparison remains poor (see Figure 4.7, bottom). 16% of all CLaMS-Ice output values reach the observations with $\pm 5\%$ within clouds, 31% with $\pm 10\%$. Under clear-sky conditions, only 9% and 21% agree with the observations. With 25% ($\pm 5\%$)/46% ($\pm 10\%$) within clouds and 12%/26% in clear-sky segments, the ECMWF values correspond better to the measurements.

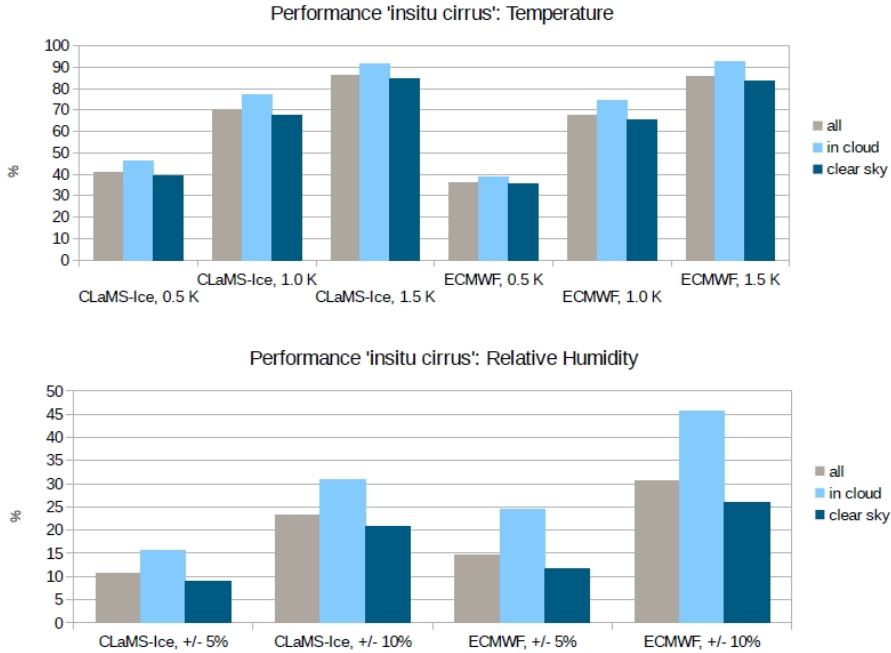


Figure 4.7: Agreement between CLaMS-Ice/ECMWF and observations as in Figure 4.5, but restricted to insitu cirrus clouds during ML-Cirrus. Top: Temperature comparison, bottom: RH_i comparison.

Cloud ice water content (IWC). Regarding the IWC, the cloud cover representation in CLaMS-Ice remains good (85%), and is still superior to the ECMWF predictions (66%). The actual IWC comparisons, however, are worse for in-situ cirrus than for the overall campaign: Only 15% of all CLaMS-Ice IWCs are within two orders of magnitude from the observed values, and 10% within one order of magnitude. The ECMWF values are also worse than the campaign average: They match in 24% and 19% of all in-situ cases, respectively. The reason for this decrease in agreement might be that for in-situ cirrus clouds, the point in time of a nucleation event plays a more critical role for the simulated cirrus on the flightpath than in the case of the liquid origin clouds, where an air parcel carries a larger number of ice crystals for a longer time (see subsection 4.4.4). As mentioned before, this point in time depends strongly on small-scale temperature fluctuations, which are not represented in the ECMWF datasets. Also, insitu cirrus occur in a wide range of relative humidities between slightly subsaturated (about 80%) to strongly supersaturated (up to 170%) conditions (Krämer et al., 2009). The relative humidities in the ERA-Interim dataset - which are used to model clouds - were found to occasionally show large differences to observations (Kunz et al., 2014, , see also subsection 4.5.1).

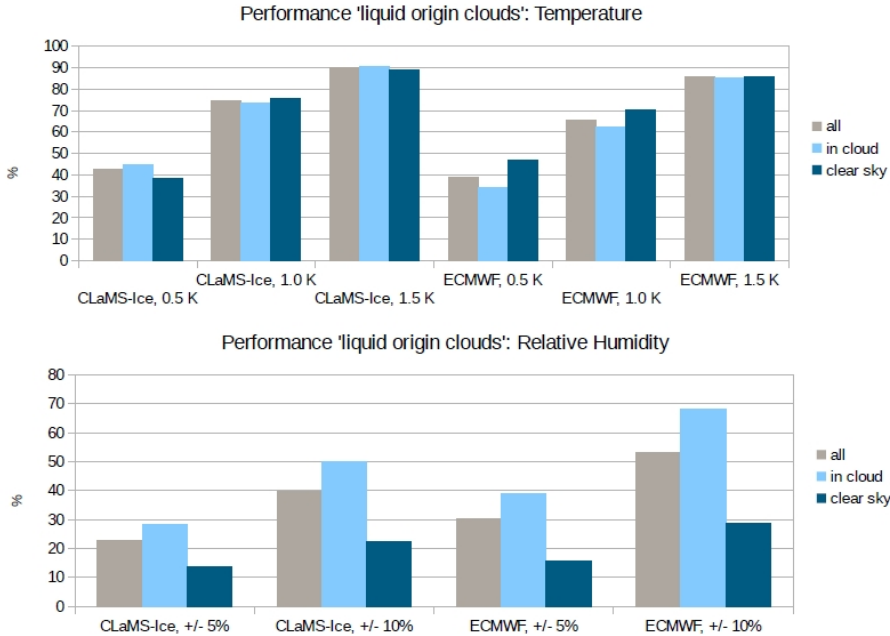


Figure 4.8: Agreement between CLaMS-Ice/ECMWF and observations as in Figure 4.5, but restricted to liquid origin clouds during ML-Cirrus. Top: Temperature comparison, bottom: RH_i comparison.

Cloud particle number concentrations (N_{ice}). The model performance regarding N_{ice} in in-situ cirrus is comparable to the IWC results. While the cloud cover is even slightly better (86%), only 13% of all values match the N_{ice} observations within two orders of magnitude. Only 9% get as close as one order of magnitude to the measurements.

4.4.4 Model performance, liquid origin cirrus

It is important to note that the label 'liquid origin' is only valid for trajectories based on ECMWF values, i.e. all trajectories labelled as 'liquid origin' carry cloud particles across the 238 K level to the flightpath. The measurements, however, show also here some cloud-free segments, where ECMWF wrongly predicted a cloud. The comparison is therefore still divided in 'in cloud' and 'clear sky'. These terms refer to actual clouds detected by NIXE-CAPS.

Temperature. The liquid origin in-cloud temperatures of CLaMS-Ice compare similar to the observations as the campaign average 45% (+/- 0.5 K), 74% (+/- 1 K), and 90% (+/- 1.5 K), as Figure 4.8 shows (top). The clear-sky temperatures compare significantly better except for

the 0.5 K criterion (38% (+/- 0.5 K)/76% (+/- 1 K)/89% (+/- 1.5 K)). The ECMWF values are comparable to the overall campaign results or slightly worse (34%/62%/85% in clouds, 47%/70%/86% in clear sky).

Relative Humidity (RH_i). In both CLaMS-Ice and ECMWF, the relative humidities match the observations better than in the general comparison (see Figure 4.8, bottom). This is not surprising, because liquid origin trajectories - by definition - always carry clouds; the range of possible RH_is is therefore not as large as in the in-situ case, as it will remain close to 100%.

Within clouds, 25% of all CLaMS-Ice values agree within +/- 5% with the observations, and 50% within +/- 10%. Outside clouds, these values decrease to 14% and 22%, respectively. The original ECMWF data show 39%/68% agreement within and 16%/29% agreement outside clouds.

Cloud ice water content (IWC). With 73%, the liquid origin category shows the lowest agreement between predicted and observed cloud cover in CLaMS-Ice. With 69%, ECMWF is still doing slightly worse. Regarding the IWCs, all liquid origin cloud comparisons show better results than the assessment of the whole campaign: CLaMS-Ice agrees in 54% of all cases within two orders of magnitude with the measurements, and in 43% of all cases within one order of magnitude. With 63% and 54%, respectively, ECMWF is still doing better.

Cloud particle number concentrations (N_{ice}). The number concentrations predicted by CLaMS-Ice lie in 25% of all cases within one order of magnitude from the observations, and in 45% of all cases within two orders of magnitude. With that, N_{ice} compares significantly worse to the observations than IWC.

In liquid-origin clouds, the CLaMS-Ice cloud particle concentrations are - by definition - influenced by pre-existing ice, i.e. ice, that already exists when the trajectory is initialized. Since ECMWF does not contain ice particle number concentrations, these values have to be computed based on the ECMWF IWC. CLaMS-Ice uses the formula by Boudala et al. (2002), who use a temperature-based parametrization to define expected ice particle sizes. With these assumed sizes, CLaMS-Ice calculates ice particle number concentrations.

This approach has large uncertainties. The Boudala et al. (2002) parametrization was made for high-latitude clouds in the mixed-phase temperature regime, not for mid-latitude cirrus. The temperature-radius relationship might be different for the types of clouds we probed here, which are largely associated with fronts and warm conveyor belts and contain many large particles. Another source of uncertainty is the number of IN that CLaMS-Ice uses for new cloud nucleations. In the version of CLaMS-Ice used here, the model allows the existence of IN even within liquid origin clouds, which might be unrealistic: Due to the formation of high concentrations of cloud particles in the mixed-phase temperature regime (cf. chapter 3), IN are probably fully used up before the air parcel reaches the cirrus cloud regime below 238 K.

4.5 Case Studies

In the previous sections, several possible sources for uncertainties in the simulations were mentioned. To examine their relative contribution, i.e. the model sensitivity to different input parameters, more closely, two case studies were performed. In subsection 4.5.1 and subsection 4.5.2, the influence of water input, sedimentation factor and initial IN concentrations is investigated. A third case study was performed to assess the representation of microphysical changes on small spatial scales in CLaMS-Ice.

4.5.1 Case I: Cold cirrus

The ML-Cirrus flight on 2014/04/15 was aimed at a high-altitude cirrus field at temperatures colder than 210 K, located over the Atlantic ocean west of Portugal. This cloud field looked homogeneous in the measurements (Figure 4.9), but backwards trajectory calculations show that it was formed in a convergence zone of two air mass flows with diametrically opposed origins (see Figure 4.10): One south-west flow went along the coast of west Africa before turning south-east and reaching the flightpath west of Portugal (classified as 'maritime air'), the second one passed France and Spain from north-east before turning south-east over Portugal (classified as 'continental air'). Both air masses show a similar dynamical history: During the last 24 hours before reaching the flightpath, all trajectories had pressure altitudes of 220 hPa and less, i.e. they remained in the upper troposphere/lower stratosphere.

The flight segment depicted in Figure 4.9 was chosen to perform a sensitivity study with CLaMS-Ice, aiming at the characterization of microphysical model input parameters. Due to their differing origin, we expect differing microphysical characteristics (humidity, IN concentration...) in the two air masses described above. To investigate the respective model sensitivities, CLaMS-Ice was initialized with systematic variations of the IN and water vapour input. Since the dynamics are comparable, we would expect similar model results for all set-ups, if the model is insensitive to the microphysical input. The results would, however, slightly vary randomly due to the small-scale temperature fluctuations that were superimposed on the trajectories.

The IN input is varied in 32 steps, equidistant on a logarithmic scale between 4 cm^{-3} and $3.2 \cdot 10^{-3} \text{ cm}^{-3}$. This choice covers a wider range of atmospheric conditions than observed so far. The lower input values represent the value where the model output matches the simulations without any IN; in this case, only homogeneous freezing of H_2SO_4 droplets is possible. The higher values exceed the IN measurements presented in DeMott et al. (2010), where 0.3 cm^{-3} was the highest reported IN concentration. They also exceed the IN concentrations used by Rolf et al. (2012) to simulate cirrus clouds formed in the outflow of the 2010 eruption of the Eyjafjallajökull volcano on Iceland. Since this was an event with a presumably above-average IN concentration over mid Europe, our range of IN settings should cover all plausible conditions during ML-Cirrus.

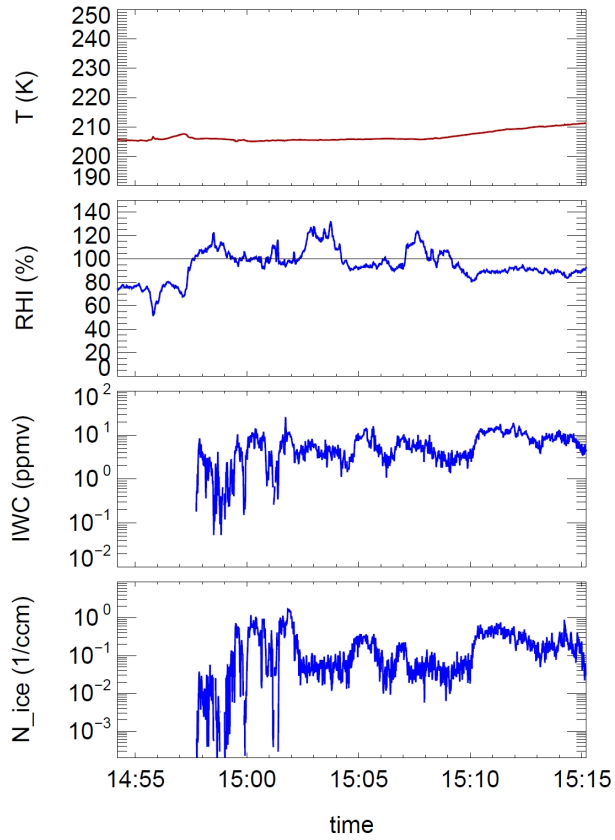


Figure 4.9: 20 Minutes of measurements by the HALO instrumentation during the entry of a cold cirrus field west of Portugal. From top to bottom: a) temperature, b) relative humidity, c) ice water content and d) ice particle number concentrations.

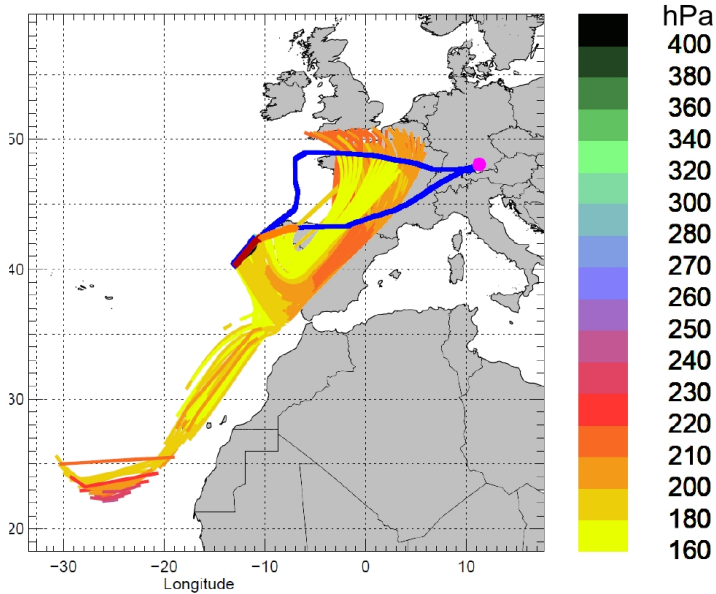


Figure 4.10: 'Cold cirrus' case study: The trajectories leading to the flightpath reveal that a bifurcation point was passed. Maritime trajectories from southwest meet continental trajectories from northeast. The color code denotes the pressure along the trajectory.

Each trajectory is initialized with a water vapour value taken from the ECMWF dataset. Kunz et al. (2014) have shown that in the upper troposphere, about 70% of the water vapour values in ECMWF deviate more than 10% (and up to a factor of 2) from in-situ measurements. It is important to assess the impact of this uncertainty on the model output. We thus use the original ECMWF water vapour values and vary them at the trajectory starting point by multiplying them with a 'water factor'. This factor ranges from 0.7 times the original value to 1.2 times the original value.

As described in subsection 4.4.2, the comparison between model and observations is based on 1 Hz measurements by the HALO instrumentation along the flightpath and one simulation result per minute of flight. The latter are interpolated to 1 Hz along the flightpath to match the observations. In the 'cold cirrus' case, this translates to 1200 single data points that can be compared. As a simple quality parameter for the agreement between CLaMS-Ice and observations, the median deviations are analyzed. Unlike mean values, they are robust against outliers, which can - in the case of IWC and N_{ice} - cover many orders of magnitude.

Continental air. In general, the model output for the 'continental air' trajectories of the flight does not seem to be sensitive to the water input: when the IN input into CLaMS-Ice is held constant, the deviation between model and observations does not vary greatly between model

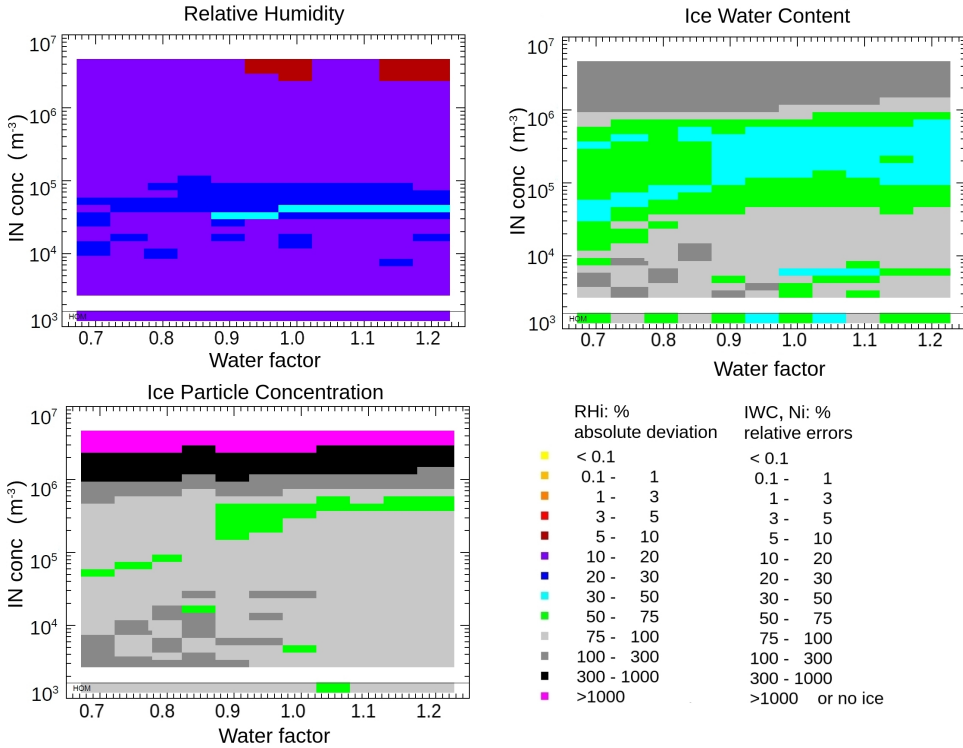


Figure 4.11: 'Continental air' trajectories. Top left: This graph shows the model's deviation from the observed values for 352 model runs with regard to the parameter RH. Each colored square depicts a model/observation comparison of 1100 data points (1 Hz observational data, 1 simulation result per minute interpolated to 1 Hz values). The deviation is given as absolute difference in the simulated and measured RH. The model runs below the horizontal line show the results for a purely homogeneous nucleation; in this case, the initial model concentration for IN is 0 cm^{-3} . Top right: Model deviation from the observed values for 352 model runs with regard to the parameter IWC. The deviation is given as relative error between the simulated and measured IWC. Bottom left: As top right, but for N_{ice} .

runs with an increase or decrease of the water factor (horizontal result pattern, see Figure 4.11 to Figure 4.11). The absolute deviations with regard to the relative humidity range from 5% to 50%, with most of the model runs reaching absolute deviations between 10% and 20%. For IWC and N_{ice} , relative errors are given, as the observed values cover several orders of magnitude. Here, the best model runs have median relative errors of 30% to 300% with respect to IWC and 50% to 1000% with respect to N_{ice} . As a reminder, relative errors up to two orders of magnitude can be seen as agreement due to measurement uncertainties (see subsection 4.4.2).

Only for very dry settings with water deficits of 15% and more compared to ECMWF, the simulations show a worse agreement to the observations than otherwise. The IN input, on the

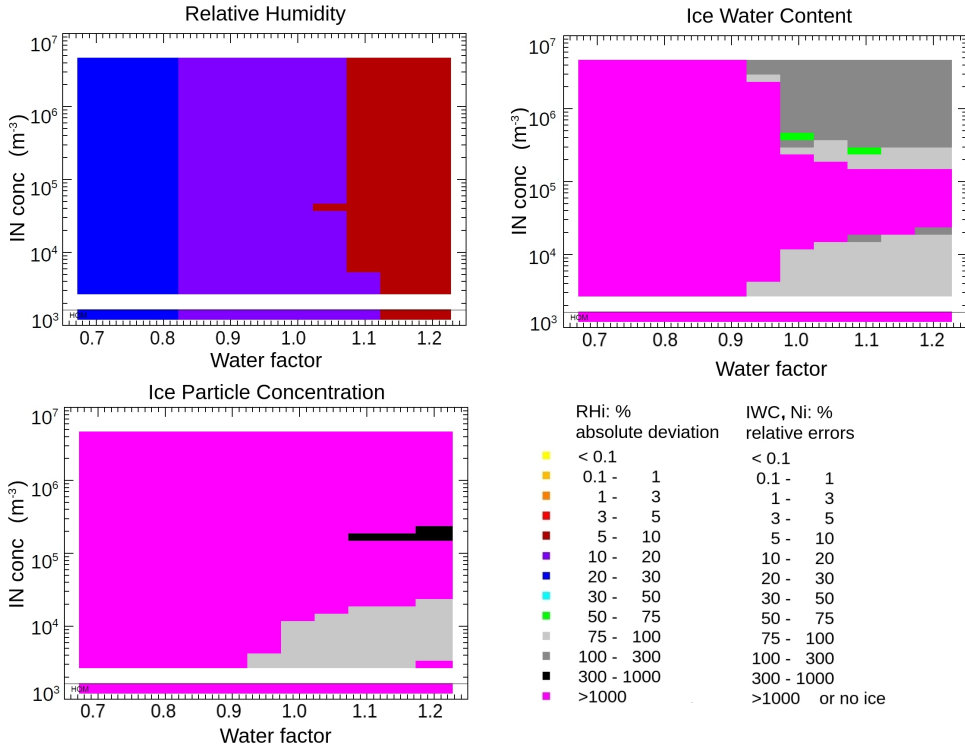


Figure 4.12: Model deviations from observed values. Like Figure 4.11, but for the maritime trajectories.

other hand, does influence the model performance significantly. Best agreements between model and observations are obtained for IN input concentrations around 0.1 cm^{-3} to 0.4 cm^{-3} ($10^{5.3}$ to $10^{5.6}/\text{m}^3$) and for an unchanged to slightly increased water input values. Only a small number of model runs (very high IN input) fails to simulate the cirrus clouds completely.

Overall, CLaMS-Ice is able to reproduce the observed microphysical characteristics of this cloud section well. These results suggest that the 'continental air' which produced cirrus clouds west of Portugal was rich in IN, which corresponds to 'polluted' conditions. The ECMWF water vapour initialization provided realistic results with a tolerance for slightly higher or lower values.

Maritime air. The simulations of the 'maritime air' section of the flight behaves differently (see Figure 4.12). Here, a decrease in the initial water vapour values inhibits the formation of clouds completely. Only model runs with a 'water factor' of 1.0 or higher produce clouds, and those runs only produce realistic IWCs and N_{ice} under two conditions: low IN input (0.016 cm^{-3} or lower, equalling $10^{4.2}/\text{m}^3$ or lower) or very high IN input (0.16 cm^{-3} or higher,

equalling $10^{5.2}/\text{m}^3$ or higher). The deviations between model and observational values are lower for the 'low IN' group, with relative errors of 75% to 100 % for both IWC and N_{ice} . For the 'high IN' runs, a small group of runs has relative errors of 300% to 1000% regarding N_{ice} (black group in Figure 4.12, bottom panel); the same group shows relative errors of 75% to 100% regarding IWC.

When the IN concentrations are set to higher values than 0.16 cm^{-3} , CLaMS-Ice produces clouds with IWCs that deviate between 100% to 300% from the observations, i.e. that still deviate less than two orders of magnitude from the measurements. The N_{ice} , however, deviate by more than 100%, i.e. more than two orders of magnitude, from the observations. This group of model runs can therefore not be considered to provide realistic results.

For water factors of 1.1 and higher, the simulated RH_i provides a very good agreement with the measurements. The absolute error remains between 5% and 10% for all chosen IN input values. In conclusion, the 'maritime air' segment of the flight can only be reproduced in the model if low IN values are chosen as an input. Since the backward trajectories have been over the sea for more than 24 hours, it is possible that they have not met a source of pollution for some time. The simulations indicate that in this case, the ECMWF water vapour input has to be modified to slightly higher values (10% to 20% more water vapour).

4.5.2 Case II: Sedimentation and high-pressure cirrus

HALO flight 03 probed high pressure cirrus clouds over Germany. Those consist of mostly heterogeneously nucleated particles, i.e. comparatively large ice particles. The associated simulations are therefore expected to be sensitive to changes in the 'sedimentation factor' input. The standard model setup uses a sedimentation factor of 0.9, as described in section 4.3. To assess the influence of this choice, the sedimentation factor is varied between 0.5 (strong sedimentation) and 1.0 (no sedimentation). Furthermore, the H₂O input is varied to account for the ECMWF uncertainties as mentioned in subsection 4.5.1.

Flight 03 is divided in sections referring to the probed cloud segment (cloud edge, top, middle). Fall streaks (virgae) made the lower part of the cirrus diffuse, so that the bottom can not be examined here. Figure 4.13 shows the comparison between simulations and observations for the parameters RH_i, IWC and N_{ice} for each of the segments.

The input parameters that produce the best simulation results vary between the cloud segments. This was to be expected, as Spichtinger and Cziczó (2010) have assigned different sedimentation factors to various cloud regions, taking into account that the lower an air parcel is within a cloud, the more sedimenting cloud particles it will receive from the top.

For all cloud regions, the microphysical parameters IWC and N_{ice} could be reproduced within the measurement uncertainties. With regard to the sedimentation factor, only weak or no sedimentation did not produce realistic IWCs and N_{ice} in CLaMS-Ice. The systematic variations of the model input parameters show that the results do not depend significantly on the applied

sedimentation factor, as long as

$$0.9 \leq \textit{sedimentation\ factor} \leq 0.98 \quad (4.1)$$

For this range of the sedimentation factor, the water vapour input plays a larger role than the sedimentation setting. At the same time, it is important to note that all water factors produce simulation results within the measurement uncertainties. Water inputs slightly lower than the ECMWF values give the best results; the optimal water factor varies between 0.8 and 0.9.

The relative humidity is only captured correctly in the middle of the cloud, where the least variations are expected. For both cloud edge and top, only a water factor of 0.8 produced IWC and N_{ice} in an acceptable agreement with the observations (less than one order of magnitude difference). For the cloud edge, an extraordinary closure of 5% is reached between CLaMS-Ice and observations with regard to the IWC, while N_{ice} shows higher, yet still acceptable deviations (median of relative error near 100%). Like often in the overall comparison in subsection 4.4.2, the RH_i shows here large deviations > 10%.

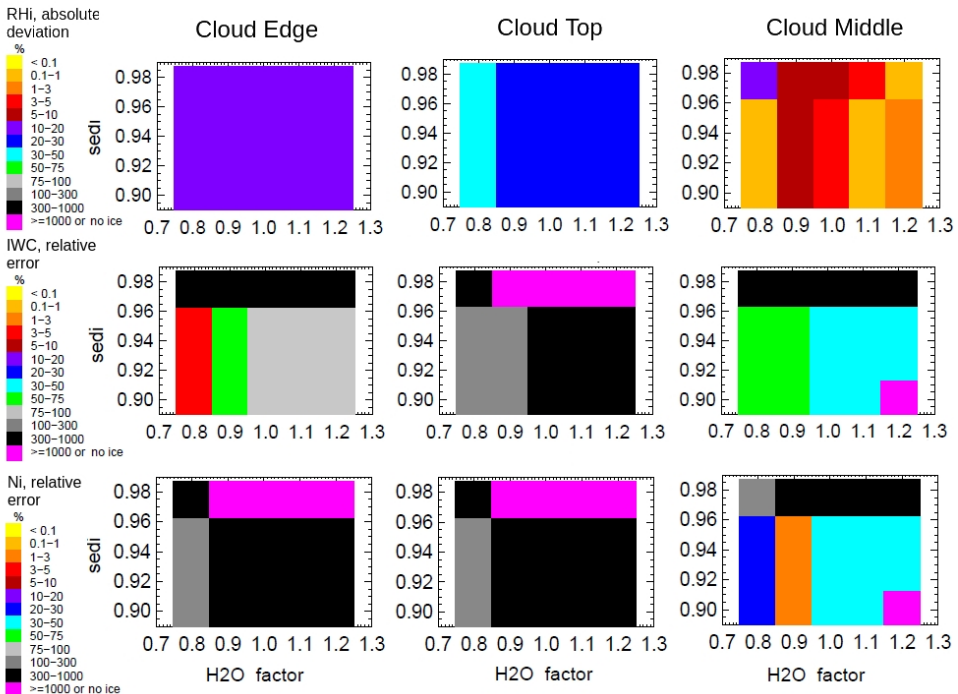


Figure 4.13: Case study II: The model input parameters that led to the best results are quite different for each respective cloud segment. The plot shows the cloud edge (left panels), top (middle panels) and cloud middle (right panels). The top row shows the results from the RH_i comparison, middle row: ice water content, bottom row: cloud particle concentrations.

With regard to the water input, another fact has to be taken into account: The probed region over Germany was contaminated with contrails and contrail-induced cirrus. This fact might also play a role in the simulated under- and overestimation of water vapour by ECMWF: in those cases where the observed cirrus cloud was initiated by a contrail in otherwise cloud-free air, the true water vapour value would not result in a simulated cloud, if CLaMS-Ice is correct. A decreased or increased water vapour value, however, causes a cirrus nucleation to happen at different points in time. These events then have a higher chance to occur in the area where the contrail cirrus was observed during the measurements.

In conclusion, this case study demonstrates that a sedimentation factor of 0.9 produces satisfying results for a wide range of cloud locations. The current CLaMS-Ice setup, where the cloud development along all trajectories is simulated independently, can therefore be trusted to provide robust results without varying the sedimentation setting. On the other hand, this case study shows again that the ECMWF water input has to be analyzed with care and possibly varied in order to reproduce the observed microphysical cloud characteristics in CLaMS-Ice.

4.5.3 Case III: Warm conveyor belt: microphysical separation and outflow characteristics

Flight 06 probed a warm conveyor belt (WCB) associated with a low over the Mediterranean sea (see Figure 4.14, upper left panel). The WCB reached the cirrus cloud level near Corsica; HALO crossed this region at varying altitudes. For the second part of the flight, the WCB's outflow was probed in some distance of the ascent region: over southern Germany and the Alps (see Figure 4.14, lower left panel).

In the first flight part within the WCB, the observations show two distinctively different cloud groups, one with fewer particles consisting of smaller and more pristine ice crystals (Figure 4.15, top), and the second with many and large particles, mostly aggregates (Figure 4.15, bottom). When the aircraft changed the flight level from the largest altitude within the cloud to lower levels, a transition between the two groups is visible in the CIP images (Figure 4.15, middle panels). Also, a comparison of the cloud particle size distributions and number concentrations reveals differences between the two groups:

The first probed cloud section (before 12.45 UTC, marked as 12.75 in Figure Figure 4.16) contains predominantly small ice crystals with highly variable number concentrations. Backward trajectories (see top left in Figure 4.14) show that this cirrus layer does not originate in lower regions of the atmosphere like the lower clouds. The air parcels in which the cirrus has formed were transported horizontally from a Western direction and were lifted in the vicinity of the WCB due to the vertical air movement below.

In the following flight legs at lower altitude (after 12.45 UTC), where more large agglomerates and rosettas were observed, the backward trajectories show that these cloud particles have formed under 'liquid origin' conditions. They might have grown due to the Wegener-Bergeron-Findeisen process, which would explain the large particle sizes (compare section 3.1).

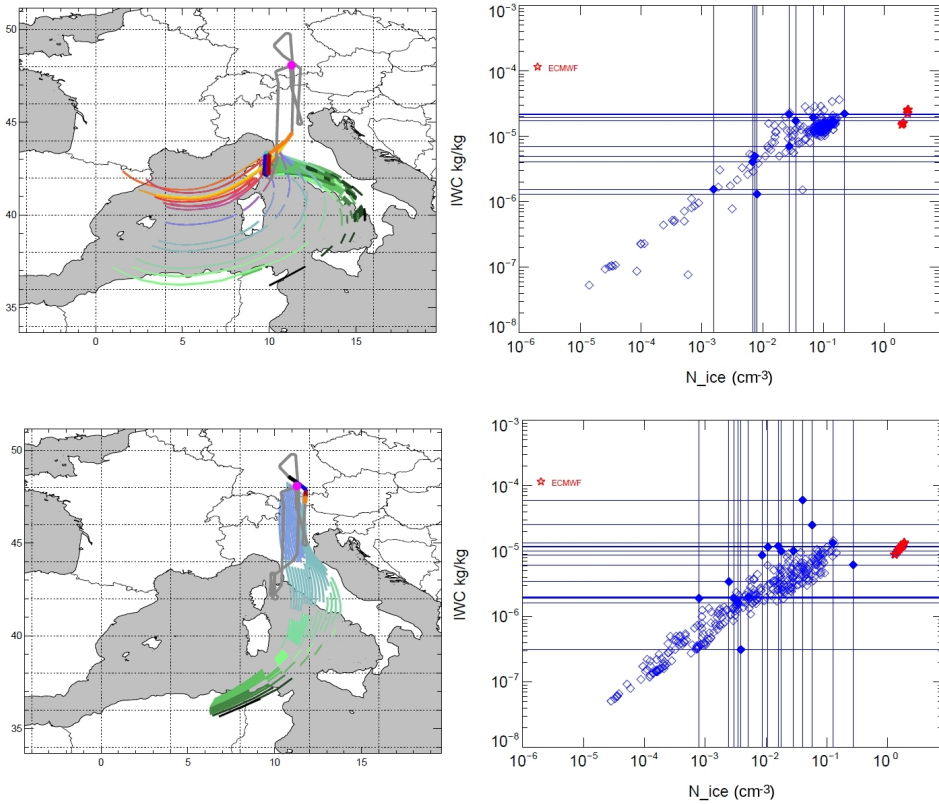


Figure 4.14: Two segments of flight 06 of ML-Cirrus, on the 27th of March 2014. The left panels show CLaMS trajectories leading to two chosen flightpath segments: One close to the ascent region of the warm conveyor belt (top), the other in the warm conveyor belt's outflow regions over the Alps (bottom). (Color code: pressure along trajectory as in Figure 4.10. Grey line: flightpath.) The solid blue diamonds in the panels on the right show cloud particle number concentrations (N_{ice}) and ice water contents (IWC) measured by NIXE-CAPS in these segments. Blue lines show the location of these values to indicate the range of the observations on the axes. The empty diamonds show the CLaMS-Ice simulation results. The red stars show the IWC that ECMWF predicts. The respective N_{ice} are calculated using the Boudala et al. (2002) parametrization.

Corresponding to this, a curtain through the Corsica area (see Figure 4.17) shows that the lower probed cloud region is connected to the a cloud layer with a large vertical extension reaching down below 400 hPa. Above the massive cloud layer, a less homogeneous layer has formed which is partially disconnected from the lower part.

In the second part of the flight, the WCB outflow over the Alps and its evaporation region over southern Germany were probed. The trajectories show that these clouds originated in the WCB (see lower left panel in Figure 4.14) and could therefore be classified as liquid origin clouds.

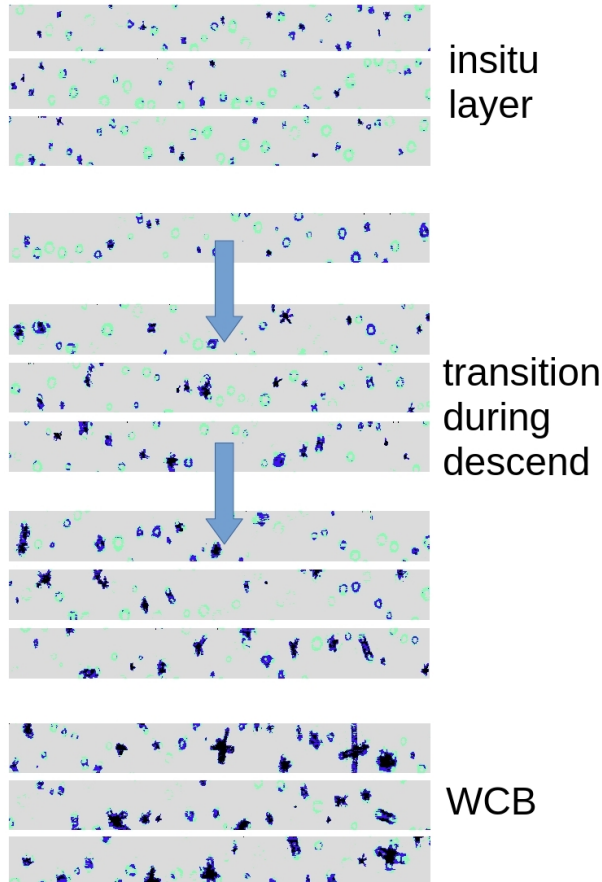


Figure 4.15: Top: CIP images recorded within the cirrus cloud layer at the higher altitude above the liquid origin clouds (compare Figure 4.17). Middle panels: As the aircraft descends into the liquid origin cloud region, a shift in the particle habits towards larger diameters and more complex shapes can be observed. Bottom: Within the liquid origin clouds, large rosettas and aggregates are recorded by the CIP.

However, they do not show the microphysical characteristics associated with those clouds in Luebke et al. (2016), as it can be seen in Figure 4.14 (lower right panel): with average ice crystal concentrations of 0.01 cm^{-3} , they are more similar to insitu cirrus. The characteristics for liquid origin cirrus clouds (high cloud particle number concentrations, larger ice water contents) are only found in clouds closer to the main ascent area of the WCB (see upper panels in Figure 4.14). The two cloud sections show distinctly different microphysical signatures in CLaMS-Ice, in line with the observations. As the right panels of Figure 4.14 show, this microphysical differentiation would not be possible with ECMWF IWC data (red stars) alone.

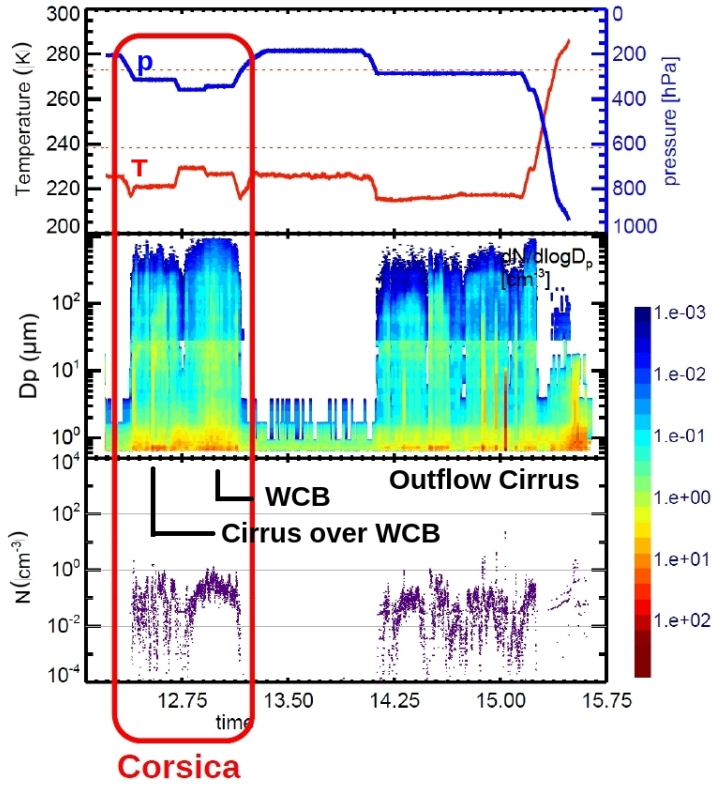


Figure 4.16: The region near Corsica was probed for about 40 minutes during flight 06 of ML-Cirrus. The measurements are divided into two parts that are different with regard to the cloud particle number concentration's variability (lowest panel) and the cloud particle size range (middle panel).

It can be assumed that the transport from the ascending part of the WCB to the probed region above the Alps took enough time for the large particles to sediment out of those clouds. The remaining cloud is microphysically comparable to an in-situ formed cirrus following Luebke et al. (2016).

The strong transformation of the cirrus' microphysical properties along the liquid origin trajectories shows the difficulty of drawing conclusions on the microphysical appearance of a cirrus cloud based on the air mass origin alone, as suggested by Wernli et al. (2016). When cirrus cloud studies are aimed at estimating the cirrus clouds' radiative impact, a microphysical model such as CLaMS-Ice has to be employed to determine the characteristics of the resulting clouds.

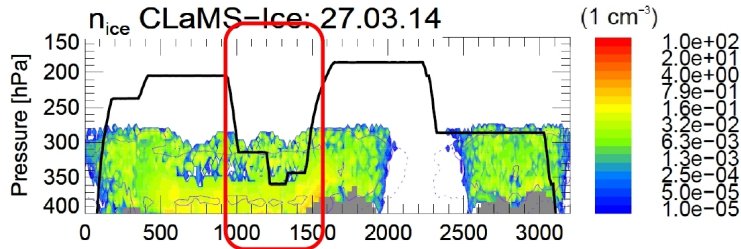


Figure 4.17: CLaMS-Ice simulation results for a curtain from 400 to 200 hPa along the flight-path. The x-axis shows kilometers of flight. The section between kilometers 1000 and 1500 clearly shows the increased variability of cirrus cloud ice particle concentrations compared to the WCB below. For N_{ice} observations along the flightpath see Figure 4.16.

4.6 CLaMS-Ice simulations - Summary

CLaMS-Ice has provided satisfying results with regard to the cirrus cloud cover and the overall microphysical properties over Europe. More precisely, initialization with average values produces a satisfying climatological agreement between simulations and observations in the ice water content/temperature parameter space (Rolf et al., 2015). This suggests that if the spatial scales of a simulation are large enough, local IN and water vapour variations that are not captured by the ECMWF input data might cancel out. Apart from the importance for climatological studies, this is also noteworthy for the use of CLaMS-Ice as a forecast tool e.g. for flight planning of cirrus cloud campaigns.

On the other hand, the simulation results in the case studies presented here were proven to be sensitive to these microphysical input parameters, which are not available from external data sources for the model initialization. The 'cold cirrus' case has shown how variable cirrus clouds can be on small spatial scales: in addition to reproducing the correct mean characteristics of a cloud, the simulation of inhomogeneity is another challenge for cirrus cloud modelling. As a second result, the 'cold cirrus' case has demonstrated that two groups of trajectories with differing source regions showed different sensitivity to the input parameters IN number concentration and water vapour input. Climatological studies that aim for the average state of the atmosphere can yield satisfying results without these variations, but for localized simulations, e.g. for flight planning purposes, the potential influence of the input parameter variability has to be taken into account.

Also, in case study II (high pressure cirrus), CLaMS-Ice is to a limited extent sensitive to assumptions about the sedimentation factor, which might depend on the position of the modelled air parcel within the cloud layer (top, middle, bottom). The setting suggested by Spichtinger and Cziczo (2010) for the middle region of the cloud, however, does produce acceptable agreements between observations and simulations. This holds true for all examined cloud regions. A 3D

version of CLaMS-Ice is planned, in which cloud particles sedimenting out of one trajectory are received by the trajectory below. Case study II suggests, however, that the simplified version of CLaMS-Ice used here can also provide good results, as long as the water vapour input is realistic. The problem of an unknown percentage of contrail cirrus in the observations remains unsolved and produces a deviation between model and observations that cannot be quantified at this point.

The third case study investigated the microphysical characteristics of cirrus clouds connected to the center of a warm conveyor belt, within its outflow and in a partially disconnected layer above the ascent region. Both observations and CLaMS-Ice simulations show large differences between these regions. Interestingly, the cirrus cloud in the outflow region is microphysically similar to insitu cirrus clouds, even though the trajectory alone would suggest a liquid origin cloud. The case study proves the importance of a correct microphysical representation of cirrus cloud processes such as sedimentation in the model, which can strongly alter the cloud's characteristics. This is especially important when the results are used for irradiation simulations. The air mass origin alone and statistical characteristics of in-situ and liquid origin cirrus clouds will lead to imprecise assumptions with regard to ice particle number concentrations and ice water contents, as long as changes in the microphysical appearance of the cloud due to sedimentation and additional nucleation events are not considered.

With regard to the uncertainties of the observations, an observation/simulation agreement within one to two orders of magnitude can be seen as a success. An additional factor of uncertainty is the strong dependence of the model results on the spatially coarse and occasionally imprecise ECMWF input data fields. With respect to such uncertainties, CLaMS-Ice produces promising results. Nevertheless, the micro-physical characterization of the modelled clouds could be improved when judged by the direct, second-to-second comparison between simulation and observations. CLaMS-Ice is thus currently refined and will be compared to the observations again in the future (see next section).

4.7 Outlook - future work on CLaMS-Ice

The latest version of CLaMS-Ice has two updated schemes, which were motivated by the detailed insitu/model comparison in this study: One for the IWC/ice crystal number concentration relation and the second for the IN input. In the model version used for the studies presented here, the Boudala et al. (2002) parameterization was used to define ice particle number concentrations depending on the IWC and temperature input. With this approach, particle diameters were calculated and compared to those observed by NIXE-CAPS during ML-Cirrus. The Boudala parameterization was established for Arctic clouds and can therefore be expected to deviate from the cloud characteristics in the mid-latitudes. The new CLaMS-Ice model therefore uses a IWC/particle number concentration relationship that is based on the NIXE-CAPS measurements during ML-Cirrus; this yields better agreement between model and observations. Regarding

the IN input, the old CLaMS-Ice version used a fixed number concentration for IN particles that had to be defined in the input file. The new version will use the input concentration as the mean of a lognormal IN concentration distribution. This approach acknowledges that the IN concentrations can vary on short spatial scales.

In the near future, the comparison described above will be repeated using this updated model version to determine where and to what extent the new, more precise parametrizations have improved the agreement between simulations and observations. Also, to fully capture the range and variability of the microphysical parameters in cirrus clouds, the model simulations will be done with a higher resolution along the flightpath, e.g. using one trajectory per second of flight. This will allow to compare not only median values of the agreement, but also to capture the cloud variability and thus inhomogeneity. With that, CLaMS-Ice will provide another microphysical attribute of cirrus clouds that is not available in current modelling products.

5 Thesis summary and outlook

With the cloud spectrometer NIXE-CAPS, detailed microphysical observations of cloud particle properties were obtained at temperatures between 0°C and -70°C : cloud particle concentrations, size distributions and shape information were collected. Observations of small particle shapes below $50\ \mu\text{m}$ constitute an innovation for in-situ cloud probes. Therefore, the respective NIXE-CAPS detector was validated in a comparison with the PPD-2K instrument at the AIDA cloud chamber in Karlsruhe prior to the analysis of the conducted field experiments. In the course of the instrument checks, the NIXE-CAPS software library NIXElib was accelerated and extended by corrections for electronic noise and erroneous single particle measurements.

One scientific focus of this work was the mixed-phase temperature regime (0°C to -38°C), where both supercooled liquid and frozen cloud particles can exist. Here, the analysis of the backscattered light of small cloud particles (with diameters below $50\ \mu\text{m}$) was proven to be valuable, as this technique allows a new approach at the detection of microphysical cloud processes: ice multiplication, the Wegener-Bergeron-Findeisen process and also simultaneous growth of both liquid and ice particles in high updrafts strongly affect the population of small cloud particles, while large cloud particles usually contain the glaciated fraction of the cloud. The proportions of clouds affected by the mentioned processes was determined in Arctic, mid-latitude and tropical measurements, which showed considerable differences in the occurrence of the associated cloud types. The Arctic measurements with weak atmospheric dynamics contained a high percentage of fully liquid clouds, which might also be a result of a lack of biological particles acting as ice nuclei in the probed region. In the mid-latitudes, the Wegener-Bergeron-Findeisen process leads to a quick glaciation at temperatures below -20°C , hinting at mineral dust as the predominant ice nuclei type. Biological particles are, however, likely to influence the clouds as well, because smaller fractions of the probed clouds already contain ice at temperatures warmer than -20°C . The tropical convective clouds, which are associated with strong vertical winds, were found to contain spherical, i.e. potentially liquid, particles down to very cold temperatures near the homogeneous freezing threshold. At the same time, throughout the probed temperature range, large ice particles were found, which might stem from the Wegener-Bergeron-Findeisen process or might have sedimented from the cumulonimbus anvils. This cloud classification can be applied to further observations in the future, thus creating a larger database on the global occurrence of the different cloud types.

In the cirrus cloud regime at temperatures below -38°C , the NIXE-CAPS data were used to evaluate the performance of the new ice cloud model CLaMS-Ice, a two-moment bulk model

aimed at simulating the microphysical properties of cirrus clouds on large spatial scales. In detailed case studies, the model was able to simulate the observed cirrus clouds, given that the input parameters are adjusted to the respective conditions. While the overall comparison of the CLaMS-Ice simulations with the observed clouds was also promising, it was shown that a higher trajectory density is required to capture the full characteristics of the cirrus clouds when studied on small spatial scales, e.g. at the flightpath. These characteristics include small-scale inhomogeneities of microphysical parameters such as ice particle concentrations, which can span over several orders of magnitude. The resolution chosen during this study was not high enough to provide these characteristics, resulting in locally unsatisfactory comparisons between NIXE-CAPS observations and CLaMS-Ice simulations. Nevertheless, the comparison led to improvements in CLaMS-Ice: the model time step variation was adapted to meet the required precision, and a parametrization for the size distributions of ice originating in warmer atmospheric regions was found. These modifications in combination with a higher trajectory density will lead to a more realistic representation of cirrus clouds in CLaMS-Ice.

Bibliography

- Augustin-Bauditz, S., Wex, H., Kanter, S., Ebert, M., Niedermeier, D., Stolz, F., Prager, A., and Stratmann, F.: The immersion mode ice nucleation behavior of mineral dusts: A comparison of different pure and surface modified dusts, *Geophysical Research Letters*, 41, 7375–7382, 2014.
- Barthelmebs, A.: Der Strahlungseffekt von Eiswolken in den mittleren Breiten, Master's thesis, Johannes Gutenberg Universitaet Mainz, Germany, 2015.
- Baumgardner, D., Jonsson, H., Dawson, W., O'Connor, D., and Newton, R.: The cloud, aerosol and precipitation spectrometer: a new instrument for cloud investigations, *Atmospheric Research*, 59–60, 251 – 264, doi:[http://dx.doi.org/10.1016/S0169-8095\(01\)00119-3](http://dx.doi.org/10.1016/S0169-8095(01)00119-3), URL <http://www.sciencedirect.com/science/article/pii/S0169809501001193>, 13th International Conference on Clouds and Precipitation, 2001.
- Baumgardner, D., Newton, R., Krämer, M., Meyer, J., Beyer, A., Wendisch, M., and Vochezer, P.: The Cloud Particle Spectrometer with Polarization Detection (CPSPD): A next generation open-path cloud probe for distinguishing liquid cloud droplets from ice crystals, *Atmospheric Research*, 142, 2 – 14, doi:<http://dx.doi.org/10.1016/j.atmosres.2013.12.010>, URL <http://www.sciencedirect.com/science/article/pii/S0169809513003591>, the 16th International Conference on Clouds and Precipitation, 2014.
- Boucher, O., Randall, D., Artaxo, P., Bretherton, C., Feingold, G., Forster, P., Kerminen, V.-M., Kondo, Y., Liao, H., Lohmann, U., Rasch, P., Satheesh, S. K., Sherwood, S., Stevens, B., and Zhang, X. Y.: Clouds and Aerosols, *Climate Change 2013: The Physical Science Basis. Contribution of Working Group I to the Fifth Assessment Report of the Intergovernmental Panel on Climate Change* [Stocker, T.F., D. Qin, G.-K. Plattner, M. Tignor, S.K. Allen, J. Boschung, A. Nauels, Y. Xia, V. Bex and P.M. Midgley (eds.)], URL <https://www.ipcc.ch/report/ar5/>, cambridge University Press, Cambridge, United Kingdom and New York, NY, USA, 2013.
- Boudala, F. S., Isaac, G. A., Fu, Q., and Cober, S. G.: Parameterization of effective ice particle size for high-latitude clouds, *International journal of climatology*, 22, 1267–1284, 2002.
- Bühl, J., Ansmann, A., Seifert, P., Baars, H., and Engelmann, R.: Toward a quantitative charac-

- terization of heterogeneous ice formation with lidar/radar: Comparison of CALIPSO/CloudSat with ground-based observations, *Geophysical Research Letters*, 40, 4404–4408, 2013.
- Bunz, H., Benz, S., Gensch, I., and Krämer, M.: MAID: a model to simulate UT/LS aerosols and ice clouds, *Environmental research letters*, 3, 035 001, 2008.
- Cecchini, M. A., Machado, L. A. T., Wendisch, M., Costa, A., Krämer, M., Andreae, M. O., Afchine, A., Albrecht, R. I., Artaxo, P., Borrmann, S., Fütterer, D., Klimach, T., Mahnke, C., Martin, S. T., Minikin, A., Molleker, S., Pardo, L. H., Pöhlker, C., Pöhlker, M. L., Pöschl, U., Rosenfeld, D., and Weinzierl, B.: Illustration of microphysical processes of Amazonian deep convective clouds in the Gamma phase space: Introduction and potential applications, 2017.
- Costa, A., Meyer, J., Afchine, A., Luebke, A., Günther, G., Dorsey, J. R., Gallagher, M. W., Ehrlich, A., Wendisch, M., Baumgardner, D., Wex, H., and Krämer, M.: Classification of Arctic, midlatitude and tropical clouds in the mixed-phase temperature regime, *Atmospheric Chemistry and Physics*, 17, 12 219–12 238, doi:10.5194/acp-17-12219-2017, URL <https://www.atmos-chem-phys.net/17/12219/2017/>, 2017.
- DeMott, P. J., Prenni, A. J., Liu, X., Kreidenweis, S. M., Petters, M. D., Twohy, C. H., Richardson, M. S., Eidhammer, T., and Rogers, D. C.: Predicting global atmospheric ice nuclei distributions and their impacts on climate, *Proceedings of the National Academy of Sciences*, 107, 11 217–11 222, doi:10.1073/pnas.0910818107, URL <http://www.pnas.org/content/107/25/11217.abstract>, 2010.
- DMT: CAPS User Manual - Chapter I: Single Particle Light Scattering, Boulder, Colorado, droplet Measurement Technologies, 2009.
- Ehrlich, A.: The impact of ice crystals on radiative forcing and remote sensing of arctic boundary-layer mixed-phase clouds, Ph.D. thesis, Ph. D. thesis, Johannes Gutenberg University Mainz, Germany, 2009.
- Erfani, E. and Mitchell, D. L.: Developing and bounding ice particle mass- and area-dimension expressions for use in atmospheric models and remote sensing, *Atmospheric Chemistry and Physics*, 16, 4379–4400, doi:10.5194/acp-16-4379-2016, URL <http://www.atmos-chem-phys.net/16/4379/2016/>, 2016.
- Field, P. R., Heymsfield, A. J., and Bansemmer, A.: Shattering and Particle Interarrival Times Measured by Optical Array Probes in Ice Clouds, *Journal of Atmospheric and Oceanic Technology*, 23, 1357–1371, doi:10.1175/JTECH1922.1, URL <http://dx.doi.org/10.1175/JTECH1922.1>, 2006.
- Field, P. R., Lawson, R. P., Brown, P. R. A., Lloyd, G., Westbrook, C., Moisseev, D., Miltenberger, A., Nenes, A., Blyth, A., Choulaton, T., Connolly, P., Buehl, J., Crosier,

- J., Cui, Z., Dearden, C., DeMott, P., Flossmann, A., Heymsfield, A., Huang, Y., Kalesse, H., Kanji, Z. A., Korolev, A., Kirchgaessner, A., Lasher-Trapp, S., Leisner, T., McFarquhar, G., Phillips, V., Stith, J., and Sullivan, S.: Chapter 7. Secondary Ice Production - current state of the science and recommendations for the future, *Meteorological Monographs*, 0, null, doi:10.1175/AMSMONOGRAPHS-D-16-0014.1, URL <http://dx.doi.org/10.1175/AMSMONOGRAPHS-D-16-0014.1>, 2015.
- Findeisen, W., Volken, E., Giesche, A. M., and Brönnimann, S.: Colloidal meteorological processes in the formation of precipitation, *Meteorologische Zeitschrift*, 24, 443–454, doi:10.1127/metz/2015/0675, URL <http://dx.doi.org/10.1127/metz/2015/0675>, 2015.
- Frisinger, H.: *The History of Meteorology: To 1800*, Historical monograph series American meteorological society, Science History Publications, URL <https://books.google.de/books?id=CYTuAAAAIAAJ>, 1977.
- Gary, B. L.: Mesoscale temperature fluctuations in the stratosphere, *Atmospheric Chemistry and Physics*, 6, 4577–4589, 2006.
- Hallett, J. and Mossop, C.: Production of secondary ice particles during the riming process, *Nature*, 249, 26–28, 1974.
- Heymsfield, A. J. and Parrish, J. L.: A Computational Technique for Increasing the Effective Sampling Volume of the PMS Two-Dimensional Particle Size Spectrometer, *Journal of Applied Meteorology*, 17, 1566–1572, doi:10.1175/1520-0450(1978)017<1566:ACTFIT>2.0.CO;2, URL [http://dx.doi.org/10.1175/1520-0450\(1978\)017<1566:ACTFIT>2.0.CO;2](http://dx.doi.org/10.1175/1520-0450(1978)017<1566:ACTFIT>2.0.CO;2), 1978.
- Jäkel, E., Wendisch, M., Krisna, T. C., Ewald, F., Kölling, T., Jurkat, T., Voigt, C., Cecchini, M. A., Machado, L. A. T., Afchine, A., Costa, A., Krämer, M., Andreae, M. O., Pöschl, U., Rosenfeld, D., and Yuan, T.: Vertical distribution of the phase state of particles in tropical deep-convective clouds as derived from cloud-side reflected solar radiation measurements, *Atmospheric Chemistry and Physics Discussions*, 2017, 1–30, doi:10.5194/acp-2017-64, URL <http://www.atmos-chem-phys-discuss.net/acp-2017-64/>, 2017.
- Järvinen, E., Schnaiter, M., Mioche, G., Jourdan, O., Shcherbakov, V. N., Costa, A., Afchine, A., Krämer, M., Heidelberg, F., Jurkat, T., Voigt, C., Schlager, H., Nishman, L., Gallagher, M., Hirst, E., Schmitt, C., Bansemmer, A., Heymsfield, A., Lawson, P., Tricoli, U., Pfeilsticker, K., Vochezer, P., Möhler, O., and Leisner, T.: Quasi-spherical Ice in Convective Clouds, *Journal of the Atmospheric Sciences*, 0, null, doi:10.1175/JAS-D-15-0365.1, URL <http://dx.doi.org/10.1175/JAS-D-15-0365.1>, 2016.
- Kanji, Z., Ladino, L. A., Wex, H., Boose, Y., Burkert-Kohn, M., Cziczo, D. J., and Krämer, M.: Ice Formation and Evolution in Clouds and Precipitation: Measurement and Modeling

- Challenges, Chapter 1: Overview of Ice Nucleating Particles, Meteorological Monograph, 2017.
- Kienast-Sjögren, E., Miltenberger, A. K., Luo, B. P., and Peter, T.: Sensitivities of Lagrangian modelling of mid-latitude cirrus clouds to trajectory data quality, *Atmospheric Chemistry and Physics*, 15, 7429–7447, doi:10.5194/acp-15-7429-2015, URL <http://www.atmos-chem-phys.net/15/7429/2015/>, 2015.
- Kienast-Sjögren, E., Rolf, C., Seifert, P., Krieger, U. K., Luo, B. P., Krämer, M., and Peter, T.: Climatological and radiative properties of midlatitude cirrus clouds derived by automatic evaluation of lidar measurements, *Atmospheric Chemistry and Physics*, 16, 7605–7621, doi:10.5194/acp-16-7605-2016, URL <http://www.atmos-chem-phys.net/16/7605/2016/>, 2016.
- Kienast-Sjögren, E. A.: Mid-latitude cirrus properties derived from lidar measurements, Ph.D. thesis, Dissertation, ETH-Zürich, 2015, Nr. 22492, 2015.
- Klingebiel, M., de Lozar, A., Molleker, S., Weigel, R., Roth, A., Schmidt, L., Meyer, J., Ehrlich, A., Neuber, R., Wendisch, M., and Borrmann, S.: Arctic low-level boundary layer clouds: in situ measurements and simulations of mono- and bimodal supercooled droplet size distributions at the top layer of liquid phase clouds, *Atmospheric Chemistry and Physics*, 15, 617–631, doi:10.5194/acp-15-617-2015, URL <http://www.atmos-chem-phys.net/15/617/2015/>, 2015.
- Konopka, P., Steinhorst, H.-M., Groöß, J.-U., Günther, G., Müller, R., Elkins, J. W., Jost, H.-J., Richard, E., Schmidt, U., Toon, G., et al.: Mixing and ozone loss in the 1999–2000 Arctic vortex: Simulations with the three-dimensional Chemical Lagrangian Model of the Stratosphere (CLaMS), *Journal of Geophysical Research: Atmospheres*, 109, 2004.
- Konopka, P., Günther, G., Müller, R., Dos Santos, F., Schiller, C., Ravegnani, F., Ulanovsky, A., Schlager, H., Volk, C., Viciani, S., et al.: Contribution of mixing to upward transport across the tropical tropopause layer (TTL), *Atmospheric Chemistry and Physics*, 7, 3285–3308, 2007.
- Koop, T., Luo, B., Tsias, A., and Peter, T.: Water activity as the determinant for homogeneous ice nucleation in aqueous solutions, *Nature*, 406, 611–614, 2000.
- Korolev, A.: Limitations of the Wegener–Bergeron–Findeisen Mechanism in the Evolution of Mixed-Phase Clouds, *Journal of the Atmospheric Sciences*, 64, 3372–3375, doi:10.1175/JAS4035.1, URL <http://dx.doi.org/10.1175/JAS4035.1>, 2007a.
- Korolev, A.: Reconstruction of the Sizes of Spherical Particles from Their Shadow Images. Part I: Theoretical Considerations, *Journal of Atmospheric and Oceanic Technology*, 24, 376–389, doi:10.1175/JTECH1980.1, URL <http://dx.doi.org/10.1175/JTECH1980.1>, 2007b.
- Korolev, A. and Sussman, B.: A Technique for Habit Classification of Cloud Particles, *Journal of Atmospheric and Oceanic Technology*, 17, 1048–1057, doi:10.1175/1520-0426(2000)017<1048:

- ATFHCO>2.0.CO;2, URL [http://dx.doi.org/10.1175/1520-0426\(2000\)017<1048:ATFHCO>2.0.CO;2](http://dx.doi.org/10.1175/1520-0426(2000)017<1048:ATFHCO>2.0.CO;2), 2000.
- Korolev, A., Emery, E., Strapp, J., Cober, S., Isaac, G., Wasey, M., and Marcotte, D.: Small ice particles in tropospheric clouds: Fact or artifact? Airborne Icing Instrumentation Evaluation Experiment, *Bulletin of the American Meteorological Society*, 92, 967–973, 2011.
- Korolev, A., Emery, E., and Creelman, K.: Modification and Tests of Particle Probe Tips to Mitigate Effects of Ice Shattering, *Journal of Atmospheric and Oceanic Technology*, 30, 690–708, doi:10.1175/JTECH-D-12-00142.1, URL <http://dx.doi.org/10.1175/JTECH-D-12-00142.1>, 2013.
- Krämer, M., Schiller, C., Afchine, A., Bauer, R., Gensch, I., Mangold, A., Schlicht, S., Spelten, N., Sitnikov, N., Borrmann, S., de Reus, M., and Spichtinger, P.: Ice supersaturations and cirrus cloud crystal numbers, *Atmospheric Chemistry and Physics*, 9, 3505–3522, doi:10.5194/acp-9-3505-2009, URL <http://www.atmos-chem-phys.net/9/3505/2009/>, 2009.
- Krämer, M., Afchine, A., Avallone, L., Baumgardner, D., Borrmann, S., Buchholz, B., Costa, A., Ebert, V., Fahey, D., Grooss, J.-U., Herman, R., Jensen, E., Klingebiel, M., Lawson, P., Luebke, A., Meyer, J., Riese, M., Rolf, C., Rollins, A., Smith, J., Spelten, N., Thornberry, T., Woods, S., and Zöger, M.: Cirrus Clouds and H₂O between 75 N and 25 S derived from extensive airborne in-situ observations, 2016a.
- Krämer, M., Rolf, C., Luebke, A., Afchine, A., Spelten, N., Costa, A., Meyer, J., Zoeger, M., Smith, J., Herman, R. L., Buchholz, B., Ebert, V., Baumgardner, D., Borrmann, S., Klingebiel, M., and Avallone, L.: A microphysics guide to cirrus clouds - Part 1: Cirrus types, *Atmospheric Chemistry and Physics*, 16, 3463–3483, doi:10.5194/acp-16-3463-2016, URL <http://www.atmos-chem-phys.net/16/3463/2016/>, 2016b.
- Kunz, A., Spelten, N., Konopka, P., Müller, R., Forbes, R., and Wernli, H.: Comparison of Fast In situ Stratospheric Hygrometer (FISH) measurements of water vapor in the upper troposphere and lower stratosphere (UTLS) with ECMWF (re) analysis data, *Atmospheric chemistry and physics*, 14, 10 803–10 822, 2014.
- Lamquin, N., Gierens, K., Stubenrauch, C. J., and Chatterjee, R.: Evaluation of upper tropospheric humidity forecasts from ECMWF using AIRS and CALIPSO data, *Atmospheric Chemistry and Physics*, 9, 1779–1793, doi:10.5194/acp-9-1779-2009, URL <http://www.atmos-chem-phys.net/9/1779/2009/>, 2009.
- Lance, S.: Coincidence Errors in a Cloud Droplet Probe (CDP) and a Cloud and Aerosol Spectrometer (CAS), and the Improved Performance of a Modified CDP, *Journal of Atmospheric and Oceanic Technology*, 29, 1532–1541, doi:10.1175/JTECH-D-11-00208.1, URL <http://dx.doi.org/10.1175/JTECH-D-11-00208.1>, 2012.

- Liu, X., Shi, X., Zhang, K., Jensen, E. J., Gettelman, A., Barahona, D., Nenes, A., and Lawson, P.: Sensitivity studies of dust ice nuclei effect on cirrus clouds with the Community Atmosphere Model CAM5, *Atmospheric Chemistry and Physics*, 12, 12 061–12 079, 2012.
- Lloyd, G., Choulaton, T. W., Bower, K. N., Crosier, J., Jones, H., Dorsey, J. R., Gallagher, M. W., Connolly, P., Kirchgaessner, A. C. R., and Lachlan-Cope, T.: Observations and comparisons of cloud microphysical properties in spring and summertime Arctic stratocumulus clouds during the ACCACIA campaign, *Atmospheric Chemistry and Physics*, 15, 3719–3737, doi:10.5194/acp-15-3719-2015, URL <http://www.atmos-chem-phys.net/15/3719/2015/>, 2015.
- Luebke, A. E., Afchine, A., Costa, A., Groß, J.-U., Meyer, J., Rolf, C., Spelten, N., Avallone, L. M., Baumgardner, D., and Krämer, M.: The origin of midlatitude ice clouds and the resulting influence on their microphysical properties, *Atmospheric Chemistry and Physics*, 16, 5793–5809, 2016.
- McKenna, D. S., Groß, J.-U., Günther, G., Konopka, P., Müller, R., Carver, G., and Sasano, Y.: A new Chemical Lagrangian Model of the Stratosphere (CLaMS) 2. Formulation of chemistry scheme and initialization, *Journal of Geophysical Research: Atmospheres*, 107, 2002a.
- McKenna, D. S., Konopka, P., Groß, J.-U., Günther, G., Müller, R., Spang, R., Offermann, D., and Orsolini, Y.: A new Chemical Lagrangian Model of the Stratosphere (CLaMS) 1. Formulation of advection and mixing, *Journal of Geophysical Research: Atmospheres*, 107, 2002b.
- Meyer, J.: Ice Crystal Measurements with the New Particle Spectrometer NIXE-CAPS, Dr. (univ.), Bergische Universitaet Wuppertal, Jülich, URL <http://juser.fz-juelich.de/record/22871>, record converted from VDB: 12.11.2012; Wuppertal, Univ., Diss., 2012, 2012.
- Mie, G.: Beiträge zur Optik trüber Medien, speziell kolloidaler Metallösungen, *Annalen der physik*, 330, 377–445, 1908.
- Mioche, G., Jourdan, O., Delanoë, J., Gourbeyre, C., Febvre, G., Dupuy, R., Szczap, F., Schwarzenboeck, A., and Gayet, J.-F.: Characterization of Arctic mixed-phase cloud properties at small scale and coupling with satellite remote sensing, *Atmospheric Chemistry and Physics Discussions*, 2017, 1–52, doi:10.5194/acp-2017-93, URL <http://www.atmos-chem-phys-discuss.net/acp-2017-93/>, 2017.
- Möhler, O., Stetzer, O., Schaefer, S., Linke, C., Schnaiter, M., Tiede, R., Saathoff, H., Krämer, M., Mangold, A., Budz, P., et al.: Experimental investigation of homogeneous freezing of sulphuric acid particles in the aerosol chamber AIDA, *Atmospheric Chemistry and Physics*, 3, 211–223, 2003.

- Nicolet, M., Stetzer, O., and Lohmann, U.: Depolarization ratios of single ice particles assuming finite circular cylinders, *Appl. Opt.*, 46, 4465–4476, doi:10.1364/AO.46.004465, URL <http://ao.osa.org/abstract.cfm?URI=ao-46-20-4465>, 2007.
- Osborne, S. R., Abel, S. J., Boutle, I. A., and Marengo, F.: Evolution of Stratocumulus Over Land: Comparison of Ground and Aircraft Observations with Numerical Weather Prediction Simulations, *Boundary-Layer Meteorology*, 153, 165–193, 2014.
- Pruppacher, H. R., Klett, J. D., and Wang, P. K.: *Microphysics of clouds and precipitation*, Taylor & Francis, 1998.
- Rolf, C., Krämer, M., Schiller, C., Hildebrandt, M., and Riese, M.: Lidar observation and model simulation of a volcanic-ash-induced cirrus cloud during the Eyjafjallajökull eruption, *Atmospheric Chemistry and Physics*, 12, 10 281–10 294, doi:10.5194/acp-12-10281-2012, URL <http://www.atmos-chem-phys.net/12/10281/2012/>, 2012.
- Rolf, C., Groß, J.-U., Spichtinger, P., Costa, A., and Krämer, M.: Forecasting and understanding cirrus clouds with the large scale Lagrangian microphysical model CLaMS-Ice, in: EGU General Assembly Conference Abstracts, vol. 17, p. 6862, 2015.
- Schumann, U.: Contrail Cirrus Analysis of the ML-CIRRUS Experiment: Comparisons of Model and Measurements Results, ML-Cirrus Workshop 2015, 4/5 March, MPI Mainz, 2015.
- Shupe, M. D., Daniel, J. S., de Boer, G., Eloranta, E. W., Kollias, P., Luke, E. P., Long, C. N., Turner, D. D., and Verlinde, J.: A Focus On Mixed-Phase Clouds, *Bulletin of the American Meteorological Society*, 89, 1549–1562, doi:10.1175/2008BAMS2378.1, URL <http://dx.doi.org/10.1175/2008BAMS2378.1>, 2008.
- Spichtinger, P. and Cziczo, D. J.: Impact of heterogeneous ice nuclei on homogeneous freezing events in cirrus clouds, *Journal of Geophysical Research: Atmospheres*, 115, 2010.
- Spichtinger, P. and Gierens, K.: Modelling of cirrus clouds—Part 1b: Structuring cirrus clouds by dynamics, *Atmospheric Chemistry and Physics*, 9, 707–719, 2009a.
- Spichtinger, P. and Gierens, K. M.: Modelling of cirrus clouds—Part 1a: Model description and validation, *Atmospheric Chemistry and Physics*, 9, 685–706, 2009b.
- Storelvmo, T. and Tan, I.: The Wegener-Bergeron-Findeisen process ? Its discovery and vital importance for weather and climate, *Meteorologische Zeitschrift*, 24, 455–461, doi:10.1127/metz/2015/0626, URL <http://dx.doi.org/10.1127/metz/2015/0626>, 2015.
- Taylor, J. W., Choulaton, T. W., Blyth, A. M., Liu, Z., Bower, K. N., Crosier, J., Gallagher, M. W., Williams, P. I., Dorsey, J. R., Flynn, M. J., Bennett, L. J., Huang, Y., French, J., Korolev, A., and Brown, P. R. A.: Observations of cloud microphysics and ice formation during

- COPE, *Atmospheric Chemistry and Physics*, 16, 799–826, doi:10.5194/acp-16-799-2016, URL <http://www.atmos-chem-phys.net/16/799/2016/>, 2016.
- Voigt, C., Schumann, U., Minikin, A., Abdelmonem, A., Afchine, A., Borrmann, S., Boettcher, M., Buchholz, B., Bugliaro, L., Costa, A., et al.: ML-CIRRUS-The airborne experiment on natural cirrus and contrail cirrus with the high-altitude long-range research aircraft HALO, *Bulletin of the American Meteorological Society*, 2016.
- Wallace, J. M. and Hobbs, P. V.: *Atmospheric science: an introductory survey*, vol. 92, Academic press, 2006.
- Wang, M. and Penner, J. E.: Cirrus clouds in a global climate model with a statistical cirrus cloud scheme, *Atmospheric Chemistry and Physics*, 10, 5449–5474, 2010.
- Wang, M., Liu, X., Zhang, K., and Comstock, J. M.: Aerosol effects on cirrus through ice nucleation in the Community Atmosphere Model CAM5 with a statistical cirrus scheme, *Journal of Advances in Modeling Earth Systems*, 6, 756–776, doi:10.1002/2014MS000339, URL <http://dx.doi.org/10.1002/2014MS000339>, 2014.
- Weigel, R., Spichtinger, P., Mahnke, C., Klingebiel, M., Afchine, A., Petzold, A., Krämer, M., Costa, A., Molleker, S., Reutter, P., et al.: Thermodynamic correction of particle concentrations measured by underwing probes on fast-flying aircraft, *Atmospheric Measurement Techniques*, 9, 5135, 2016.
- Wendisch, M. and Brenguier, J.-L.: *Airborne measurements for environmental research: methods and instruments*, John Wiley & Sons, 2013.
- Wendisch, M., Yang, P., and Ehrlich, A.: Amplified climate changes in the Arctic: Role of clouds and atmospheric radiation, *Sitzungsberichte der Saechsischen Akademie der Wissenschaften zu Leipzig. Mathematisch-Naturwissenschaftliche Klasse*, 132, 1–34, 2013.
- Wendisch, M., Pöschl, U., Andreae, M. O., Machado, L. A. T., Albrecht, R., Schlager, H., Rosenfeld, D., Martin, S. T., Abdelmonem, A., Afchine, A., Araùjo, A., Artaxo, P., Aufmhoff, H., Barbosa, H. M. J., Borrmann, S., Braga, R., Buchholz, B., Cecchini, M. A., Costa, A., Curtius, J., Dollner, M., Dorf, M., Dreiling, V., Ebert, V., Ehrlich, A., Ewald, F., Fisch, G., Fix, A., Frank, F., Fütterer, D., Heckl, C., Heidelberg, F., Hüneke, T., Jäkel, E., Järvinen, E., Jurkat, T., Kanter, S., Kästner, U., Kenntner, M., Kesselmeier, J., Klimach, T., Knecht, M., Kohl, R., Kölling, T., Krämer, M., Krüger, M., Krisna, T. C., Lavric, J. V., Longo, K., Mahnke, C., Manzi, A. O., Mayer, B., Mertes, S., Minikin, A., Molleker, S., Münch, S., Nillius, B., Pfeilsticker, K., Pöhlker, C., Roiger, A., Rose, D., Rosenow, D., Sauer, D., Schnaiter, M., Schneider, J., Schulz, C., de Souza, R. A. F., Spanu, A., Stock, P., Vila, D., Voigt, C., Walser, A., Walter, D., Weigel, R., Weinzierl, B., Werner, F., Yamasoe, M. A., Ziereis, H., Zinner,

- T., and Zöger, M.: The ACRIDICON-CHUVA campaign: Studying tropical deep convective clouds and precipitation over Amazonia using the new German research aircraft HALO, *Bulletin of the American Meteorological Society*, 0, n.a., doi:10.1175/BAMS-D-14-00255.1, URL <http://dx.doi.org/10.1175/BAMS-D-14-00255.1>, 2016.
- Wernli, H., Boettcher, M., Joos, H., Miltenberger, A. K., and Spichtinger, P.: A trajectory-based classification of ERA-Interim ice clouds in the region of the North Atlantic storm track, *Geophysical Research Letters*, pp. n/a–n/a, doi:10.1002/2016GL068922, URL <http://dx.doi.org/10.1002/2016GL068922>, 2016GL068922, 2016.
- Wilson, T. W., Ladino, L. A., Alpert, P. A., Breckels, M. N., Brooks, I. M., Browse, J., Burrows, S. M., Carslaw, K. S., Huffman, J. A., Judd, C., et al.: A marine biogenic source of atmospheric ice-nucleating particles, *Nature*, 525, 234–238, 2015.
- Wylie, D., Jackson, D. L., Menzel, W. P., and Bates, J. J.: Trends in Global Cloud Cover in Two Decades of HIRS Observations, *Journal of Climate*, 18, 3021–3031, doi:10.1175/JCLI3461.1, URL <http://dx.doi.org/10.1175/JCLI3461.1>, 2005.
- Yano, J.-I. and Phillips, V. T. J.: Ice–Ice Collisions: An Ice Multiplication Process in Atmospheric Clouds, *Journal of the Atmospheric Sciences*, 68, 322–333, doi:10.1175/2010JAS3607.1, URL <http://dx.doi.org/10.1175/2010JAS3607.1>, 2011.

A Single particle events in the NIXE-CAPS data

Evaluations of measured total cloud particle concentrations (section 2.4) have shown that in general, in-situ datasets of particle measurements have to be cleared from data points that were caused by one single particle in the instrument's sampling area ('single particle event'). The following sections show the resulting concentrations from single particle events, evaluate how strongly and often these events influenced the obtained particle concentrations and size distributions during ML-Cirrus, and present a discussion on how a removal of those events affects the cloud dataset.

What determines the peak concentration?

A closer look at the NIXE-CAPS cloud particle concentration frequency spectrum during the ML-Cirrus campaign shows that such peaks occur at the lowest detectable concentration for each instrument (see Figure A.1). The peak for the CAS instrument, however, reaches higher absolute values than the one for the CIP. To explain what causes the peak and what determines the measurable concentration ranges, it is necessary to evaluate the sampling volumes of each instrument.

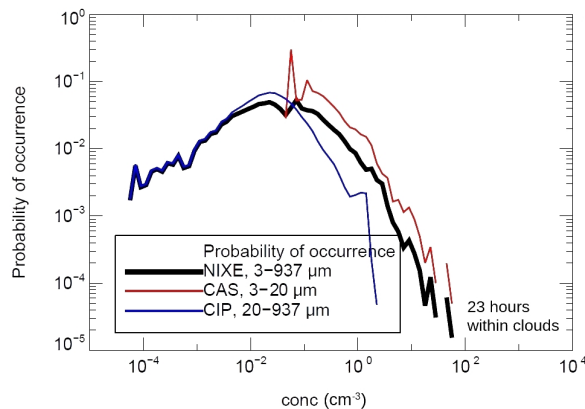


Figure A.1: Frequency of occurrence of cloud particle concentrations in the ML-Cirrus measurements.

A number of cloud and aerosol particle probes use the two measurement techniques used in NIXE-CAPS: particles pass a laser beam and cause a) shadow images or b) forward/backward scattering patterns. The shadow images or scattering intensities are used to derive particle sizes and particle concentrations. For the latter (*conc*), particle counts (*N*) are divided by the respective sampling volume (*SV*):

$$\text{conc} = \frac{N}{SV} \quad (\text{A.1})$$

The size range of particles that can be measured varies from instrument to instrument, depending on the measurement technique, the proportions of the sensor array, and so on. In the same way, the measurable particle concentrations are limited by the respective sampling volume. The sampling volume is determined by the sampling area (*SA*) – the two-dimensional area that a particle has to pass in order to be recorded as valid particle. The second parameter is the length of the flightpath. It is found by multiplying the true air speed (*TAS*) with the chosen time interval (*t*), usually one second:

$$SV = SA * TAS * t \quad (\text{A.2})$$

Figure A.2 shows the CAS sampling volume in dependence of the TAS. The sampling area is fixed ($SA = 0.25 \text{ mm}^2$); i.e. the sampling volume only depends on the speed of the aircraft. The CAS instrument records particles up to $50 \mu\text{m}$ in diameter (see subsection 2.1.1). Thus, the particle diameters are much smaller than the width of the laser beam. It can therefore be assumed that the sampling area does not depend on particle sizes. This is different for the

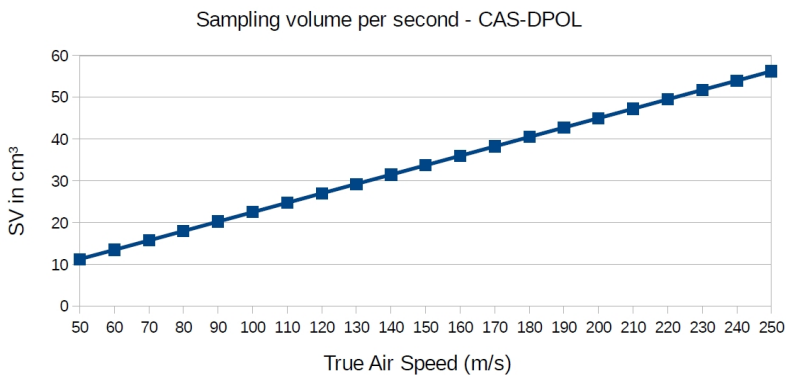


Figure A.2: The CAS sampling volume (*SV*) only depends on the speed of the aircraft.

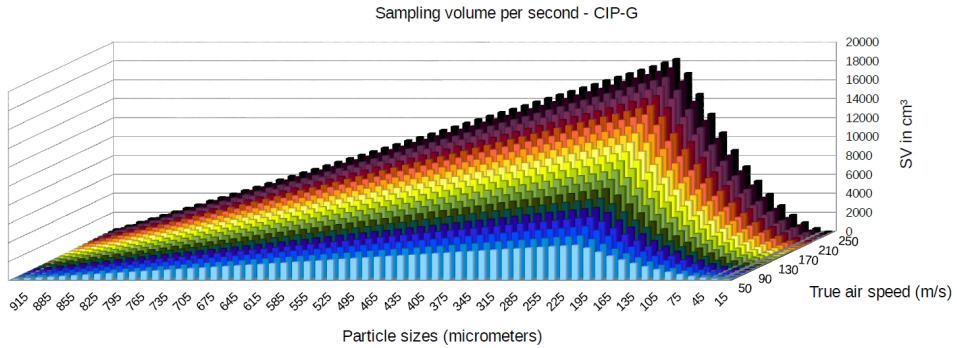


Figure A.3: The CIP sampling volume (SV) in dependence on the speed of the aircraft and the size of the measured particles.

CIP probe that obtains particle shadow images (see subsection 2.1.2). It records particles in the size range of $7.5 \mu\text{m}$ to $960 \mu\text{m}$, thus approaching the limits of its sensor array which can size particles of up to $937 \mu\text{m}$ in diameter. The larger a particle is, the higher the probability that it touches one or both borders of the sampling area – only particles passing perfectly in the middle of the SA will be counted as valid (cf. subsection 2.1.2). This restricts the effective sampling area for large particles to a smaller value (DMT, 2009). Figure A.3 shows how the effective sampling volume increases with decreasing particle sizes, until it reaches a maximum at particles of $200 \mu\text{m}$ in diameter.

Particles with diameters smaller than $200 \mu\text{m}$ will – again – meet a smaller sampling area. This is due to the size-dependance of the depth of field (DOF). Particles with diameters of $200 \mu\text{m}$ and more are large enough to produce focussed images at any point within the CIP laser beam (open path length: 10 cm). The smaller the particles are, however, the closer they need to be to the focal point of the CIP laser beam in order to produce an unblurred shadow image, otherwise they are rejected. The CIP sampling area – and with it the sampling volume – therefore decreases for particles smaller than $200 \mu\text{m}$.

The lowest sampling volumes are found at the lowest True Air Speeds, occurring for example at the slow, low to medium altitude flights with the Polar-5 aircraft (see chapter 3). At 50 ms^{-1} , the CIP sampling volume goes down to 75 cm^{-3} per second for particles with $D_p = 937 \mu\text{m}$ and 25 cm^{-3} per second for particles with $D_p = 15 \mu\text{m}$.

Due to the CIP's large sampling areas, its sampling volumes are generally much larger than the one of the CAS. The CIP can thus detect lower particle concentrations than the CAS. In the NIXE-CAPS setup, this means that large particles can be recorded also in low concentrations, while higher concentrations are necessary for small particles.

Connecting sampling volumes and concentrations

Apart from 'no particles' - a clear sky situation - 'one single particle' is the lowest number any instrument can record per time unit during a flight. This trivial event – one particle within a given time interval – can lead to a number of different conclusions on the underlying particle concentration. This is elaborated in the following section. The following two plots depict the particle concentrations per second that result from recording one particle during one second, each for the CIP (Figure A.5) and the CAS (Figure A.4). Due to its small sampling volume, the CAS will diagnose larger particle concentrations from recording one particle than the CIP instrument: At 50 ms^{-1} and in the overlapping size range between 15 and $50 \mu\text{m}$, the difference between the found concentrations covers the factors two to twenty: The CIP would find a concentration of 0.0403 cm^{-3} (particle diameter $15 \mu\text{m}$), 0.0103 cm^{-3} ($30 \mu\text{m}$) or 0.0046 cm^{-3} ($45 \mu\text{m}$) based on one single particle, whereas the CAS would always find a concentration of 0.0800 cm^{-3} .

As long as the measurements take place within a cloud of sufficient density, i.e. with a particle concentration that will lead to at least one particle per second in both instruments, the cloud concentration will be measured accurately: Depending on the aircraft speed, the critical density for the CAS is between 0.02 cm^{-3} to 0.09 cm^{-3} . If a cloud is less dense, however, the CAS 1 Hz data will be the first dataset to suffer from undersampling, i.e. although within a cloud, less than one particle per second will be detected by the instrument. With a decreasing cloud concentration, the time intervals have to be enlarged (0.5 Hz , 0.25 Hz data...) to enable accurate CAS measurements - but this approach will decrease the data quality: highly resolved cloud features in the CIP measurements will be blurred and cloud edges will be smeared.

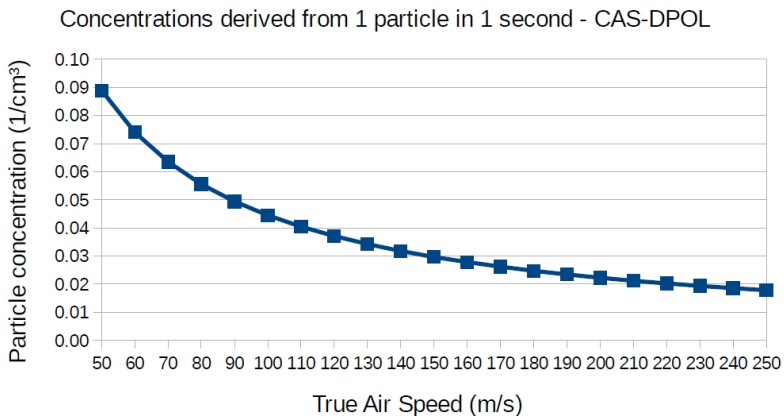


Figure A.4: Particle concentrations obtained from one single particle passing the CAS' sampling volume at different airspeeds.

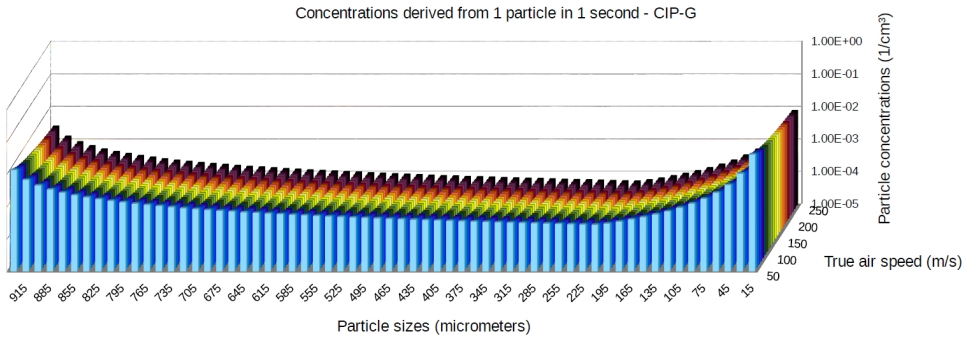


Figure A.5: Particle concentrations obtained from one single particle passing the CIP's sampling volume at different airspeeds, for the size range of particles detectable by CIP.

Cirrus clouds have average densities of 0.01 to 0.5 cm^{-3} (compare Figure 2.12). It is evident that during airborne measurements, the high concentration resulting from one particle in the CAS sampling volume can cause a misinterpretation of this 'single particle event' as a cirrus cloud - under otherwise 'clear sky' conditions (i.e. no particles detected by the CIP).

This type of error has, however, no significant influence on the NIXE-CAPS dataset: An analysis of the ML-Cirrus data shows that if all 'single particle events' in the CAS instrument are removed, only 3% of the cloud measurements are lost. This means that in only 3% of the measurements, a cloud event relied on one particle in the CAS instrument alone. In most of the data points within clouds, large particle numbers were recorded by the CIP instrument.

But measurements in those CIP-dominated cirrus clouds, too, can be biased by single particle events in the CAS. Due to its large sampling volume, the CIP can record particle concentrations down to 10^{-4} cm^{-3} in the 1 Hz dataset. Whenever a single particle appears in the CAS instrument, these resulting total concentrations (CAS+CIP) will be close to the CAS minimum concentration of about 10^{-2} cm^{-3} . Due to the magnitude of the difference in concentrations, the CIP measurements will modify the total concentration for this second only marginally. Averages over long times of flight will give accurate concentration results for both instruments, as long as all data points are within the cloud. On cloud edges, clear sky segments will be wrongly classified as clouds.

Cloud measurements in which the CIP recorded low particle concentrations $< 0.01 \text{ cm}^{-3}$ were frequently found during ML-Cirrus (see Figure 2.12). Single particle events in the CAS modified 17.33% of those cirrus cloud concentrations towards values between 0.02 and 0.05 cm^{-3} , even though on larger time intervals the CAS would have showed lower concentrations. In the statistical plots showing the frequency of occurrence of ice particle concentrations (Figure 2.11 and Figure 2.12), these local high particle concentrations in the 1 Hz dataset cause the peak at 10^{-2} cm^{-3} .

Particle size distribution errors

It was shown in the previous section that 'single particle events' lead to particle concentrations of 0.016 cm^{-3} to 0.08 cm^{-3} in the CAS measurements. Not only the total concentrations, also the size distributions obtained by a combination of CIP and CAS measurements are affected by these events.

The following scenario simulates a measurement situation in a cirrus cloud, consisting of particles with a size mode at $200 \mu\text{m}$ and a standard deviation of $100 \mu\text{m}$. In this setting, cloud particles with $D_p < 50 \mu\text{m}$ will represent about 5% of all particles (Figure A.6). With a cloud density of 0.01 cm^{-3} , particles $< 50 \mu\text{m}$ that can be recorded by the CAS are expected to cross the sampling area once per 100 seconds. Per second, about 140 particles will be registered in the CIP sampling area.

In the simulation, this cloud is now probed for 100 seconds, which corresponds to a flightpath of 20 kilometers. The size distribution $> 50 \mu\text{m}$ (CIP) is the same for all 100 seconds. Most of the seconds therefore show the count and size distribution as shown in Figure A.7 from 80 to $300 \mu\text{m}$.

During one second, however, a particle with $D_p = 20 \mu\text{m}$ occurs in the CAS. In the second of this event, the small particle creates a sharp peak in the size distribution, as can be seen in Figure A.7.

The influence of this event can be decreased by enlarging the sampling volume. This can be done by calculating particle concentrations not for one, but for several seconds. In a ten-second-interval, the 'single particle event' would however still show up (see blue line in Figure A.7).

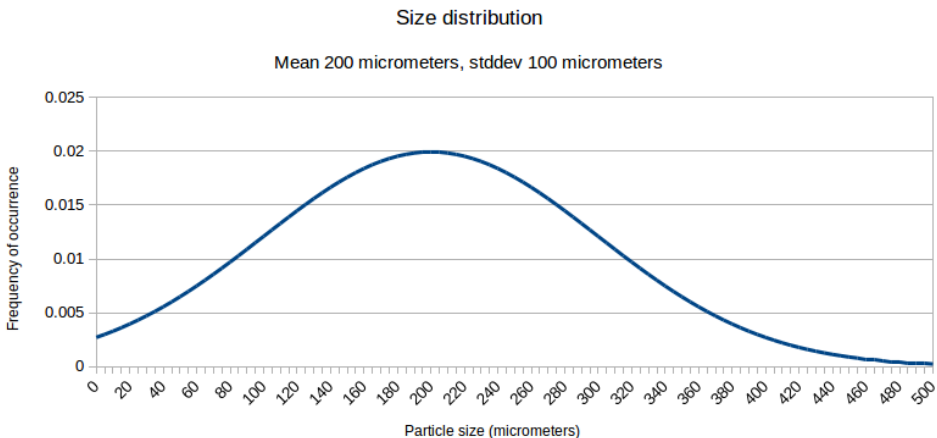


Figure A.6: Simulated size distribution for a typical cirrus cloud.

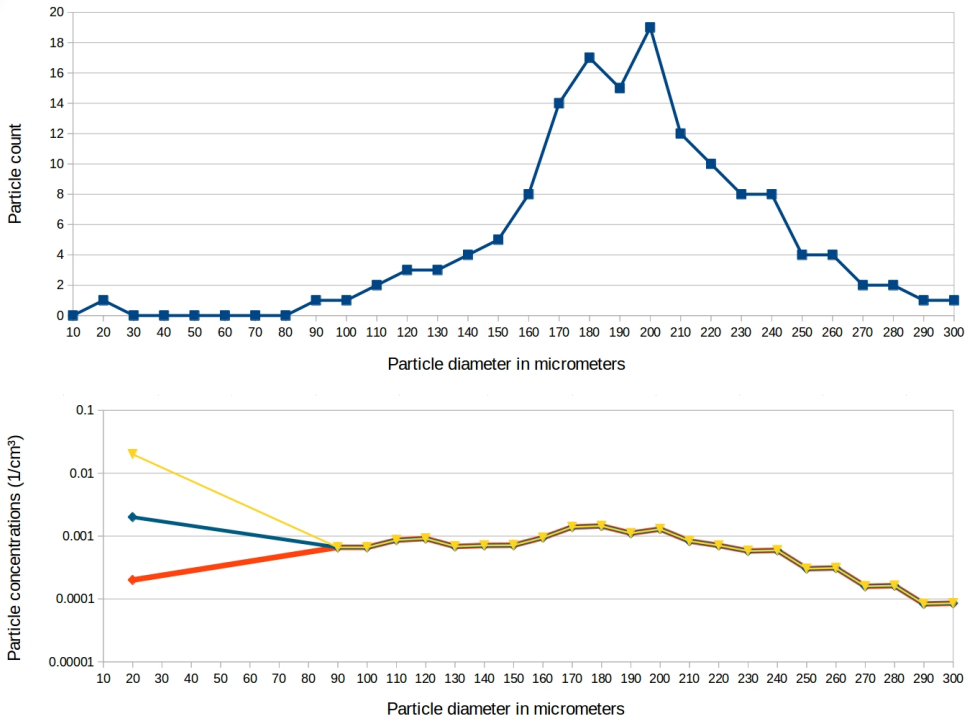


Figure A.7: Particle counts and resulting size distributions for an idealized cirrus cloud measurement. One particle at $20 \mu\text{m}$ is recorded. This single particle has a significant influence on the size distribution averaged for 1 second of flight (yellow). When averaging over 10 seconds (blue line), the single particle's influence on the size distribution is still comparable to the numbers obtained by the bulk of larger cloud particles. Only when averaging over 100 seconds (red line), the size distribution gives a hint that the small particle was a rare event compared to the frequent occurrence of large particles.

And after averaging over the full 100 seconds the single particle event would still be visible (see red line Figure A.7). The resulting concentration for small particles is still comparable to those caused by the bulk of particles recorded in the CIP-G measurement range above $50 \mu\text{m}$. This large averaging time of 100 seconds requires a homogeneous cloud field over 20 kilometers. Such a long homogeneous cloud is unlikely to occur, which means that in the data analysis one has to compromise between choosing sufficiently large time intervals to set the concentrations of the CAS instrument into context, but also sufficiently small time intervals to accurately determine cloud edges and inhomogeneities within the clouds that are captured by the CIP instrument. Averaging over very large time scales does therefore not provide a solution for the 'single particle event' problem. The cloud edges would have to be smeared over dozens of kilometers to remove the influence of one irregular 'single particle', recorded by an instrument

with a small sampling volume. A different approach is to simply remove 'single particle events' from the dataset. Whenever only one single particle is recorded, it will be marked as invalid. Thus, the size distributions of the cirrus cloud shown above are cleared – on all shown time scales. This approach is discussed in the following.

Removing 'single particle events' from particle size distributions

Clouds do have particle concentrations that would result in 'one particle per bin and time unit' or less in the insitu measurements (see Figure A.8). These clouds – as well as thinner clouds – can not be measured any more, when single particle events are excluded from the dataset. It is therefore necessary to assess how many measurements would be lost in this case.

The first thing to note is that this approach only concerns instruments with small sampling volumes. The removal of single particles in the dataset therefore systematically affects the cloud probes designed for small particle sizes. Data losses due to this removal occur when these instruments are operated in clouds with low concentrations of small particles. This indicates that the removal of single particles mostly affects clouds where the small particle population does not contribute significantly to the cloud size distribution. As shown above, less than 3% of all ice clouds probed during the 20 hours of measurements during ML-Cirrus would be lost due to removing single particle events. Clouds that are rich in particles with small diameters (such as lee wave cirrus or contrails) easily exceed the required 'at least two particles' per bin and time unit in our measurements and would not be affected. Clouds with predominantly large particles are either not affected at all (80% of the ML-Cirrus measurements) or only suffer from an increased uncertainty in the total concentration with regard to the contribution of small particles, which constitute less than 5% of the measurable size range and were simulated to contribute about 5% of a typical cirrus cloud size distribution (see Figure A.6). The removal of

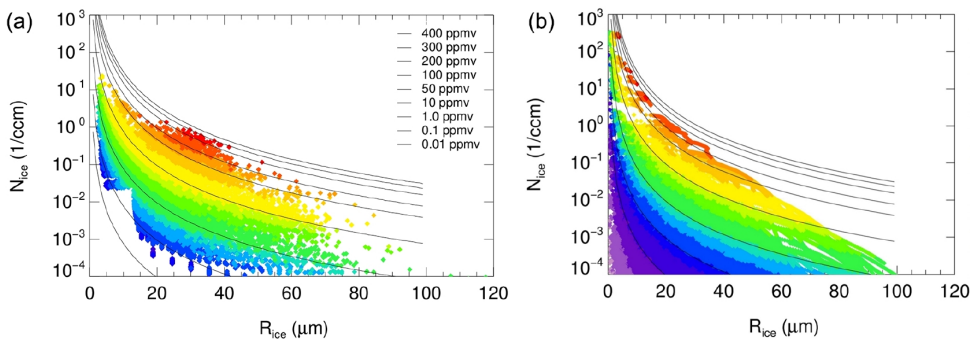


Figure A.8: Left panel (a): Overview of measurements during ML-Cirrus: Low concentrations of small particles (CAS size range) could not be detected, although they are simulated to occur in the microphysical model MAID (right panel, b). The colors indicate the associated ice water content. Image taken from Krämer et al. (2016b).

single particle events modifies 17% of the ML-Cirrus data.

Secondly, there has always been an invisible 'lower concentration limit' in particle measurements: Every particle instrument has cut-off concentrations below which not enough particles reach the instrument's sampling volume to conclude on the underlying cloud concentration. If cloud particle concentrations below the respective cut-off value occur, single particle events cause local large 'measured cloud concentrations'. Since small concentrations can easily occur especially in cirrus clouds, this results in a dominating feature in plots depicting the frequency of occurrence of particle concentrations, e.g. as shown in Figure 2.11. These 'artificially high' concentrations can not be recalculated to their actual low value, because this option - enlarging the averaging time interval and thus the sampling volume - would lead to a loss on information e.g. on the cloud extent. Excluding 'single particle events' is therefore the only way to address this lower limit quantitatively: With this approach, a necessary minimum concentration can be calculated from the sampling area and air speed data. Without removing single particle events, any low concentration might - depending on the length of the flightpath inside the cloud - trigger an event in the dataset, leaving the actual confidence level of the concentration measurement hidden.

Are two particles better than one?/How many particles are necessary for a valid concentration measurement?

Figure A.9 shows how often 'single particle events' occurred during the ML-Cirrus campaign. The CAS instrument has much more single particles per time unit than the CIP. The reason for this difference is the frequency of occurrence of cloud particle concentrations in the atmosphere. The CAS' measurable concentration range ends in the middle of the natural concentration range of cirrus clouds: Over long flying times within clouds, these smaller concentrations are likely to cause single particle events in the CAS. Whenever such a low concentration leads to one particle being recorded in the CAS, this event increases the frequency of occurrence of the CAS minimum measurable concentration, leading to the peak as shown in Figure A.10 and measured during ML-Cirrus (Figure 2.12). Which lower concentration precisely caused the event can not be derived from the CAS data without lowering the data resolution and thus the frequency, as explained before. Therefore, data from 'single particle events' - and only these data - can not be interpreted.

In principle, the same happens in the CIP measurements. However, the detectable concentration range of the CIP instrument reaches much lower values - and clouds with particle concentrations of less than 0.001 cm^{-3} are rare (see Figure 2.12). Therefore, the CIP's single particle events are rare as well (compare red line in Figure A.10).

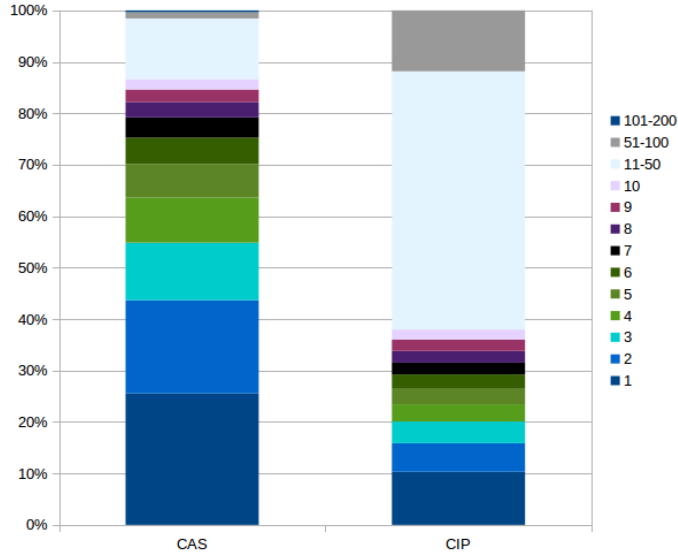


Figure A.9: Frequency of occurrence of cloud particle numbers in the ML-Cirrus measurements. 'Single particle events' are more common in the CAS than in the CIP. Figure A.10 explains the background.

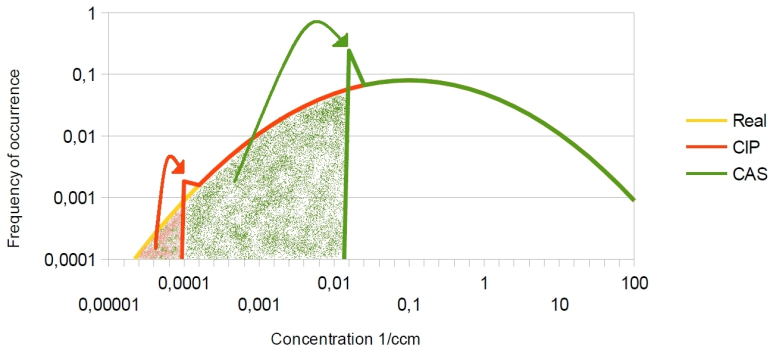


Figure A.10: Frequency of occurrence of cloud particle concentrations in an ideal case. The yellow curve marks the 'real' cloud particle concentration distribution. The green and red curve show what the CAS and CIP instrument would measure, respectively: all concentrations below the detectable concentration limit cause signals at this detection limit. The actual low concentrations that lead to the peak cannot be derived from the measurements.

B Data evaluation with the NIXElib

As described in chapter 2, NIXE-CAPS consists of four components: CAS, CIP, a Hotwire and a Pitot tube. The raw data of CAS, CIP and Hotwire are saved in different file formats simultaneously: a raw file and a cvs file, respectively. All csv files contain the velocity information obtained by the Pitot tube. Additionally, there is a CAS PBP (particle by particle) file and a CIP image file. Apart from basic housekeeping data, these raw/cvs files store histogram information on the bulk properties of all particles that have passed the NIXE-CAPS sensors during one second (1 Hz histograms). The PBP and image file additionally contain particle-by-particle information, such as sizes and inter-arrival times, for each registered particle separately.

The raw data need to be processed further and several corrections have to be applied. As explained in subsection 2.1.2, the sampling volume is crucial for the calculation of particle concentrations. Initially, all particle concentrations stored in these files are calculated with a sampling volume based on the probe air speed (PAS) measured with the Pitot tube. Within the CAS tube, however, the flow velocity increases (A. Afchine, personal communication), therefore the true air speed (TAS) recorded by the aircraft instrumentation is used here. Also, the CIP sampling volume has to be corrected to account for the adiabatic air compression that occurs at large aircraft speeds in front of the instrument (Weigel et al., 2016).

Further, the time line in these files depends on a central unit recording the NIXE-CAPS data (HALO, POLAR 5/6) or an independent data unit within the NIXE-CAPS container (new Geophysica setup). Consequently, these time lines have to be checked and sometimes corrected to match UTC times.

To apply these corrections and to produce standard data products such as joint particle size distributions between the NIXE-CAPS components, the IDL routine library NIXElib has been developed by Meyer (2012). In the frame of this work, it was optimized with regard to computation time and user friendliness, and additional options were added. In the following, the structure, options and products of the NIXElib will be shortly described.

B.1 NIXElib description and new features

Masternixe settings

The NIXElib routines are coordinated from the so-called 'masternixe' files. These files regulate which NIXElib modules will be employed to process the data. With this system, it is possible to

e.g. repeat certain analysis steps with various settings without repeating all calculations. The masternixe files also contain the locations in the file system from which raw data files will be accessed and where the output is written.

A number of options can be chosen in the masternixe files that change the way in which the raw data are interpreted by the NIXElib routines. Since this can change the output significantly, these choices have to be documented carefully and have to be made clear when presenting the observations. The standard options used in this work are listed in section B.2.

- 'SODA sizing': The images recorded by the CIP instrument are 2D shadow images. The size of particles in these images can be interpreted in different ways: 'Maximum dimension' will chose the largest particle diameter, 'x size' will chose the largest extend in x direction, 'areaseize' will reassemble the image pixels into a circle. The peak of the size distribution derived from these images can vary for different sizing methods, especially for irregular ice crystals.
- 'SODA SV (sampling volume) method': Here, the 'allin' or 'reconstructed' method can be chosen (see subsection 2.1.2).
- 'grey thresh[old]': The CIP instrument records particle images in three grey levels: up to 35% shadowing ('greythresh 0'), up to 75% shadowing ('greythresh 1'), and up to 100% shadowing ('greythresh 2'). Note that this sizing decision can strongly influence the concentrations found for small particle sizes (see subsection 2.1.2).
- 'correct spe': This option en- or disables the algorithm described in section 2.4.
- 'out of focus correction': Small particles passing the CIP laser beam outside its depth of field (DOF) can cause false images of enlarged - but weak - concentric rings (see subsection 2.5.3). The correction algorithm for these 'Poisson spots' analyses the size of these ring images and calculates the original particle size.
- 'IAT (inter-arrival time) correction': The IAT correction algorithm by Field et al. (2006) removes shattering artefacts as described in subsection 2.5.2.
- 'Aircraft speed': Depending on the choice of input data, different air speeds are used to calculate the sampling volume and thus the particle concentrations. Due to the aircraft wing's shape, the air speed is lower around the NIXE-CAPS than at the nose boom, where the 'TAS' (true air speed) is measured by the avionik instrumentation. NIXE-CAPS records the air speed in its vicinity with the Pitot tube ('PAS', probe air speed). As long as no avionik data are available, all sampling volumes have to be calculated using the PAS. As soon as there are external data, the external air speed can be used by choosing 'CASmod' as CAS histogram data type. The CIP histogram data are analysed in the

same way: 'CIP' with PAS, 'CIPmod' with TAS. The CIP images and CAS PBP data are processed with the same air speed that was chosen for the respective histogram data.

Main modules of the NIXElib

The NIXElib is divided into modules: 'conc', 'phase', 'output', and 'compare'. Four more features, 'nixe plot', 'plot diverse', 'synchronize timeline', and 'plot temperature average' are disabled in the updated NIXElib version.

Conc routines

The module 'conc' performs all analyses necessary to retrieve particle concentrations and size distributions from the NIXE measurements. Within this module, the most basic steps of the data analysis are done: Truncated raw data files are joined and raw data files are decoded. External data are read in, decoded in a platform-specific routine, and synchronized with the NIXE-CAPS measurements. Also, an air speed for the sampling volume calculation is chosen. Because of these steps, the 'conc' module always has to be run as the first step of a new data analysis.

If a CIP image analysis was chosen, the 'conc' module also starts the SODA2 module. In SODA2, the large raw image files are read in and broken down into single particles. These single images are screened for rejection criteria (such as the IAT threshold or the 'noise' analysis, see subsection 2.1.2). Particles are flagged as 'allin' if its shadow image does not touch the borders of the image array. The sizes of the accepted particles are recorded using the chosen sizing algorithm. Time and size information are stored in a particle-by-particle file. Furthermore, SODA2 finds the sampling volume for each bin size and second (see subsection 2.1.2) and calculates particle concentrations.

If inter-arrival time corrections are performed, plots showing the inter-arrival time distributions for bulks of 100 particles are saved in the output folder.

The main routine of the 'conc' module assembles then the SODA2 data, the CIP histogram data, the CAS histogram data and the CAS PBP information into one netcdf output file.

Phase routines

The module 'phase' does the shape analysis of the NIXE-CAPS particles. Its name originates from the assumption that spherical particles can only be liquid water (which is not always the case, as shown recently by Järvinen et al. (2016)) - a shape analysis would therefore allow to determine the particles' phase.

Instead, the phase routines perform the asphericity calibration analysis for the particles recorded by the CAS. In this procedure, a threshold is defined that allows to sort the CAS particles into the categories 'spherical' and 'aspherical' (see subsection 2.1.1). Aspherical fractions are then derived for each second of measurement; this has to be monitored carefully for measurements

with low particle number densities, e.g. AIDA experiments.

The CIP shape analysis is performed using the algorithm by Korolev and Sussman (2000) (see subsection 2.1.2). They are currently displayed in the automatic 'overview' plot (see Figure B.1) but not used in any analysis.

Output routines

The 'output' routines allow to create netcdf, NASA ames, KIT-specific 'ict' and simple ascii data files.

Compare routines

The 'compare' module was created to synchronize the NIXE-CAPS data with other instruments, e.g. other particle spectrometers like the CPSD, to perform instrument comparisons.

B.2 User options and standard settings

Comparisons of data evaluation algorithms have shown that the settings under which the analysis is performed can influence its outcome (cf. chapter 2). For the NIXE-CAPS studies, the following settings were chosen for the CIP measurements: Pixels of all shadow intensities $> 0\%$ are considered as part of the image (grey threshold: 0), so that only slightly shadowed pixels e.g. of transparent ice crystals are also recognized as part of the image. Only particle shadow images that don't touch the borders of the recording field ('all-in') are accepted; this influences the sampling area of the probe (see subsection 2.1.2). Concerning the particle size, the number of pixels that are part of the image are counted and the particle size is defined as the diameter of a circle covering this amount of pixels ('areazise' or 'equivalent size' method). An IAT correction is applied to remove shattering fragments (subsection 2.5.2).

In the frame of this work, the NIXElib routines were accelerated. A standard data analysis with regard to particle concentrations is available within about 20 minutes (times vary depending on the number of cloud particles recorded). A full analysis including particle shapes may take between one and two hours. The NIXElib produces an overview plot showing the main measurement results (see Figure B.1): Temperature and pressure, true air speed (TAS, avionic data) and probe air speed (PAS) in the top panel; particle size distributions of CAS and CIP below; cloud and aerosol particle number concentrations in the middle; separate particle number concentrations for spherical and aspherical particles as well as the aspherical fraction per second in the fourth panel; and the aspherical fractions per second and size bin in the bottom panel. Figure B.2 illustrates the effect of the 'single particle event' correction: CAS and CIP instrument show a better agreement of their size distributions; a wider range of concentrations is visible in panel 3.

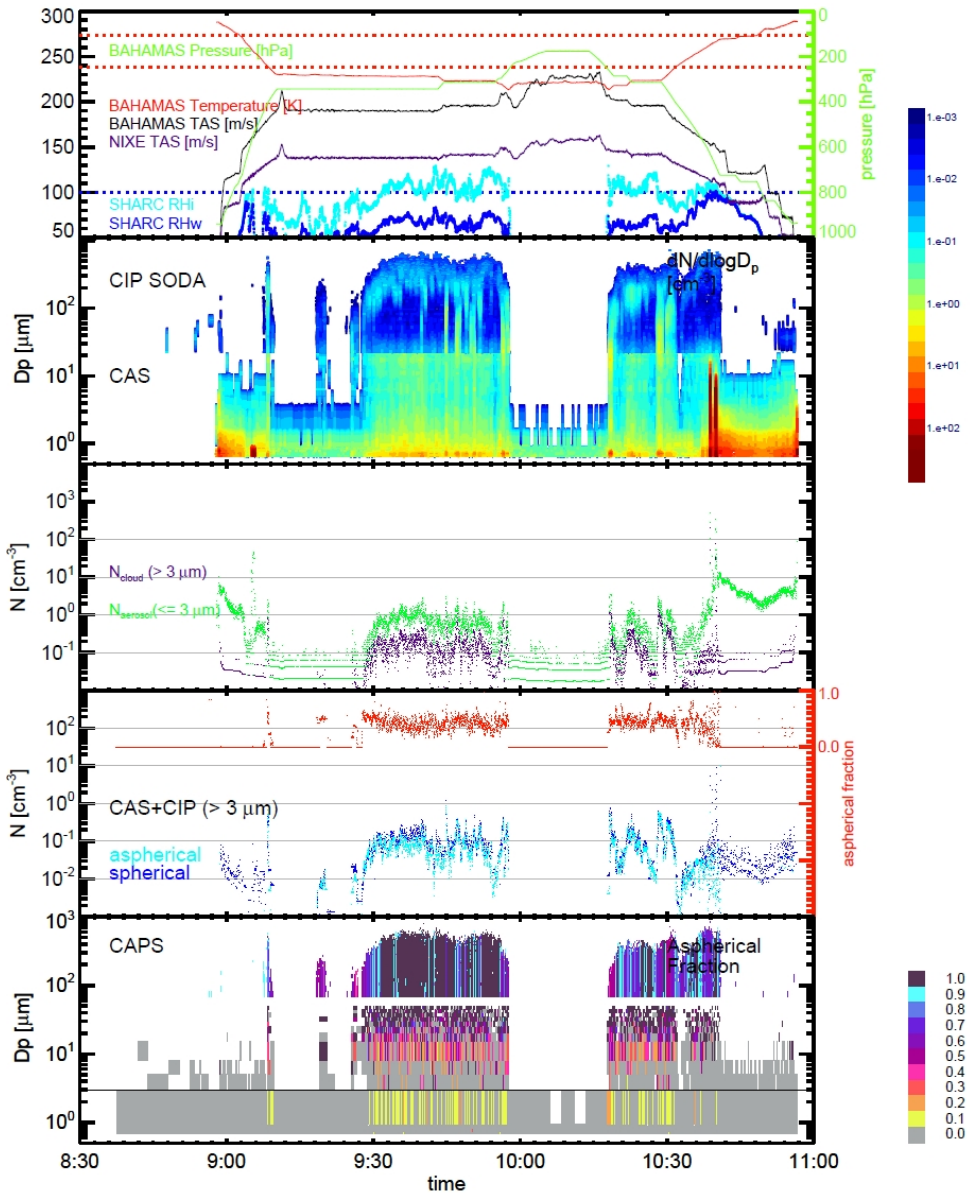


Figure B.1: Standard NIXElib plot for ML-Cirrus flight 03 on 22.03.2014.

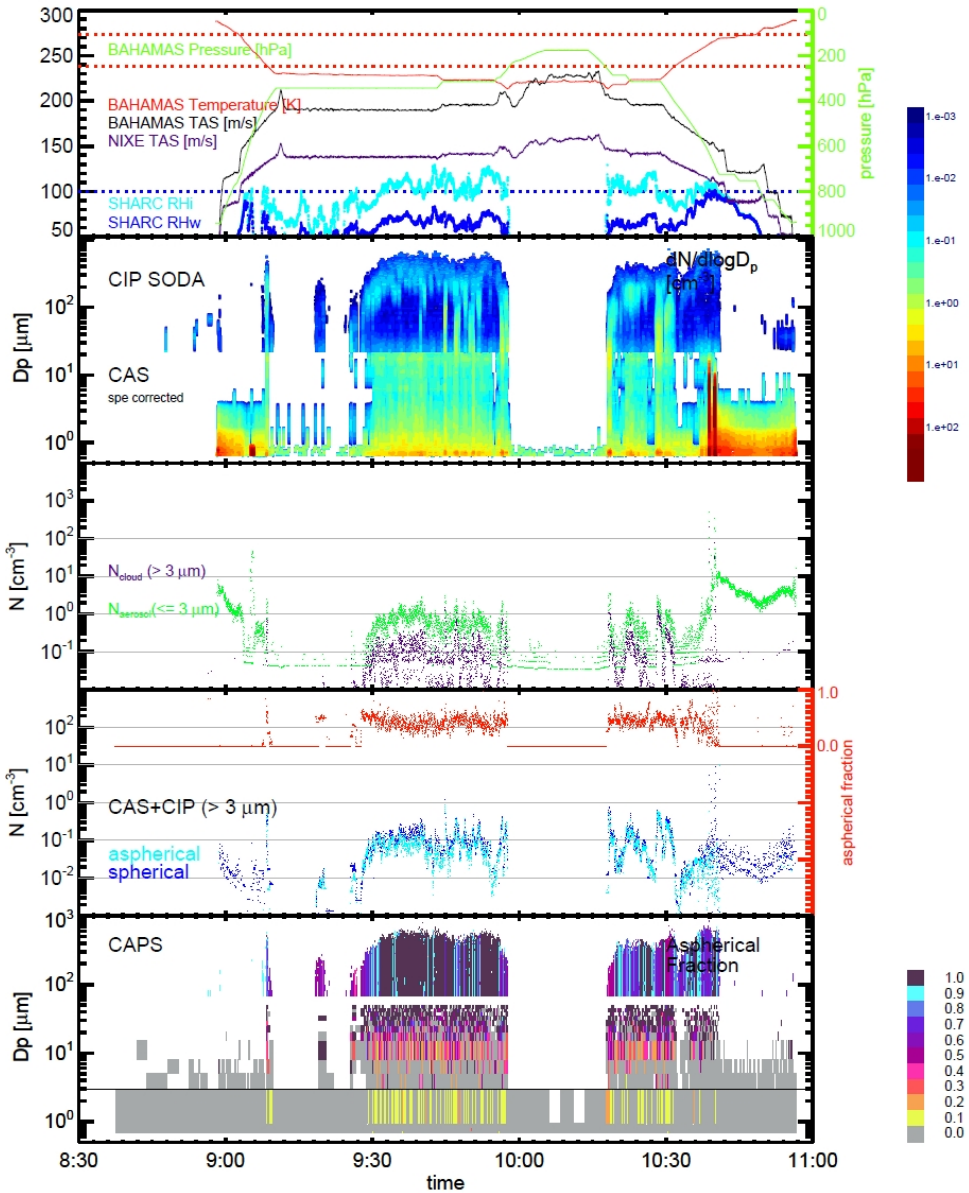


Figure B.2: Same as Figure B.1, but with 'single particle event' correction in the CAS data.

C Acknowledgments

This thesis was prepared using the results of a number of multi-year projects and profited from the ideas, experience and advice of several people.

At first, I would like to thank Dr. Martina Krämer for the supervision of this work, the productive discussions, the opportunity to present the results at the AMS and EGU conferences, and the chance to participate in the measurement campaigns AQUAVIT-II, AIRTOSS-Ice, ML-Cirrus, ACRIDICON, and RICE03, which were an invaluable experience for me. I'm thankful to Prof. Dr. Ralf Koppmann and Prof. Dr. Martin Riese for the supervision of this work, and the fruitful discussions at the seminar talks. I thank Dr. Christian Rolf for being a patient teacher of IDL and FORTRAN, for his introductions to the FISH instrument - my first contact with airborne measurements - and his advice throughout the preparation of this dissertation. To both him and Dr. Jens-Uwe Grooß, I'm thankful for their cooperation and support during the work with CLaMS-Ice. I'm grateful that Armin Afchine and Dr. Jessica Meyer shared their experience with me regarding the NIXE-CAPS instrument and its data analysis. Furthermore, thank you to Nicole Spelten for the pleasant years in our shared office. In addition to the 'water vapour and clouds' group of Forschungszentrum Jülich, Dr. Anna Luebke, Prof. Dr. Martin W. Gallagher, Dr. Andre Ehrlich, Prof. Dr. Manfred Wendisch, Prof. Dr. Darrel Baumgardner, and Dr. Heike Wex provided very helpful comments for the preparation of the mixed-phase temperature regime study. Special thanks to Dr. Martin Schnaiter and Dr. Emma Järvinen, who enabled the AIDA cloud chamber campaign RICE03 during which the possibilities and limits of the NIXE-CAPS ashpericity detection could be explored.

I thank the HITEC graduate school for the research grant that enabled me to take up this position, and broad experiences I was able to make during their program. In its course, I was able to visit Prof. Dr. Heini Wernli and Dr. Maxi Boettcher at the ETH Zürich, whom I would like to thank for the insights into their research and their helpful comments on my project.

Band / Volume 384

IEK-3 Report 2017

Sektorkopplung –
Forschung für ein integriertes Energiesystem
(2017), 182 pp
ISBN: 978-3-95806-256-6

Band / Volume 385

Bestimmung der Wolframerosion mittels optischer Spektroskopie unter ITER-relevanten Plasmabedingungen

M. Laengner (2017), vi, 184, XI pp
ISBN: 978-3-95806-257-3

Band / Volume 386

IEK-3 Report 2017

Sector Coupling –
Research for an Integrated Energy System
(2017), 175 pp
ISBN: 978-3-95806-258-0

Band / Volume 387

Photochemistry of Highly Oxidized Multifunctional Organic Molecules: a Chamber Study

L. I. M. Pullinen (2017), II, 96, xviii pp
ISBN: 978-3-95806-260-3

Band / Volume 388

Poröse Transportschichten für die Polymerelektrolytmembran-Wasserelektrolyse

M. Höh (2017), VI, 186 pp
ISBN: 978-3-95806-262-7

Band / Volume 389

Modelling of High Temperature Polymer Electrolyte Fuel Cells

Q. Cao (2017), 173 pp
ISBN: 978-3-95806-263-4

Band / Volume 390

Potential use of nitrification inhibitors for mitigating N₂O emission from soils

D. Wu (2017), 206 pp
ISBN: 978-3-95806-264-1

Band / Volume 391

Mechanical Characterization of Solid Oxide Fuel Cells and Sealants

J. Wei (2017), II, 151 pp
ISBN: 978-3-95806-266-5

Band / Volume 392

Microcrystalline Silicon Carbide for Silicon Heterojunction Solar Cells

M. B. Pomaska (2017), 150 pp

ISBN: 978-3-95806-267-2

Band / Volume 393

Einfluss der Kristallisation auf das Fließverhalten oxidischer Schmelzen

S. Seebold (2017), 168 pp

ISBN: 978-3-95806-268-9

Band / Volume 394

Water vapour in the UTLS – Climatologies and Transport

P. R. Neis (2017), x, 124 pp

ISBN: 978-3-95806-269-6

Band / Volume 395

Neutronenaktivierungsanalyse mit gepulsten 14 MeV Neutronen zur Charakterisierung heterogener radioaktiver Abfälle

F. Mildenberger (2017), vi, 128 pp

ISBN: 978-3-95806-271-9

Band / Volume 396

Coupled biotic-abiotic mechanisms of nitrous oxide production in soils during nitrification involving the reactive intermediates hydroxylamine and nitrite

S. Liu (2017), xvii, 148 pp

ISBN: 978-3-95806-272-6

Band / Volume 397

Mixed-phase and ice cloud observations with NIXE-CAPS

A. Costa (2017), xviii, 117 pp

ISBN: 978-3-95806-273-3

Weitere **Schriften des Verlags im Forschungszentrum Jülich** unter

<http://www.zb1.fz-juelich.de/verlagextern1/index.asp>

**Energie & Umwelt /
Energy & Environment
Band / Volume 397
ISBN 978-3-95806-273-3**

